Underwater Acoustic Localization and Tracking of Pacific Walruses in the Northeastern Chukchi Sea

by

Brendan Pearce Rideout
BASc., University of Waterloo, 2008

A Thesis Submitted in Partial Fulfillment of the
Requirements for the Degree of

MASTER OF SCIENCE

in the School of Earth and Ocean Science

University of Victoria

Underwater Acoustic Localization and Tracking of Pacific Walruses in the Northeastern Chukchi Sea

by

Brendan Pearce Rideout
BASc., University of Waterloo, 2008

Supervisory Committee

Dr. Stan E. Dosso, Supervisor
(School of Earth and Ocean Sciences)

Dr. N. Ross Chapman, Departmental Member
(School of Earth and Ocean Science)

Dr. Michael Wilmut, Departmental Member
(School of Earth and Ocean Science)

Mr. David Hannay, Additional Member
(JASCO Research, Ltd.)

Supervisory Committee

Dr. Stan E. Dosso, Supervisor
(School of Earth and Ocean Sciences)

Dr. N. Ross Chapman, Departmental Member
(School of Earth and Ocean Science)

Dr. Michael Wilmut, Departmental Member
(School of Earth and Ocean Science)

Mr. David Hannay, Additional Member
(JASCO Research, Ltd.)

ABSTRACT

This thesis develops and demonstrates an approach for estimating the three-dimensional (3D) location of a vocalizing underwater marine mammal using acoustic arrival time measurements at three spatially separated receivers while providing rigorous location uncertainties. To properly account for uncertainty in the measurements of receiver parameters (e.g., 3D receiver locations and synchronization times) and environmental parameters (water depth and sound speed correction), these quantities are treated as unknowns constrained with prior estimates and prior uncertainties. While previous localization algorithms have solved for an unknown scaling factor on the prior uncertainties as part of the inversion, in this work unknown scaling factors on both the prior and arrival time uncertainties are estimated. Maximum *a posteriori* estimates for sound source locations and times, receiver parameters, and environmental parameters are calculated simultaneously. Posterior uncertainties for all unknowns are calculated and incorporate both arrival time and prior uncertainties. Simulation results demonstrated that, for the case considered here, linearization errors are generally small and that the lack of an accurate sound speed profile does not necessarily cause large uncertainties or biases in the estimated positions. The primary motivation for this work was to develop an algorithm for locating underwater Pacific walruses in the coastal waters around Alaska. In 2009, an array of approximately 40 underwater acoustic receivers was deployed in the northeastern Chukchi Sea (northwest of Alaska) from August to October to record the vocalizations of marine mammals including Pacific walruses and bowhead whales. Three of these receivers were placed in a triangular arrangement approximately 400 m apart near the Hanna Shoal (northwest of Wainwright, Alaska). A sequence of walrus knock vocalizations from this data set was processed using the localization algorithm developed in this thesis, yielding a track whose estimated swim speed is consistent with current knowledge of normal walrus swim speed. An examination of absolute and relative walrus location uncertainties demonstrated the usefulness of considering relative uncertainties for applications where the precise location of the mammal is not important (e.g., estimating swim speed).

Contents

List of Tables

List of Figures

ACKNOWLEDGEMENTS

I would like to thank:

my principal advisors, Dr. Stan Dosso and Dave Hannay; I lack the words to sufficiently express my gratitude to both of you for your eagerness and availability to help me at every stage of this work,

my family and friends, for the years of support and encouragement which helped me get to this point,

my colleagues at the School of Earth and Ocean Sciences and JASCO Research Ltd., for answering my frequent questions on walrus ecology and for many helpful suggestions,

ConocoPhillips Company, for allowing access to underwater acoustic data collected on their behalf during the summer of 2009, and

NSERC, Dr. Stan Dosso, the British Columbia Ministry for Advanced Education, JASCO Research Ltd., and the University of Victoria for providing the funding necessary to complete this work.

DEDICATION

This work is dedicated to the unknown walrus whose location I have been estimating for the last 3 years. Thank you for swimming through my small part of the ocean at just the right time, and for creating what may be the most highly scrutinized 7.2 seconds of Pacific walrus knock data in the history of marine science. You are a much more engaging walrus than either John or Paul; knock on!

Chapter 1

Introduction

Locating and tracking marine mammals underwater has been a topic of much interest in the scientific and marine industrial communities for at least the last 40 years. Marine mammal localization is a problem faced by scientists seeking to understand marine mammal behavior. For example, insight into prey selection, feeding depths and techniques, and swim speed are all enhanced through localizing and tracking marine mammals underwater. Additionally, the protection afforded marine mammals in the vicinity of underwater anthropogenic noise sources would be enhanced by knowing the underwater positions of nearby animals. Also, information on animal location relative to anthropogenic noise sources will allow a more accurate assessment of the effects of these noise sources on marine mammals. Due to the virtual impossibility of collecting underwater visual observations over large ranges, acoustic techniques are of great interest. Passive acoustic techniques, such as the one presented in this work, are of particular interest. While previous work has explored underwater acoustic marine mammal localization in a known environment, the incorporation of environmental and hydrophone location uncertainties to produce rigorous localization uncertainties has received comparatively little attention.

Marine mammal localization has been a topic of study since at least the mid-1970s. Watkins and Schevill [1972] presented a method for calculating the three-dimensional (3D) location of an underwater marine mammal using the relative arrival times of vocalizations at a four-hydrophone 3D array (three shallow receivers and one deeper) located near the surface. The hydrophones were deployed off a surface vessel, and were spaced approximately 30 m apart. A transducer deployed from the vessel produced sounds to locate the hydrophones and characterize the system response. Sounds from nearby ships and marine mammals were recorded by the array and localized. Errors in estimated relative arrival times were thought to more significantly affect estimated range than estimated direction. Good range estimates were found to be possible out to ranges 10 times the spacing between the hydrophones. For larger ranges, estimated ranges were often unreliable. In Watkins and Schevill [1977], this method was used to estimate the direction of vocalizing sperm whales relative to the array. Due to the expected long ranges of the whales from the array, range estimates were deemed unreliable.

Cummings and Holliday [1985] demonstrated that arrival time differences could be used for localization of bowhead whale vocalizations in the Arctic. Three hydrophones were deployed through a grounded ice ridge near Pt. Barrow, Alaska, forming an approximately linear 2.5 km horizontal array. Range and bearing estimates from the array to vocalizing bowhead whales were calculated, and estimates for the number of calling animals were made.

Spiesberger and Fristrup [1990] developed a method for estimating sound source locations (for either terrestrial or underwater sources) while also estimating the uncertainties in these positions. Relative arrival times for animal vocalizations at an array of receivers were measured. Uncertainties in arrival times, along with uncertainties in the sound speed, movement of the acoustic propagation medium (i.e., winds or currents), and receiver positions were used to estimate the uncertainty in the estimated source position. This approach used linear inverse theory to carry out localization. In a subsequent study, Spiesberger [1999] suggested that due to the non-linear nature of acoustic propagation, using a non-iterative linear approach to carry out localization gave sub-optimal results. Freitag and Tyack [1993] applied this method to 3D localization using vocalizations from captive Atlantic bottlenose dolphins recorded by an array of four to six hydrophones.

Stafford et al. [1998] located blue whales underwater using relative arrival times for vocalizations recorded by the U.S. Navy sound surveillance system (SOSUS) off the Pacific Northwest of the United States. Unlike previous localization approaches, which tended to use multiple hydrophones to perform localization, Aubauer et al. [2000] presented a method for estimating the range and depth of a marine mammal underwater using direct and interface-reflected acoustic arrival times at a single hydrophone in a range independent environment. Thode et al. [2000] presented a method for estimating the 3D position of a calling blue whale. First, selected calls were localized using a genetic algorithms localization scheme and a normal-mode propagation model. Estimates of the composition of the ocean bottom and the shape of the array were also made. Next, a matched-field processing approach was used to locate other calls in the track. Tiemann et al. [2006] developed an algorithm for estimating the 3D location of a marine mammal underwater using direct and interface-reflected acoustic arrivals at a single hydrophone. This method used known range-dependent bathymetry around the hydrophone to distinguish between sources at the same range but different azimuth angles. The method was demonstrated using sperm whale vocalizations recorded southeast of Alaska. Nosal and Frazer [2006] presented an approach for estimating 3D sperm whale position using the arrival time difference between direct and surface-reflected acoustic arrivals at an array of four receivers. For each receiver, the range and depth of the sperm whale was estimated by comparing the measured time difference to those at candidate ranges and depths about the receiver. The estimated ranges and depths from each receiver were combined to yield a single estimate of the estimated 3D whale position. Nosal and Frazer [2007] extended this method by incorporating arrival times for direct acoustic arrivals. Along with estimating the 3D position, the pitch and yaw of the vocalizing animal were estimated by measuring the swim direction of the animal and assuming the main axis of the whale is located along the swim direction. Roll was estimated using knowledge of the beam pattern of sperm whale clicks.

This thesis considers the problem of acoustic localization of submerged Pacific walruses (*Odobenus rosmarus divergens*) northwest of Alaska in the Chukchi Sea. Localization is a tool which can offer insights into walrus population trends and underwater behavior which would otherwise be difficult to observe. Studying the Pacific walrus is of particular importance at this time for several reasons. First, according to the IUCN Red List of Threatened Species, climate change is expected to have a particularly negative impact on the Pacific walrus population (Lowry et al. [2011]). Second, increased anthropogenic noise (from ongoing oil exploration in traditional walrus habitats) may cause changes in Pacific walrus habitat usage over time. Third, little work has been done in observing walrus behavior in the wild.

Pacific walruses winter in the Bering Sea. Their seasonal migration patterns closely follow seasonal variation in pack ice coverage in the Chukchi and Bering Seas (Fay [1982]). In mid-June to mid-July, females, juveniles, and pups migrate north to the Chukchi Sea where they haul out on ice floes. Many of these animals travel to the Hanna Shoal, north of Wainwright Alaska, where the water is shallow and ice tends to linger well into August. Walruses haul out on ice floes and dive to the bottom to feed on benthic organisms.

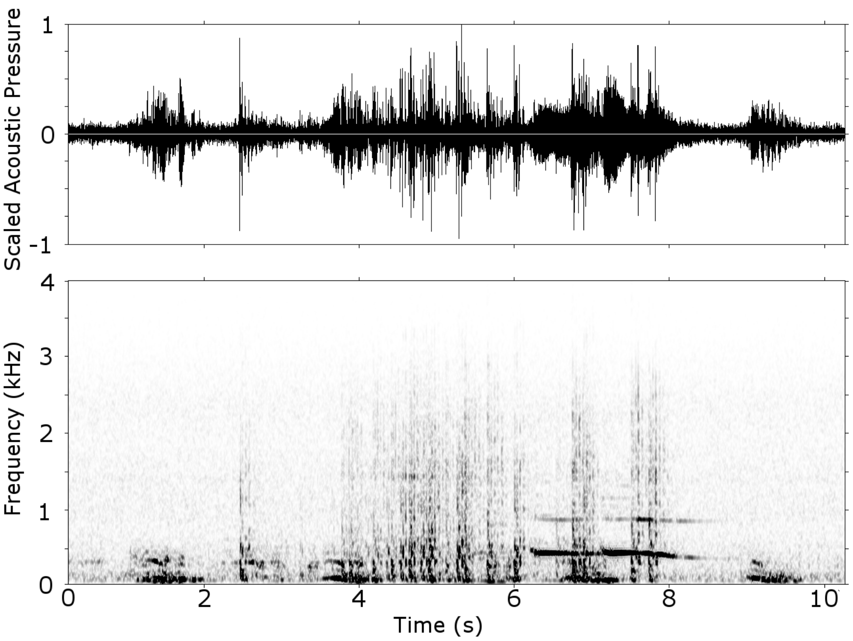

Figure 1.1: An acoustic time series and spectrogram containing walrus grunts, knocks, and bells. Data courtesy of JASCO Research, Ltd..

Walruses are considered highly gregarious animals (Miller [1985], Ray et al. [2006]), and make a variety of different types of vocalizations both in air (Miller [1985]) as well as underwater (Schevill et al. [1966], Stirling et al. [1987], Schusterman and Reichmuth [2008]). Three types of walrus vocalizations are bells, knocks, and grunts. Bells are tonal vocalizations which can be several seconds long. Knocks are short duration, wide bandwidth vocalizations. Grunts are low frequency vocalizations lasting one second or more. Figure 1.1 shows examples of bell, knock, and grunt-type vocalizations. Bells are seen from 6 s to 8 s. Knocks are observed between 2 s and 8 s with a particularly high concentration between 4 s and 6 s. Grunts are seen at 1 s, 3.5 s, 6.5 s, and 9 s.

To date, little work has been done in localizing walruses. Wiig et al. [1993] presented data collected over a two week period by a depth recorder attached to an Atlantic walrus near Svalbard in 1991. The animal was first sedated, after which the depth recorder was attached to one of its tusks and the animal revived. After two weeks, the walrus was again sedated, the recorder was removed, and the animal revived. While invasive, this study gave important insight into walrus swim speed, dive depth, and dive durations. In Jay et al. [2009], satellite tracking tags were attached to 34 Pacific walruses in the southern Chukchi Sea near the Alaskan coast.

Signals received from these tags were used to estimate the hourly position of the walrus. While some of the walruses from this tagging location moved to the Russian side of the Chukchi Sea during the recording period, the majority continued northward on the Alaskan side. Mouy et al. [2011] presented a method for estimating the two-dimensional location (range and depth) of a vocalizing underwater walrus using relative multipath arrival times at a single hydrophone assuming a range-independent environment. First, model-predicted arrival times were calculated over a set of candidate source positions using a ray-tracing propagation model (BELLHOP, Porter and Liu [1994]). Next, the portion of the waveform containing the arrivals for the vocalization is identified. The leading edge of this waveform portion is estimated using a combination of kurtosis and manual analysis. The trailing edge of the portion is calculated using a threshold on the normalized cumulative Teager-Kaiser energy. This waveform portion is then compared with the model-predicted arrival times for each candidate source position. To account for environmental uncertainty, each model-predicted arrival is represented by a box function, centred on the calculated arrival time, with a width of 2 ms. The match between measured and model-predicted data is taken to be integral of the Teager-Kaiser energy of the measured arrivals falling within those boxes. The source location which maximizes this match is taken to be the estimated walrus location.

This thesis presents a method for estimating the 3D location of an underwater sound source while also rigorously calculating the uncertainty in this location. Arrival times (and arrival time uncertainties) for direct and interface-reflected (i.e., sea surface and bottom) acoustic rays at an array of underwater receivers are processed using an iterated linearized Bayesian inversion algorithm. Receiver parameters (e.g., 3D receiver locations and synchronization times) and environmental parameters (water depth and sound speed correction) are treated as unknowns constrained with prior estimates and prior uncertainties. Maximum *a posteriori* (MAP) estimates for sound source locations and times, receiver locations, and environmental parameters are calculated simultaneously. Posterior uncertainties for all unknowns are calculated and incorporate both arrival time and prior uncertainties.

The work in this thesis builds upon a linearized inversion approach previously developed for array element localization (Dosso et al. [1998a], Dosso et al. [1998b], Dosso et al. [2004], Dosso and Ebbeson [2006]). In Dosso et al. [1998b], a method for locating the elements of an ocean-bottom horizontal array of hydrophones was presented. Data were collected on a 3D array of hydrophones (called the Spinnaker array) located north of Ellesmere Island, Canada, in April 1996. Data for this experiment consisted of relative travel times for underwater impulsive acoustic sources at the horizontal arrays. This approach used an iterative linearized inversion and *a priori* information on source locations, depths of the end points of each of the two horizontal line arrays, and the expected shape of each of the arrays to solve for array element and source locations. In addition to fitting the relative travel time data to a statistically appropriate level, source and hydrophone positions were selected which minimized the curvature of each array. An unknown scaling factor on the prior uncertainties was solved for during the inversion but data uncertainties were assumed to be known. A rigorous model parameter (posterior) uncertainty analysis was carried out by estimating prior and data uncertainties.

For the work presented in this thesis, the array element localization approach is extended using the Akaike Bayesian information criterion (ABIC), as developed in Akaike [1974]. In array element localization, as presented in Dosso and Ebbeson [2006], an unknown scaling factor on the prior uncertainties is estimated as part of the inversion. However, data uncertainties are assumed to be known. The ABIC can be used to estimate unknown scaling factors on both the data and prior uncertainties. Two recent implementations of the ABIC in geophysical inverse problems are found in Mitsuhata et al. [2001] and Guo et al. [2011]. In these two cases, the ABIC is used to calculate the trade-off between the fit to the measured data and a smoothness constraint on the estimated model.

The localization algorithm outlined above is applied in this thesis to localize Pacific walruses based on their vocalizations. From August - October 2009, approximately 40 underwater acoustic receivers were deployed throughout the northeastern Chukchi Sea (northwest of Alaska) in order to monitor the migration paths of marine mammals, including bowhead whales and Pacific walruses. Three of the 40 receivers were placed in a triangular arrangement approximately 400 m apart near the Hanna Shoal. The author of this thesis assisted in designing the layout of this three-element array, acquired the sound speed profile used in this thesis while on assignment in the Chukchi Sea in August 2009, and has spent over 3 months at sea on field work in the coastal waters around Alaska since 2008. Walrus knocks were recorded by these receivers throughout the deployment period. Until recently, only males were known to produce knocks. However, in Schusterman and Reichmuth [2008], both mature female and male walruses were observed to produce knocks. It is also possible that, along with mature animals, juvenile walruses could have produced the knocks recorded near the

Hanna Shoal.

Simulation results presented in this thesis demonstrate that this localization approach reliably locates submerged sound sources in an uncertain environment deemed representative of the conditions at the measured data collection site and time. Additionally, the calculated swim speed based on estimated locations for walrus vocalizations recorded in 2009 is consistent with current knowledge of normal walrus swim speed.

The following are descriptions of the remaining chapters in this thesis:

Chapter 2 develops the localization algorithm used for this work. Specifically, a derivation for the ABIC linearized inversion algorithm is presented. Both linear and linearized formulations for this algorithm are discussed. A description of the two propagation models (for curving-ray and straight-line acoustic propagation) used for this work is also included. Finally, a technique for calculating the relative uncertainty between estimated parameters based on the posterior model covariance matrix is derived.

Chapter 3 presents simulation results for the localization algorithm for a variety of scenarios. These scenarios employ a Monte Carlo approach to explore the differences in localization performance using either curving-ray or straight-line acoustic propagation, the significance of linearization error, how sensitive the inversion is to data set size, the effects of mislabeling arrival paths on localization, the precision and accuracy with which environmental and hydrophone parameters are estimated, and a comparison of relative and absolute localization uncertainties.

Chapter 4 describes the data collection portion of the project, including a description of the data recorders, justification for the selection of the data collection site, the importance of Pacific walruses as the study subject, and descriptions of the physical basis for the environmental and hydrophone parameter prior uncertainties.

Chapter 5 presents the techniques used to identify and label arrival paths of walrus vocalizations. The method for estimating arrival time uncertainties (i.e., data uncertainties) is also discussed.

Chapter 6 presents estimated locations and posterior uncertainties for a set of walrus vocalizations recorded in the Chukchi Sea in August, 2009. The estimated swim speed, and swim speed uncertainty, are computed for this track.

Chapter 7 summarizes the salient points of this thesis, along with several areas for further research.

Chapter 2

Localization Algorithm

The field of inverse theory is essential to localization as it is formulated in this work. Inverse theory can be defined as the estimation of the parameters of a postulated model for a physical system from observations (data) of some process which interacts with the system. In the context of underwater sound source localization, the "system" is the underwater environment. The "process" consists of underwater acoustic propagation. The "model" is an explanation of how the properties of the underwater environment determine underwater acoustic propagation. The "parameters" of this model, in general, include the sound source location and transmission time, the location and time synchronization factor of each of the receivers, water depth, and sound speed profile (SSP). Finally, the "observations" of interest for this work consist of the arrival times of direct and interface-reflected acoustic arrivals at the receivers.

The marine mammal tracking approach developed in this work is based on an array element localization algorithm presented in Dosso et al. [1998b] and Dosso and Ebbeson [2006]. Array element localization is the process of locating the hydrophones of an underwater array by producing sounds at measured locations (with estimated uncertainties). The arrival time of the direct and interface-reflected rays are recorded at each hydrophone. These arrival times are used to invert for hydrophone locations, source times and improved source locations, and environmental parameter values that produce model-predicted data which match the observed data to within the desired fit level.

Array element localization, as formulated in Dosso et al. [1998b] and Dosso and Ebbeson [2006], assumes that data uncertainties are known independently. To treat data uncertainties as unknowns to be estimated from the data, the array element localization inversion method is extended here using the Akaike Bayesian information criterion (Akaike [1974], Mitsuhata et al. [2001], Mitsuhata and Uchida [2002], Guo et al. [2011]).

2.1 Propagation Model

Inversion algorithms incorporating two different propagation models were implemented. For cases when a measured SSP is available, a propagation model incorporating vertical refraction is used, as presented in Dosso and Ebbeson [2006]. For the special case of constant sound speed with depth (typically assumed if a measured SSP is not available) a straight-line propagation model can be used. In both cases a uniform correction to the SSP can be included in the inversion; in the case of constant sound speed with depth this is equivalent to inverting for the SSP. This section briefly describes these two propagation models. A comparison of localization accuracy and uncertainties, using synthetic data, for these two models is presented in Section 3.2.

2.1.1 Ray Tracing

The derivation presented in this section is based on that presented in Dosso and Ebbeson [2006]. This propagation model is referred to as the curving-ray propagation model in subsequent sections of this thesis. The integrals in this section assume that the source is shallower than the receiver. For sources deeper than the receiver, the integrals below are multiplied by -1 except where noted. Consider the j^{th} receiver at location $\left(X_j, Y_j, Z_j\right)$ and i^{th} source at $\left(x_i, y_i, z_i\right)$ in water with SSP $c(z)$. Throughout this work, the z-coordinate is measured positive downward from the ocean surface. The horizontal range between the source and receiver is

$$r = [(x_i - X_j)^2 + (y_i - Y_j)^2]^{1/2}. \tag{2.1}$$

For non-turning rays (i.e., rays that do not reverse vertical direction), range and arrival time for a ray connecting source and receiver are calculated by applying Snell's law to an infinite stack of infinitesimal layers (Telford et al. [1976]):

$$r_{ij} = \int_{z_i}^{Z_j} \frac{pc(z)dz}{[1 - p^2c^2(z)]^{1/2}}, \tag{2.2}$$

$$t_{ij} = t_{0i} + \tau_j + \int_{z_i}^{Z_j} \frac{dz}{c(z)[1 - p^2c^2(z)]^{1/2}}, \tag{2.3}$$

where p is the ray parameter ($p = cos\theta(z)/c(z)$ where θ is the grazing angle) and t_{0i} is the source transmission time. In general, there will be a significant time difference in the recording start times between acoustic recorders. To accurately compare arrival times of a single source recorded on multiple recorders, a time correction factor (τ_j) must be applied to bring the j^{th} recorder in line with the experiment reference time. The parameter τ_j is unknown, and will be solved for as part of the inverse problem. For convenience, the start time of one of the recorders can be arbitrarily set as the experiment reference time.

In Eq. (2.2) and (2.3), the ray parameter is constant along a ray and defines the takeoff angle for that ray. A search over p is required to find the value which connects source and receiver to within a predefined range tolerance. For non-turning rays an efficient method for determining p uses Newton's method (Dosso et al. [1998b]). A starting estimate (p_0) is made by approximating the measured SSP with the harmonic mean (c_H) of the profile between the source and receiver depths where

$$c_H = \frac{Z_j - z_i}{\int_{z_i}^{Z_j} dz/c(z)}. \tag{2.4}$$

This equation is also valid for $Z_j \leq z_i$. Using the range between source and receiver (r_{ij}) and assuming straight-line propagation, p_0 is given by

$$p_0 = \frac{r_{ij}}{\left(r_{ij}^2 + (Z_j - z_i)^2\right)^{1/2} c_H}. \tag{2.5}$$

The ray parameter estimate p_0 can be improved by considering a Taylor expansion of $r(p)$ about p_0 (neglecting higher order terms) which yields an update

$$p_1 = p_0 + \left[\frac{\partial r(p_0)}{\partial p}\right]^{-1} \Big(r(p) - r(p_0)\Big). \tag{2.6}$$

In Eq. (2.6), $\partial r/\partial p$ is derived by differentiating Eq. (2.2) according to Leibnitz's rule, yielding

$$\frac{\partial r}{\partial p} = \int_{z_i}^{Z_j} \frac{c(z)dz}{[1 - p^2c^2(z)]^{3/2}}. \tag{2.7}$$

If $|r(p_1) - r_{ij}|$ is less than the range tolerance, p is deemed to have converged. Otherwise, $p_0 \leftarrow p_1$ and the process is repeated iteratively until convergence. Upon convergence, the arrival time of the ray is calculated using Eq. (2.3).

In addition to calculating ray travel times, the localization algorithm presented here requires partial derivatives of ray arrival time with respect to source and receiver positions, source times, synchronization times, water depth, and sound speed bias. Using the chain rule, $\partial t/\partial x_i$ is expressed as

$$\frac{\partial t}{\partial x_i} = \frac{\partial t}{\partial p}\frac{\partial p}{\partial r}\frac{\partial r}{\partial x_i} = \frac{\partial t}{\partial p}\left[\frac{\partial r}{\partial p}\right]^{-1}\frac{\partial r}{\partial x_i}. \tag{2.8}$$

The three partial derivatives on the right can be evaluated using Eq. (2.3), (2.2), and (2.1), yielding

$$\frac{\partial t}{\partial x_i} = p(x_i - X_j)/r. \tag{2.9}$$

Similarly, partial derivatives for the remaining horizontal coordinates are

$$\frac{\partial t}{\partial X_j} = p(X_j - x_i)/r, \tag{2.10}$$

$$\frac{\partial t}{\partial y_i} = p(y_i - Y_j)/r, \tag{2.11}$$

$$\frac{\partial t}{\partial Y_j} = p(Y_j - y_i)/r. \tag{2.12}$$

The partial derivative of arrival time with respect to Z_j can be derived from Eq. (2.3):

$$\frac{\partial t}{\partial Z_j} = \int_{z_i}^{Z_j} \frac{pc(z)dz}{[1-p^2c^2(z)]^{3/2}}\left(\frac{\partial p}{\partial Z_j}\right) - \frac{1}{c(Z_j)[1-p^2c(Z_j)^2]^{1/2}}. \tag{2.13}$$

To derive a formula for $\partial p/\partial Z_j$, it is noted that the horizontal range for rays traveling between source and receiver is independent of source or receiver depth (i.e., $\partial r/\partial Z_j = 0$). Therefore, an expression for $\partial p/\partial Z_j$ is found by calculating $\partial r/\partial Z_j$ from Eq. (2.2):

$$\frac{\partial r}{\partial Z_j} = 0 = \int_{z_i}^{Z_j} \frac{c(z)dz}{[1-p^2c^2(z)]^{3/2}}\left(\frac{\partial p}{\partial Z_j}\right) - \frac{pc(Z_j)}{[1-p^2c^2(Z_j)]^{1/2}}. \tag{2.14}$$

Solving Eq. (2.14) for $\partial p/\partial Z_j$ and substituting into Eq. (2.13) yields

$$\frac{\partial t}{\partial Z_j} = \frac{1}{c(Z_j)}[1-p^2c^2(Z_j)]^{1/2}. \tag{2.15}$$

Similarly,

$$\frac{\partial t}{\partial z_i} = -\frac{1}{c(z_i)}[1 - p^2 c^2(z_i)]^{1/2}. \tag{2.16}$$

The derivatives of arrival time, Eq. (2.3), with respect to source time (t_{0i}) and synchronization time (τ_j) are

$$\frac{\partial t}{\partial t_{0i}} = 1, \tag{2.17}$$

$$\frac{\partial t}{\partial \tau_j} = 1. \tag{2.18}$$

However, to improve the numerical stability of the inversion, t_{0i} and τ_j in Eq. (2.3) are replaced by $\big(\bar{c}t_{0i}\big)/\bar{c}$ and $\big(\bar{c}\tau_j\big)/\bar{c}$, where $\bar{c}$ is a representative sound speed (an arbitrary constant selected to provide appropriate scaling to t_0 and τ_j). This allows the unknowns to be represented as $\bar{c}t_{0i}$ and $\bar{c}\tau_j$, which have the same units and similar magnitudes and uncertainties as the positional parameters in the problem. This scaling results in the following partial derivatives for $\bar{c}t_{0i}$ and $\bar{c}\tau_j$:

$$\frac{\partial t}{\partial\big(\bar{c}t_{0i}\big)} = \frac{1}{\bar{c}}, \tag{2.19}$$

$$\frac{\partial t}{\partial\big(\bar{c}\tau_j\big)} = \frac{1}{\bar{c}}. \tag{2.20}$$

While measured SSPs are generally accurate in expressing relative sound speed, inaccurate calibration can result in a uniform bias of up to 2 m/s (Vincent and Hu [1997]). To account for this, the SSP is written $c(z) = c_t(z) + c_b$, where $c_t(z)$ is the true profile and c_b is the unknown bias. Calculating $\partial t/\partial c_b$ for Eq. (2.3) (where $\partial p/\partial c = -p/c$) yields

$$\frac{\partial t}{\partial c_b} = -\int_{z_i}^{Z_j} \frac{dz}{c^2(z)[1 - p^2 c^2(z)]^{1/2}}. \tag{2.21}$$

The development above applies to direct rays. For rays bouncing off the sea surface and/or bottom, the method of images can be used to represent higher order arrival paths as direct arrivals. Effectively, an interface-reflected ray from the true source location is represented as a direct ray from an image source located above the surface or below the bottom (Brekhovskikh and Lysanov [2003]). To accomplish this, the measured SSP is reflected about the boundary one or more times such that the direct ray from the image source experiences the same variation in sound speed along its

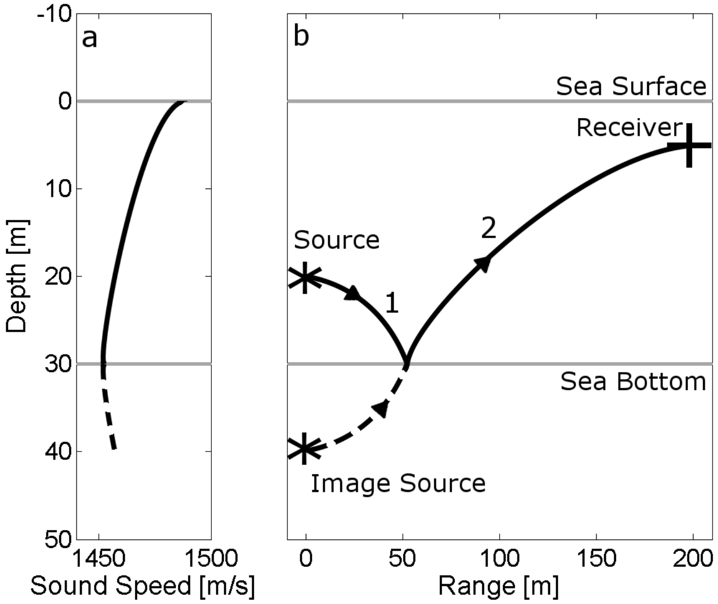

Figure 2.1: An illustration of the method of images approach to expressing a bottom bounce ray as a direct ray. In (a), the SSP is reflected about the bottom to accomodate the image source. In (b), the source location is reflected about the bottom as an image source.

path as the physical ray. This process is illustrated in Fig. 2.1 for a bottom-reflected ray. The method of images can be applied recursively for cases involving multiple reflections.

The inversion algorithm presented in Dosso and Ebbeson [2006] assumes that water depth, W, is known and constant. To allow water depth to be unknown in the inversion, $\partial t/\partial W$ is required. For example, the travel time along the ray in Fig. 2.1 can be expressed as the sum of the travel times along ray segments 1 and 2:

$$t = \int_{z_i}^{W} \frac{dz}{c(z)[1 - p^2c^2(z)]^{1/2}} + \int_{Z_j}^{W} \frac{dz}{c(z)[1 - p^2c^2(z)]^{1/2}}. \tag{2.22}$$

The partial derivative of arrival time with respect to water depth, $\partial t/\partial W$, is evaluated from Eq. (2.22) using Eq. (2.15):

$$\frac{\partial t}{\partial W} = \frac{2}{c(W)}[1 - p^2c^2(W)]^{1/2}. \tag{2.23}$$

This equation applies for arrival paths with a single bottom bounce. The general result is

$$\frac{\partial t}{\partial W} = \frac{2n_B}{c(W)}[1 - p^2c^2(W)]^{1/2}, \tag{2.24}$$

where n_B is the number of bottom bounces for a given ray path.

To implement the equations presented so far in this section it is assumed that the SSP can be represented as a series of discrete layers with a non-zero linear gradient in each layer. In the following equations, $\{(z_k,c_k),\ k{=}1,N_z\}$ represents a piecewise linear SSP of N_z layers and $\{g_k\}$ is the corresponding set of linear sound speed gradients. In this case, Eq. (2.2), (2.3), (2.4), (2.7), and (2.21) have the following analytic solutions (Dosso and Ebbeson [2006]), where $w_k \equiv (1 - p^2c_k^2)^{1/2}$:

$$r_{ij} = \sum_{k=i}^{j-1} \frac{w_k - w_{k+1}}{pg_k}, \tag{2.25}$$

$$t_{ij} = t_{0i} + \tau_j + \sum_{k=i}^{j-1} \frac{1}{g_k} \log_e \frac{c_{k+1}(1 + w_k)}{c_k(1 + w_{k+1})}, \tag{2.26}$$

$$c_H = (Z_j - z_i) / \sum_{k=i}^{j-1} \frac{1}{g_k} \log_e \frac{g_k(z_{k+1} - z_k) + c_k}{c_k}, \tag{2.27}$$

$$\frac{\partial r_{ij}}{\partial p} = \sum_{k=i}^{j-1} \frac{w_k - w_{k+1}}{p^2 g_k w_k w_{k+1}}, \tag{2.28}$$

$$\frac{\partial t}{\partial c_b} = \sum_{k=i}^{j-1} \frac{1}{g_k} \left[\frac{w_{k+1}}{c_{k+1}} - \frac{w_k}{c_k} \right]. \tag{2.29}$$

If a non-turning ray cannot be found which connects source and receiver, a search for a turning ray must be performed. An efficient method for performing this search uses the average sound speed gradient (g_{ave}) between source and receiver to indicate the most likely take-off direction from the source for a turning ray. For the case of $z_i < Z_j$ (source shallower than receiver) there are two situations to consider: $g_{\text{ave}} < 0$ and $g_{\text{ave}} > 0$. For $g_{\text{ave}} < 0$ (downward refracting), a connecting ray is first sought which heads upward from the source and turns downward. This search is performed by considering rays which turn at the top of each layer in the SSP above the source. If $g_k < 0$ for a given layer, the p value for the ray turning at the top of this layer is

$$p = 1/c_k. \tag{2.30}$$

If rays which turn at successive layer boundaries bracket the receiver, the bisection method is used to refine the estimate of p to within the prescribed range tolerance. If no bracketing rays are found, another search is performed seeking bracketing rays which head downward from the source and turn upward below the receiver (if they exist). Alternatively for $g_{\text{ave}} > 0$, the first search is performed for bracketing rays which turn upward below the receiver, followed by a search for bracketing rays which turn downward above the source (which may not exist). For $z_i > Z_j$, the same strategies as presented above are applied using reciprocity.

If the ray parameter for a turning ray is found to connect source and receiver, integrals along this ray are calculated. These calculations involve dividing the ray into a number of discrete sections. For example, consider the case of a downward traveling ray entering the l^{th} layer with $g_{\text{ave}} > 0$ (upward refracting). The turning depth for this ray is

$$z_T = z_l + (1/p - c_l)/g_l. \tag{2.31}$$

If $z_T < z_{l+1}$ the ray turns in the l^{th} layer. Otherwise, it continues downward into layer $l + 1$. If the ray turns in the l^{th} layer, and only turns once over its path length, the ray is divided into four sections for the purpose of evaluating integrals along the ray:

1. Source depth (z_i) down to the top of the turning layer (z_l)
2. z_l down to the turning depth (z_T)
3. z_T up to z_l
4. z_l up to the receiver depth (Z_j)

This segmentation leads to the following analytic forms of Eq. (2.2), (2.3), (2.7), and (2.21) for turning rays which initially travel downward:

$$r_{ij} = \sum_{k=i}^{l-1} \frac{w_k - w_{k+1}}{pg_k} + \frac{2w_l}{pg_l} + \sum_{k=l}^{j} \frac{w_k - w_{k-1}}{pg_{k-1}}, \tag{2.32}$$

$$t_{ij} = t_{0i} + \tau_j + \sum_{k=i}^{l-1} \frac{1}{g_k} \log_e \frac{c_{k+1}(1+w_k)}{c_k(1+w_{k+1})} + \frac{2}{g_l} \log_e \frac{1+w_l}{pc_l} + \sum_{k=l}^{j} \frac{1}{g_{k-1}} \log_e \frac{c_{k-1}(1+w_k)}{c_k(1+w_{k-1})}, \quad (2.33)$$

$$\frac{\partial r}{\partial p} = \sum_{k=i}^{l-1} \frac{w_k - w_{k+1}}{p^2 g_k w_k w_{k+1}} - \frac{2}{g_l p^2 w_l} + \sum_{k=l}^{j} \frac{w_k - w_{k-1}}{p^2 g_{k-1} w_k w_{k-1}}, \quad (2.34)$$

$$\frac{\partial t}{\partial c_b} = \sum_{k=i}^{l-1} \frac{1}{g_k} \left[\frac{w_{k+1}}{c_{k+1}} - \frac{w_k}{c_k} \right] + \frac{2w_l}{c_l g_l} + \sum_{k=l}^{j} \frac{1}{g_{k-1}} \left[\frac{w_{k-1}}{c_{k-1}} - \frac{w_k}{c_k} \right]. \quad (2.35)$$

Similar equations can be derived for the case of initially upward traveling rays and rays which turn multiple times.

2.1.2 Straight-Line Ray Tracing

For cases where a measured SSP is unavailable the sound speed is assumed to be an unknown constant and a straight-line ray tracing model is used. As in the ray tracing algorithm presented in Section 2.1.1, the method of images is applied. This propagation model is referred to as the straight-line propagation model in subsequent sections of this thesis.

For straight-line ray tracing, the travel time for any arrival path can be calculated using one of Eq. (2.36), (2.37), (2.38), and (2.39) which follow directly from the Pythagorean theorem:

$$t_1 = t_{0i} + \tau_j + \left[(x_i - X_j)^2 + (y_i - Y_j)^2 + (2n_B W + Z_j - z_i)^2\right]^{1/2} / c_w, \quad (2.36)$$

$$t_2 = t_{0i} + \tau_j + \left[(x_i - X_j)^2 + (y_i - Y_j)^2 + (2n_B W - Z_j - z_i)^2\right]^{1/2} / c_w, \quad (2.37)$$

$$t_3 = t_{0i} + \tau_j + \left[(x_i - X_j)^2 + (y_i - Y_j)^2 + (2n_B W + Z_j + z_i)^2\right]^{1/2} / c_w, \quad (2.38)$$

$$t_4 = t_{0i} + \tau_j + \left[(x_i - X_j)^2 + (y_i - Y_j)^2 + (2n_B W - Z_j + z_i)^2\right]^{1/2} / c_w. \quad (2.39)$$

Table 2.1 illustrates which equation is used depending on the number of surface and bottom bounces. In this table D indicates the direct path from source to receiver, B indicates a bottom reflection, S indicates a surface reflection, SB indicates a surface reflection followed by a bottom reflection, and so on.

The simple nature of this acoustic propagation model, as it is implemented for

Equation	1^{st} **Order Bounce Paths**	2^{nd}	3^{rd}	4^{th}
t_1	D	BS	BSBS	BSBSBS
t_2	B	BSB	BSBSB	BSBSBSB
t_3	S	SBS	SBSBS	SBSBSBS
t_4	SB	SBSB	SBSBSB	SBSBSBSB

Table 2.1: Direct and interface-reflected path arrivals classified according to the modelling equation and the arrival order.

this work, assumes uniform water depth (W) and sound speed (c_W). Optimal values for these parameters are estimated as part of the inversion. Partial derivatives for these equations are simple to derive and are not given explicitly here.

2.2 Linear Bayesian Inversion

This section provides an overview of linear Bayesian inversion, for which the relationship between data and model is expressed as $\mathbf{d}(\mathbf{m}) = \mathbf{A}\mathbf{m}$. In this work, $\mathbf{m}$ is the set of M model parameters, $\mathbf{d}(\mathbf{m})$ is the set of N model-predicted data, and $\mathbf{A}$ is the $N \times M$ sensitivity matrix. The non-linear localization problem will be solved by linearization and iteration as described in Section 2.4. Matrices (e.g., $\mathbf{A}$) and vectors (e.g., $\mathbf{m}$) are denoted by upper case and lower case bold characters respectively.

Bayesian inversion is based on Bayes' theorem,

$$P(\mathbf{m}|\mathbf{d})P(\mathbf{d}) = P(\mathbf{d}|\mathbf{m})P(\mathbf{m}), \tag{2.40}$$

where $P(\mathbf{m}|\mathbf{d})$ is the posterior probability density (PPD), $P(\mathbf{d})$ is the data prior distribution, $P(\mathbf{d}|\mathbf{m})$ is the conditional probability of observing the data given model $\mathbf{m}$, and $P(\mathbf{m})$ is the model prior distribution. Once the data are observed they are fixed such that $P(\mathbf{d})$ is considered constant and $P(\mathbf{d}|\mathbf{m})$ is taken to be a function of $\mathbf{m}$, known as the likelihood function $\mathrm{L}(\mathbf{m})$. Therefore, rearranging Eq. (2.40) leads to

$$P(\mathbf{m}|\mathbf{d}) \propto L(\mathbf{m})P(\mathbf{m}). \tag{2.41}$$

If the data errors are assumed to be Gaussian-distributed random variables with covariance matrix $\mathbf{C_d}$ and the prior distribution is assumed Gaussian-distributed with covariance matrix $\mathbf{C}_{\hat{\mathbf{m}}}$ about a prior estimate $\hat{\mathbf{m}}$

$$L(\mathbf{m}) = \frac{1}{(2\pi)^{N/2}|\mathbf{C_d}|^{1/2}} \exp\Big(- (\mathbf{d} - \mathbf{Am})^T {\mathbf{C_d}}^{-1} (\mathbf{d} - \mathbf{Am})/2 \Big), \tag{2.42}$$

$$P(\mathbf{m}) = \frac{1}{(2\pi)^{M/2}|\mathbf{C}_{\hat{\mathbf{m}}}|^{1/2}} \exp\Big(- (\mathbf{m} - \hat{\mathbf{m}})^T {\mathbf{C}_{\hat{\mathbf{m}}}}^{-1} (\mathbf{m} - \hat{\mathbf{m}})/2 \Big). \tag{2.43}$$

Substituting Eq. (2.42) and (2.43) into Eq. (2.41) yields

$$P(\mathbf{m}|\mathbf{d}) \propto \frac{1}{|\mathbf{C_d}|^{1/2}|\mathbf{C}_{\hat{\mathbf{m}}}|^{1/2}} \exp\Big(- \big((\mathbf{d} - \mathbf{Am})^T {\mathbf{C_d}}^{-1} (\mathbf{d} - \mathbf{Am}) + (\mathbf{m} - \hat{\mathbf{m}})^T {\mathbf{C}_{\hat{\mathbf{m}}}}^{-1} (\mathbf{m} - \hat{\mathbf{m}}) \big)/2 \Big). \tag{2.44}$$

To allow for uncertainty in the scaling of the data and prior model covariance matrices, these quantities are written

$$\mathbf{C_d} = \sigma_0^2 {\mathbf{C_d}}', \tag{2.45}$$

$$\mathbf{C}_{\hat{\mathbf{m}}} = \frac{\sigma_0^2}{\mu} {\mathbf{C}_{\hat{\mathbf{m}}}}', \tag{2.46}$$

where ${\mathbf{C_d}}'$ and ${\mathbf{C}_{\hat{\mathbf{m}}}}'$ are the relative error and prior covariance weighting matrices, respectively, and σ_0^2 and σ_0^2/μ are the corresponding scale factors (Mitsuhata & Uchida 2001).

Applying Eq. (2.45) and (2.46) to Eq. (2.44) leads to

$$P(\mathbf{m}|\mathbf{d}) \propto \Big(\frac{1}{(\sigma_0^2)^{(N+M)}(\mu^{-M})|{\mathbf{C_d}}'||{\mathbf{C}_{\hat{\mathbf{m}}}}'|} \Big)^{1/2} \exp \frac{-\Theta_L(\mathbf{m})}{2\sigma_0^2}, \tag{2.47}$$

where

$$\Theta_L(\mathbf{m}) = (\mathbf{d} - \mathbf{Am})^T {\mathbf{C_d}}'^{-1} (\mathbf{d} - \mathbf{Am}) + \mu (\mathbf{m} - \hat{\mathbf{m}})^T {\mathbf{C}_{\hat{\mathbf{m}}}}'^{-1} (\mathbf{m} - \hat{\mathbf{m}}). \tag{2.48}$$

In the special case where the error and prior covariance matrices are known absolutely (i.e., $\sigma_0^2 = \mu = 1$) the most probable or maximum *a posteriori* (MAP) model may be calculated by maximizing $P(\mathbf{m}|\mathbf{d})$ or equivalently minimizing $\Theta_L(\mathbf{m})$. Setting

$$\frac{\partial \Theta_L(\mathbf{m})}{\partial \mathbf{m}} = 0 \tag{2.49}$$

leads to

$$\mathbf{m}_{MAP} = \hat{\mathbf{m}} + \left(\mathbf{A}^T\mathbf{C_d}^{-1}\mathbf{A} + \mathbf{C_{\hat{m}}}^{-1}\right)^{-1}\mathbf{A}^T\mathbf{C_d}^{-1}\left(\mathbf{d} - \mathbf{A}\hat{\mathbf{m}}\right). \tag{2.50}$$

The PPD is a Gaussian distribution about this MAP model with posterior model covariance matrix

$$\mathbf{C_m} = (\mathbf{A}^T\mathbf{C_d}^{-1}\mathbf{A} + \mathbf{C_{\hat{m}}}^{-1})^{-1}. \tag{2.51}$$

In common applications, σ_0^2 is treated as known but μ as uncertain. In this case, a regularized inversion approach (e.g., Dosso et al. [1998b]) can be applied in which the MAP model and posterior model covariance matrix are given by

$$\mathbf{m}_{MAP} = \hat{\mathbf{m}} + \left(\mathbf{A}^T\mathbf{C_d}^{-1}\mathbf{A} + \mu\mathbf{C_{\hat{m}}}'^{-1}\right)^{-1}\mathbf{A}^T\mathbf{C_d}^{-1}\left(\mathbf{d} - \mathbf{A}\hat{\mathbf{m}}\right), \tag{2.52}$$

$$\mathbf{C_m} = (\mathbf{A}^T\mathbf{C_d}^{-1}\mathbf{A} + \mu\mathbf{C_{\hat{m}}}'^{-1})^{-1}, \tag{2.53}$$

where μ is selected so that the χ^2 misfit

$$\chi^2 = (\mathbf{d} - \mathbf{Am})^T\mathbf{C_d}^{-1}(\mathbf{d} - \mathbf{Am}) \tag{2.54}$$

achieves its expected value $<\chi^2>= N$. Since χ^2 increases monotonically with μ, this μ value can be determined with line search methods. The main-diagonal elements of $\mathbf{C_m}$ are the variances for the Gaussian marginal distributions which express the uncertainty of the parameters in $\mathbf{m}_{MAP}$. Off-diagonal elements are covariances between model parameters.

2.3 ABIC Linear Bayesian Inversion

In the previous section, the linear inverse problem was solved given that σ_0^2 was known and for the cases where μ was either known or unknown. For the case where both σ_0^2 and μ are unknown, the goal remains the maximization of the PPD. As in Section 2.2, this is analogous to minimizing $\Theta_L(\mathbf{m})$ (Eq. (2.48)) for given values of σ_0^2 and μ (the selection of these values is covered later in this section).

As developed in Mitsuhata and Uchida [2002], Eq. (2.48) can be expressed in the form

$$\Theta_L(\mathbf{m}) = |\tilde{\mathbf{d}} - \mathbf{Gm}|^2 = \left(\tilde{\mathbf{d}} - \mathbf{Gm}\right)^T\left(\tilde{\mathbf{d}} - \mathbf{Gm}\right) \tag{2.55}$$

where

$$\tilde{\mathbf{d}} = \begin{bmatrix} \mathbf{C_d}'^{-1/2}\mathbf{d} \\ \sqrt{\mu}\mathbf{C_{\hat{m}}}'^{-1/2}\hat{\mathbf{m}} \end{bmatrix}, \tag{2.56}$$

$$\mathbf{G} = \begin{bmatrix} \mathbf{C_d}'^{-1/2}\mathbf{A} \\ \sqrt{\mu}\mathbf{C_{\hat{m}}}'^{-1/2} \end{bmatrix}. \tag{2.57}$$

Once μ is determined (as discussed below), solving $\partial\Theta_L(\mathbf{m})/\partial\mathbf{m} = 0$ leads to

$$\mathbf{G}^T\mathbf{G}\mathbf{m}_{MAP} = \mathbf{G}^T\tilde{\mathbf{d}} \tag{2.58}$$

such that

$$\mathbf{m}_{MAP} = (\mathbf{G}^T\mathbf{G})^{-1}\mathbf{G}^T\tilde{\mathbf{d}}. \tag{2.59}$$

Solving Eq. (2.59) for $\mathbf{m}_{MAP}$ in such a way that data and prior information are properly balanced requires selecting appropriate values of μ and σ_0^2. To accomplish this, the Akaike Bayesian information criterion (ABIC, Akaike [1974]) is used. Essentially, the ABIC aims to optimize the marginal probability distribution $P(\mathbf{d}|\sigma_0^2, \mu)$ over the hyperparameters σ_0^2 and μ (i.e., maximize the likelihood over σ_0^2 and μ). The ABIC is based on the principle of entropy maximization and is defined as

$$\text{ABIC} = -2\log_e P(\mathbf{d}|\sigma_0^2, \mu) + 2N_H, \tag{2.60}$$

where N_H is the number of unknown hyper-parameters. Similar to developments in Mitsuhata et al. [2001], Mitsuhata and Uchida [2002], and Guo et al. [2011], an expression for $P(\mathbf{d}|\sigma_0^2, \mu)$ in terms of $P(\mathbf{d}|\mathbf{m}, \sigma_0^2, \mu)$ and $P(\mathbf{m}|\sigma_0^2, \mu)$ is derived starting with Bayes' theorem generalized to include the hyperparameters:

$$P(\mathbf{m}|\mathbf{d}, \sigma_0^2, \mu)P(\mathbf{d}|\sigma_0^2, \mu) = P(\mathbf{d}|\mathbf{m}, \sigma_0^2, \mu)P(\mathbf{m}|\sigma_0^2, \mu). \tag{2.61}$$

Integrating this equation over the model space and noting that

$$\int P(\mathbf{m}|\mathbf{d}, \sigma_0^2, \mu)\,d\mathbf{m} = 1 \tag{2.62}$$

leads to

$$P(\mathbf{d}|\sigma_0^2,\mu) = \int P(\mathbf{d}|\mathbf{m},\sigma_0^2,\mu)P(\mathbf{m}|\sigma_0^2,\mu)\,d\mathbf{m}. \tag{2.63}$$

$$\tag{2.64}$$

Therefore, the ABIC can be expressed as

$$\text{ABIC} = -2\log_e \int P(\mathbf{d}|\mathbf{m},\sigma_0^2,\mu)P(\mathbf{m}|\sigma_0^2,\mu)\,d\mathbf{m} + 2N_H. \tag{2.65}$$

Using the assumptions upon which Eq. (2.44) is based, the ABIC is written in terms of $L(\mathbf{m}|\sigma_0^2,\mu)$ and $P(\mathbf{m}|\sigma_0^2,\mu)$ as

$$\text{ABIC} = -2\log_e \int L(\mathbf{m}|\sigma_0^2,\mu)P(\mathbf{m}|\sigma_0^2,\mu)\,d\mathbf{m} + 2N_H. \tag{2.66}$$

Expanding Eq. (2.66) using Eq. (2.47) yields

$$\begin{aligned}\text{ABIC} = -2\log_e \frac{1}{(2\pi\sigma_0^2)^{N/2}|\mathbf{C_d}'|^{1/2}} - 2\log_e \frac{\mu^{M/2}}{(2\pi\sigma_0^2)^{M/2}|\mathbf{C_{\hat{m}}}'|^{1/2}} \\ - 2\log_e \int \exp\big(\frac{-\Theta_L(\mathbf{m})}{2\sigma_0^2}\big)\,d\mathbf{m} + 2N_H.\end{aligned} \tag{2.67}$$

Using Eq. (2.55), the integral in Eq. (2.67) becomes

$$\int \exp\big(\frac{-\Theta_L(\mathbf{m})}{2\sigma_0^2}\big)\,d\mathbf{m} = \int \exp\left(\frac{-1}{2\sigma_0^2}(\tilde{\mathbf{d}} - \mathbf{Gm})^T(\tilde{\mathbf{d}} - \mathbf{Gm})\right)\,d\mathbf{m}. \tag{2.68}$$

By multiplying out the integrand and multiplying by one in the form of

$$1 = \exp\left[\frac{-1}{2\sigma_0^2}\big(2\mathbf{m}_{MAP}(\mathbf{G}^T\mathbf{G}\mathbf{m}_{MAP} - \mathbf{G}^T\tilde{\mathbf{d}}) - 2\mathbf{m}^T(\mathbf{G}^T\mathbf{G}\mathbf{m}_{MAP} - \mathbf{G}^T\tilde{\mathbf{d}})\big)\right], \tag{2.69}$$

Eq. (2.68) can be rearranged to the form

$$\begin{aligned}\int \exp\big(\frac{-\Theta_L(\mathbf{m})}{2\sigma_0^2}\big)\,d\mathbf{m} = \int \exp\Big[\frac{-1}{2\sigma_0^2}\big((\mathbf{m} - \mathbf{m}_{MAP})^T\mathbf{G}^T\mathbf{G}(\mathbf{m} - \mathbf{m}_{MAP}) + \\ (\tilde{\mathbf{d}} - \mathbf{G}\mathbf{m}_{MAP})^T(\tilde{\mathbf{d}} - \mathbf{G}\mathbf{m}_{MAP})\big)\Big]\,d\mathbf{m}.\end{aligned} \tag{2.70}$$

By applying the transformation used in Appendix C of Mitsuhata et al. [2001] Eq.

(2.70) becomes

$$\int \exp\big(\frac{-\Theta_L(\mathbf{m})}{2\sigma_0^2}\big)\,d\mathbf{m} = \exp\Big(\frac{-1}{2\sigma_0^2}\Theta_L(\mathbf{m}_{MAP})\Big)(2\pi\sigma_0^2)^{M/2}|\mathbf{G}^T\mathbf{G}|^{-1/2}, \tag{2.71}$$

where $\Theta_L(\mathbf{m}_{MAP})$ is the result of evaluating Eq. (2.55) at $\mathbf{m}_{MAP}$, which itself is calculated using Eq. (2.59). Incorporating Eq. (2.71) into Eq. (2.67) and simplifying gives

$$\begin{aligned}\text{ABIC} = N\log_e\big(2\pi\sigma_0^2\big) - 2\log_e|\mathbf{C_d}'^{-1/2}| - M\log_e\big(\mu\big) - 2\log_e|\mathbf{C_{\hat{m}}}'^{-1/2}| \\ + \frac{\Theta_L(\mathbf{m}_{MAP})}{\sigma_0^2} + \log_e|\mathbf{G}^T\mathbf{G}| + 2N_H.\end{aligned} \tag{2.72}$$

The values of σ_0^2 and μ which minimize the ABIC are those which best represent the trade-off between data and prior information. Rather than performing a grid search over σ_0^2 and μ to minimize the ABIC, $\partial(ABIC)/\partial(\sigma_0^2) = 0$ is calculated for Eq. (2.72) and solved for σ_0^2 (Guo et al. [2011]). This provides an expression for the maximum likelihood estimate of σ_0^2:

$$\frac{\partial(\text{ABIC})}{\partial(\sigma_0^2)} = N\frac{1}{2\pi\sigma_0^2}2\pi - \frac{\Theta_L(\mathbf{m}_{MAP})}{(\sigma_0^2)^2} = 0 \tag{2.73}$$

implies

$$\sigma_0^2 = \frac{\Theta_L(\mathbf{m}_{MAP})}{N}. \tag{2.74}$$

Substituting Eq. (2.74) into Eq. (2.72) gives

$$\begin{aligned}\text{ABIC} = N\log_e\big(\frac{2\pi\Theta_L(\mathbf{m}_{MAP})}{N}\big) - 2\log_e|\mathbf{C_d}'^{-1/2}| - M\log_e\big(\mu\big) - 2 \\ \log_e|\mathbf{C_{\hat{m}}}'^{-1/2}| + N + \log_e|\mathbf{G}^T\mathbf{G}| + 2N_H.\end{aligned} \tag{2.75}$$

This equation only depends on μ. For each value of μ there is a different $\mathbf{m}_{MAP}$ according to Eq. (2.59), and therefore a different value of $\Theta_L(\mathbf{m}_{MAP})$ and the ABIC. To solve for the optimum model, a line search over μ is performed to minimize the ABIC. Once μ is selected, σ_0^2 is calculated using (2.74) and used to calculate the posterior model covariance matrix

$$\mathbf{C_m} = \sigma_0^2(\mathbf{A}^T\mathbf{C_d}'^{-1}\mathbf{A} + \mu\mathbf{C_{\hat{m}}}'^{-1})^{-1}. \tag{2.76}$$

In summary, the steps for carrying out ABIC linear Bayesian inversion are:

1. Define $\hat{\mathbf{m}}$, $\mathbf{C_d}'$, $\mathbf{C_{\hat{m}}}'$, and $\mathbf{A}$
2. Perform a line search over μ which minimizes the ABIC (Eq. (2.75))
3. Calculate σ_0^2 (Eq. (2.74)) using $\mathbf{m}_{MAP}$ from Eq. (2.59)
4. Calculate $\mathbf{C_m}$ (Eq. (2.76))

2.4 ABIC Linearized Bayesian Inversion

In the previous section, the method of minimizing the ABIC for a linear inverse problem was presented. However, there are many cases where the forward model for a given system is non-linear (e.g., the underwater acoustic propagation model used for this work). To address these non-linearities, iterative linearized ABIC Bayesian inversion can be applied as described in this section.

Whereas the linear problem is based on a linear system of equations, $\mathbf{d}(\mathbf{m}) = \mathbf{A}\mathbf{m}$, for non-linear inversion the data $\mathbf{d}(\mathbf{m})$ are calculated by evaluating a set of non-linear equations. Linearized inversion of a non-linear problem is based on a Taylor series expansion about an arbitrary starting model $\mathbf{m}_0$:

$$\mathbf{d}(\mathbf{m}) = \mathbf{d}(\mathbf{m}_0) + \sum_{j=1}^{M} \frac{\partial \mathbf{d}(\mathbf{m}_0)}{\partial m_j}(m_j - m_{0,j}) + \frac{1}{2!}\sum_{j=1}^{M}\sum_{k=1}^{M} \frac{\partial^2 \mathbf{d}(\mathbf{m}_0)}{\partial m_j \partial m_k}(m_j - m_{0,j})(m_k - m_{0,k}) + \cdots . \quad (2.77)$$

Ignoring second and higher order terms gives

$$\mathbf{d} \approx \mathbf{d}(\mathbf{m}_0) + \mathbf{J}(\mathbf{m} - \mathbf{m}_0) \quad (2.78)$$

where $\mathbf{J}$ is the $N \times M$ Jacobian matrix with elements

$$J_{ij} = \frac{\partial d_i(\mathbf{m}_0)}{\partial m_j}. \quad (2.79)$$

To use the linear inversion techniques described in the previous section, Eq. (2.78) is expressed as

$$\mathbf{d}' = \mathbf{d} - \mathbf{d}(\mathbf{m}_0) + \mathbf{J}\mathbf{m}_0 = \mathbf{J}\mathbf{m} \tag{2.80}$$

where $\mathbf{d}'$ represents the modified data vector for linearized inversion. Due to linearization error, multiple iterations of the inversion process are generally required to converge to a solution.

In Section 2.3 the ABIC is expressed in terms of $\mathbf{G}$ and $\tilde{\mathbf{d}}$. For linearized inversion, these quantities are modified to incorporate $\mathbf{J}$ and $\mathbf{d}'$:

$$\tilde{\mathbf{d}}_J = \begin{bmatrix} \mathbf{C_d}'^{-1/2}\mathbf{d}' \\ \sqrt{\mu}\mathbf{C_{\hat{m}}}'^{-1/2}\hat{\mathbf{m}} \end{bmatrix}, \tag{2.81}$$

$$\mathbf{G}_J = \begin{bmatrix} \mathbf{C_d}'^{-1/2}\mathbf{J} \\ \sqrt{\mu}\mathbf{C_{\hat{m}}}'^{-1/2} \end{bmatrix}. \tag{2.82}$$

Similar to the linear case in Eq. (2.59), once μ and σ_0^2 are determined $\mathbf{m}_{MAP}$ is calculated by solving

$$\mathbf{G}_J^T\mathbf{G}_J\mathbf{m}_{MAP} = \mathbf{G}_J^T\tilde{\mathbf{d}}_J \tag{2.83}$$

which yields

$$\mathbf{m}_{MAP} = (\mathbf{G}_J^T\mathbf{G}_J)^{-1}\mathbf{G}_J^T\tilde{\mathbf{d}}_J. \tag{2.84}$$

In the linear problem, $\Theta_L(\mathbf{m})$ is expressed as Eq. (2.48). Simply using Eq. (2.48) (replacing $\mathbf{A}$ with $\mathbf{J}$ and $\mathbf{d}$ with $\mathbf{d}'$) when calculating the ABIC can lead to unacceptable linearization error (Mitsuhata and Uchida [2002]). To account for the non-linear forward model within the ABIC approach, Mitsuhata and Uchida [2002] proposed a quasi-linearized approach to the inversion where the objective function, $\Theta_{QL}(\mathbf{m})$, is

$$\Theta_{QL}(\mathbf{m}) = (\mathbf{d} - \mathbf{d}(\mathbf{m}))^T\mathbf{C_d}'^{-1}(\mathbf{d} - \mathbf{d}(\mathbf{m})) + \mu(\mathbf{m} - \hat{\mathbf{m}})^T\mathbf{C_{\hat{m}}}'^{-1}(\mathbf{m} - \hat{\mathbf{m}}). \tag{2.85}$$

This equation is described as quasi-linear because it uses both non-linear terms ($\mathbf{d}$ and $\mathbf{d}(\mathbf{m})$ are used rather than $\mathbf{d}'$ and $\mathbf{J}\mathbf{m}$) and linearized terms ($\mathbf{m}$ is calculated using a linearized inversion technique).

The derivation for the ABIC equation, which incorporates $\Theta_{QL}(\mathbf{m})$ from Eq. (2.85) and $\mathbf{G}_J$ from Eq. (2.82) follows directly from the derivation in Section 2.3, yielding

$$\mathrm{ABIC}_{QL} = N\log_e\big(2\pi\sigma_0^2\big) - 2\log_e|\mathbf{C_d}^{-1/2\prime}| - M\log_e\big(\mu\big) - 2\log_e|\mathbf{C_{\hat{m}}}^{-1/2\prime}| + \frac{\Theta_{QL}(\mathbf{m}_{MAP})}{\sigma_0^2} + \log_e|\mathbf{G}_J^T\mathbf{G}_J| + 2N_H. \quad (2.86)$$

Similar to Eq. (2.74), σ_0^2 is expressed as

$$\sigma_0^2 = \frac{\Theta_{QL}(\mathbf{m}_{MAP})}{N}. \quad (2.87)$$

This yields an expression for ABIC_{QL} which is only dependent on μ:

$$\mathrm{ABIC}_{QL} = N\log_e\big(\frac{2\pi\Theta_{QL}(\mathbf{m}_{MAP})}{N}\big) - 2\log_e|\mathbf{C_d}^{-1/2\prime}| - M\log_e\big(\mu\big) - 2\log_e|\mathbf{C_{\hat{m}}}^{-1/2\prime}| + N + \log_e|\mathbf{G}_J^T\mathbf{G}_J| + 2N_H. \quad (2.88)$$

Using an arbitrary starting model $\mathbf{m}_0$ (ideally chosen close to the true model), $\mathbf{J}(\mathbf{m}_0)$ and $\mathbf{d}(\mathbf{m}_0)$ are calculated. A line search over μ is then performed. For each value of μ there is a different $\mathbf{m}_{MAP}$, and therefore a different value of $\Theta_{QL}(\mathbf{m}_{MAP})$ and the ABIC. The $\mathbf{m}_{MAP}$ which minimizes the ABIC is the optimum solution for this iteration. The next iteration is initiated with $\mathbf{m}_0 \leftarrow \mathbf{m}_{MAP}$. This process continues until $\mathbf{m}_{MAP}$ converges. Once convergence is achieved, σ_0^2 is calculated from Eq. (2.87) and $\mathbf{C_m}$ from

$$\mathbf{C_m} = \sigma_0^2(\mathbf{J}^T\mathbf{C_d}'^{-1}\mathbf{J} + \mu\mathbf{C_{\hat{m}}}'^{-1})^{-1}. \quad (2.89)$$

In summary, the steps to perform ABIC linearized Bayesian inversion are:

1. Define $\hat{\mathbf{m}}$, $\mathbf{C_d}'$, $\mathbf{C_{\hat{m}}}'$, and $\mathbf{m}_0$
2. Calculate $\mathbf{J}(\mathbf{m}_0)$ (Eq. (2.79)) and $\mathbf{d}'$ (Eq. (2.80))
3. Perform a line search over μ to minimize ABIC_{QL} (Eq. (2.88))
4. Set the model whose μ value minimizes $ABIC_{QL}$ ($\mathbf{m}_{MAP}$) to $\mathbf{m}_0$, repeat from step 2 until $\mathbf{m}_{MAP}$ converges
5. Calculate σ_0^2 (Eq. (2.87)) and $\mathbf{C_m}$ (Eq. (2.89))

2.5 Relative Call Location Error

The geographic (absolute) uncertainty for an estimated source position along a track is influenced by uncertainties of both the data (i.e., arrival times) and prior information (e.g., hydrophone positions). Depending on the localization application, either absolute or relative localization uncertainty may be more relevant. Absolute localization uncertainty is useful in cases where the actual position of the sound source is important (e.g., assessing how close a swimming walrus approaches to an underwater sound source). Absolute localization uncertainty is available directly from the main diagonal elements of $\mathbf{C_m}$. Relative uncertainty (uncertainty in the position of one source relative to another) is less a function of systemic localization errors (i.e., those which tend to shift the track as a whole rather than individual source locations) than absolute uncertainty, and thus could be useful in cases where absolute source locations are not needed (e.g., estimating source velocity). This section will present a method of estimating relative uncertainty using $\mathbf{C_m}$.

Relative call uncertainty, σ^2_{pq}, is defined as

$$\sigma^2_{pq} = \left\langle \left[(m_p - \langle m_p \rangle) - (m_q - \langle m_q \rangle)\right]^2 \right\rangle . \tag{2.90}$$

For example, the relative error variance between the y-coordinates of the third and fourth source is

$$\sigma^2_{y3,y4} = \left\langle \left[(y_3 - \langle y_3 \rangle) - (y_4 - \langle y_4 \rangle)\right]^2 \right\rangle . \tag{2.91}$$

The expression in Eq. (2.90) can be simplified to consist only of values from $\mathbf{C_m}$:

$$\begin{aligned}\sigma^2_{pq} = \langle \Big(m_p - \langle m_p \rangle\Big)^2 + \Big(m_q - \langle m_q \rangle\Big)^2 \\ - 2\Big(m_p m_q - m_p \langle m_q \rangle - m_q \langle m_p \rangle + \langle m_p \rangle \langle m_q \rangle\Big)\rangle,\end{aligned} \tag{2.92}$$

which leads to

$$\sigma^2_{pq} = C_{m,p,p} + C_{m,q,q} - 2C_{m,p,q}, \tag{2.93}$$

where $C_{m,p,p}$ is the posterior variance of m_p, $C_{m,q,q}$ is the posterior variance of m_q, and $C_{m,p,q}$ is the covariance of m_p and m_q.

Chapter 3

Simulation Study

3.1 Simulation Conditions

To examine the effectiveness of the ABIC linearized Bayesian inversion algorithm in a way not possible with measured data, a series of simulations were run. Each of these simulations was based on a set of 11 acoustic transmissions from a moving source near an array of three receivers (A, B, and C). Two different sets of arrival paths were used to generate the results in this chapter which are referred to as Small Set and Large Set. Small Set is composed of 15 arrival paths from each transmission: 7 arriving at hydrophone A, and 4 arriving at hydrophones B and C as given in Table 3.1. Small Set was designed to approximately emulate the arrivals identified in the measured data (described in Chapter 5). Large Set consists of 24 arrival paths from each transmission: 8 arriving at each of the three hydrophones as given in Table 3.2. Large set was designed to examine whether inversion results improved significantly if more arrival paths could be identified.

Hydrophone A	**Hydrophone B**	**Hydrophone C**
D	D	D
BS	BS	-
SBS	-	-
BSBS	BSBS	BSBS
SBSBS	SBSBS	SBSBS
BSBSBS		BSBSBS
BSBSBSBS	-	-

Table 3.1: Small Set arrival paths for each hydrophone.

Hydrophone A	**Hydrophone B**	**Hydrophone C**
D	D	D
BS	BS	BS
SBS	SBS	SBS
BSBS	BSBS	BSBS
SBSBS	SBSBS	SBSBS
BSBSBS	BSBSBS	BSBSBS
SBSBSBS	SBSBSBS	SBSBSBS
BSBSBSBS	BSBSBSBS	BSBSBSBS

Table 3.2: Large Set arrival paths for each hydrophone.

The transmission locations, environmental conditions, and receiver positions were selected to approximate those of the measured data. Figures 3.1 and 3.2 show the simulated transmission locations, hydrophone locations, and water depth. Simulations using the ray tracing model use the SSP shown in Fig. 3.3. The same SSP is used for the measured data analysis in Chapter 6. This profile was measured several days before, and approximately 110 km away from, the data collection time and location described in Chapter 4. This represents the only available SSP measurement and is believed to be representative of the SSP at the recording site, although some differences are possible.

Due to the linearized nature of the inversion algorithm (described in Section 2.4), linearization error may bias the model estimates and the posterior model covariance matrix. A Monte Carlo analysis is performed here to determine the effect of linearization error on the calculated posterior uncertainties. This analysis provides a non-linear estimate of the posterior uncertainties. Additionally, these simulations are used investigate the difference in results if simulated data, computed using the curving-ray propagation model and the SSP in Fig. 3.3, are inverted using the straight-line propagation model (i.e. a constant sound speed over the water column). To carry out this analysis, noise-free direct and interface-reflected arrival times were first computed using the curving-ray propagation model. To allow a statistical analysis of the results, random errors were applied to these data to yield a total of 1000 independant, noisy data sets for each of Small Set and Large Set. Each of these data sets was inverted individually to produce the results shown in this chapter. These errors were drawn from zero-mean Gaussian distributions with the same standard deviations estimated from the measured data. During the data processing phase of this work (Chapter 5), different arrival paths and different hydrophones were found

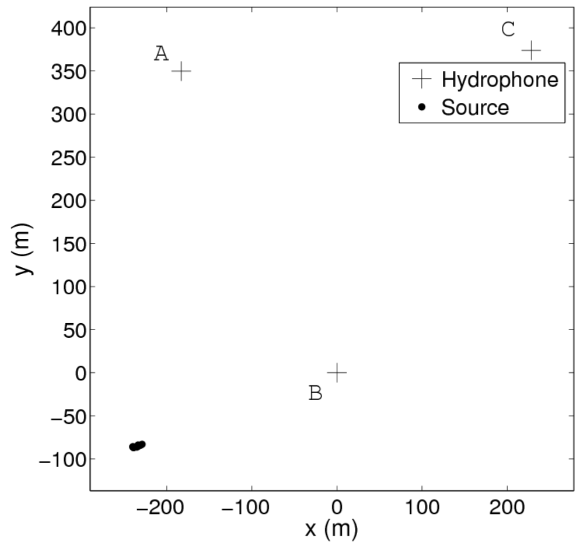

Figure 3.1: Transmission and receiver horizontal locations used for simulations in this chapter. Hydrophones A, B, and C are labeled.

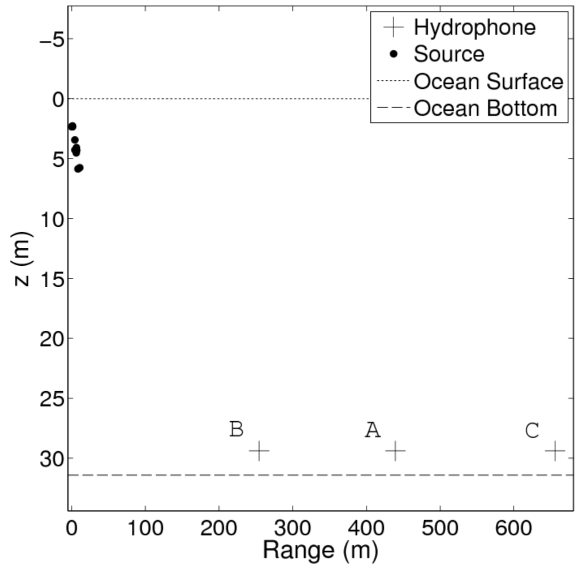

Figure 3.2: Transmission and receiver horizontal ranges (measured from the first transmission location) and depths used for simulations in this chapter. Hydrophones A, B, and C are labeled.

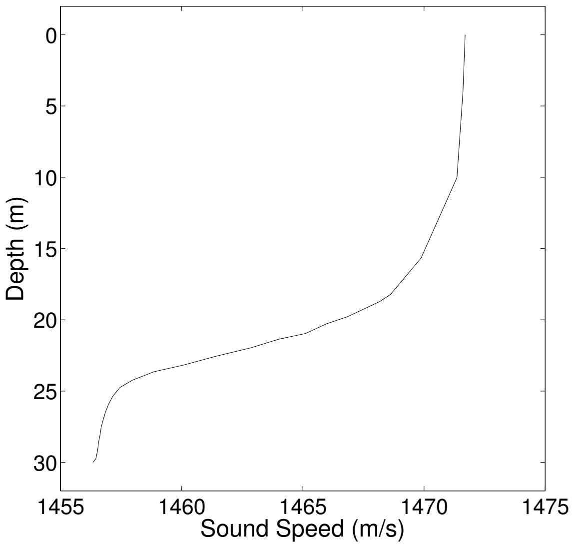

Figure 3.3: Sound speed profile used for all localizations using the curving-ray propagation model in this thesis.

Arrival Path Type	Hydrophone A	Hydrophone B	Hydrophone C
D	0.6	0.2	0.4
BS	0.8	0.4	0.4
SBS	0.5	0.6	-
BSBS	0.9	0.3	0.4
SBSBS	0.5	0.4	0.4
BSBSBS	0.9	-	0.4
BSBSBSBS	0.9	-	-

Table 3.3: Estimated arrival time uncertainties in milliseconds for the Hanna Shoal data set. The '-' symbols indicate that the arrival path was not picked in the measured data for the hydrophone in question.

to have different arrival time uncertainties, varying from 0.2–0.9 ms. Table 3.3 lists the estimated arrival time uncertainties for each hydrophone and arrival path. For both the simulation and measured data inversions in this thesis, the error covariance weighting matrix ($\mathbf{C_d}'$) consists of the arrival time uncertainties estimated from the measured data. For the cases where an arrival path was used for simulations but not identified in the measured data (e.g., the BSBSBS path at hydrophone B), the uncertainty for that arrival path at hydrophone A was used (if it was picked). Otherwise, the uncertainty for a nearby arrival path was used. For example, the SBSBSBS arrival path is used in Large Set but was not identified in the data from any of the three hydrophones. For this path, the arrival time uncertainty of BSBSBS was used.

Parameter	**True Value**	**Prior Uncertainty** (σ)
A [X,Y,Z]	[-182.9, 349.8, 29.39] m	[10, 10, 2] m
B [X,Y,Z]; τ_B	[0, 0, 29.39] m; 0 s	[10, 10, 2] m; 1 s
C [X,Y,Z]; τ_C	[228.3, 373.9, 29.39] m; 0 s	[10, 10, 2] m; 1 s
Water Depth	31.40 m	2 m
Sound Speed Offset	0 m/s	2 m/s
Sound Speed (straight-line)	1466.3 m/s	2 m/s

Table 3.4: True values and prior uncertainties for hydrophone locations and environmental parameters for simulations using the curving-ray propagation model. A, B, and C refer to hydrophones labeled in Fig. 3.1.

Prior estimates and uncertainties for model parameters (inter-hydrophone time synchronization factors, receiver locations, water depth, and sound speed offset) are used to include these parameters in the inversion and account for their uncertainties in the source location uncertainty estimates. For these simulations, the prior estimates consist of the true values with errors drawn from zero-mean Gaussian distributions. True values and prior uncertainties are listed in Table 3.4. In this table, τ refers to the inter-hydrophone time synchronization factor (defined to be zero for hydrophone A). Prior estimates for transmission locations, source times, and time synchronization factors are given very large uncertainties (10^5 m, 70 s, and 1 s) so as not to significantly bias the final result while not being infinite (which could cause numerical problems). For inversions employing straight-line ray paths, the harmonic mean of the SSP for a ray traversing the entire water column (1466.3 m/s) was chosen as the true uniform sound speed. This was done so that comparisons between the curving-ray and straight-line results could be made using a relatively small sound speed uncertainty (2 m/s) representative of calibration uncertainty for a measured SSP. In practical cases where an unknown SSP is represented by a uniform sound speed, a larger uncertainty would likely be used. Unless otherwise stated, the above conditions were used for all the simulations presented in this chapter.

3.2 Effect of Propagation Model

For some localization applications, a reliable SSP may not be available. In others, such as that discussed in Chapter 6, the measured SSP (Fig. 3.3) may be collected some time and distance from the source transmission. This could cause significant differences between the measured SSP and that present at the transmission location and time. In the absence of a reliable SSP, a common practice is to assume a uniform SSP with depth (e.g., Cummings and Holliday [1985], Freitag and Tyack [1993], Laurinolli et al. [2003]). To examine the effect of using an incorrect SSP on localization errors, each of the 1000 data sets in Small Set (described in Section 3.1) was inverted individually using the ABIC linearized Bayesian inversion algorithm and either the straight-line (i.e., uniform SSP) or curving-ray (i.e., depth-dependent SSP) propagation model. A histogram of the estimated x coordinate of the first transmission of the source over the set of 1000 independent inversions using both curving and straight rays is shown in Fig. 3.4. The standard deviation of this set was calculated, yielding an empirical (Monte Carlo) estimate of the posterior uncertainty. The ○ symbols show one standard deviation above and below the true value. Analytic uncertainties (+ symbols) are the square root of the diagonal entry of the posterior model covariance matrix. Figure 3.5 and 3.6 display the same information for the first transmission y and z coordinates, respectively.

Table 3.5 lists the empirical and analytic uncertainties from Figs. 3.4–3.6. These results are representative of those for all source transmissions along the track. The difference between the analytic and empirical uncertainty estimates gives an indication of the significance of linearization error. While linearization error causes the difference between analytic and empirical uncertainties for the curving-ray case, differences between the curving-ray and straight-line propagation models mean that linearization error is not necessarily the sole cause of the discrepancies in the estimated straight-line uncertainties. For the curving-ray case, differences between analytic and empirical uncertainties for x (1.4 m or 9%), y (8.2 m or 26%), and z (-0.07 m or -11%), while significant, are small enough that the linearized approximation is very useful. In other words, the analytic (i.e., linearized) uncertanties provide a good estimate of the empirical (i.e., non-linear) uncertainties for the curving-ray case. While the differences between analytic and empirical uncertainties for the straight-line case are slightly larger than those for the curving-ray results, the analytic uncertainties are still a reasonable approximation.

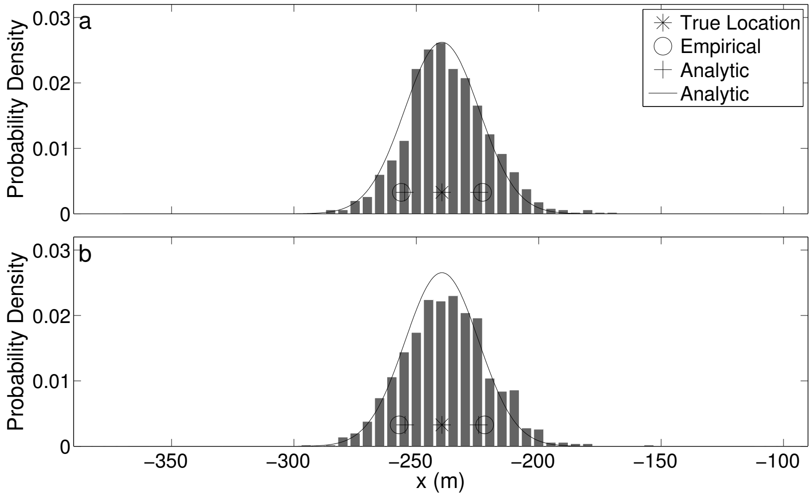

Figure 3.4: Normalized histogram of estimated x coordinates for the first transmission calculated through inversion of 1000 independent noisy data sets. The solid curve is a normalized Gaussian distribution with mean equal to the true x value and standard deviation equal to the analytic uncertainty estimate. (a) Curving-ray inversion of curving-ray data. (b) Straight-line inversion of curving-ray data.

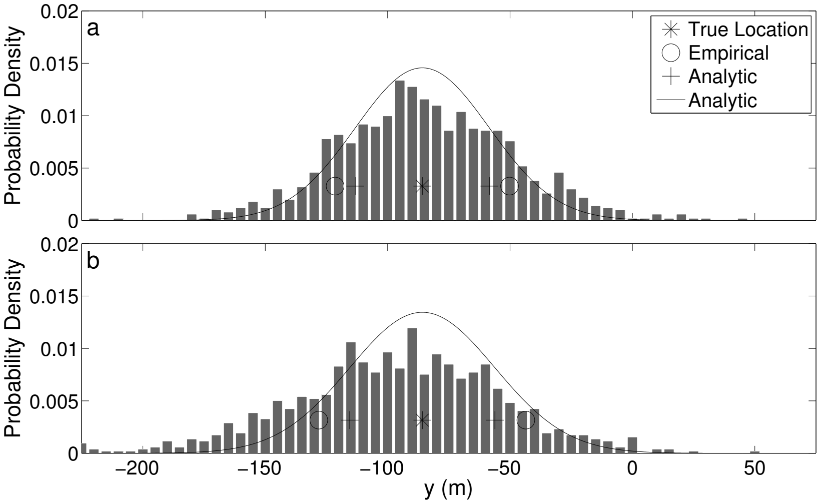

Figure 3.5: Normalized histogram of estimated y coordinates for the first transmission calculated through inversion of 1000 independent noisy data sets. The solid curve is a normalized Gaussian distribution with mean equal to the true y value and standard deviation equal to the analytic uncertainty estimate. (a) Curving-ray inversion of curving-ray data. (b) Straight-line inversion of curving-ray data.

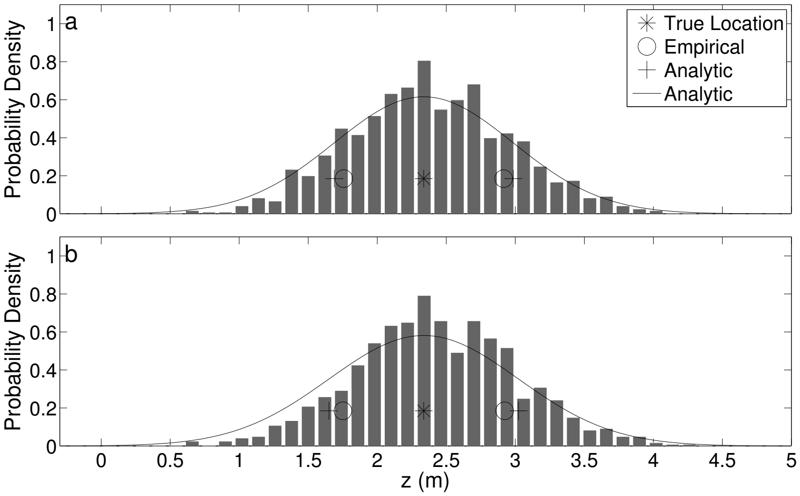

Figure 3.6: Normalized histogram of estimated z coordinates for the first transmission calculated through inversion of 1000 independent noisy data sets. The solid curve is a normalized Gaussian distribution with mean equal to the true z value and standard deviation equal to the analytic uncertainty estimate. (a) Curving-ray inversion of curving-ray data. (b) Straight-line inversion of curving-ray data.

Parameter	**Straight-Line, Analytic**	**Straight-Line, Empirical**
x_1	15.0 m	17.5 m
y_1	29.7 m	42.3 m
z_1	0.69 m	0.59 m
	Curving-Ray, Analytic	**Curving-Ray, Empirical**
x_1	15.2 m	16.6 m
y_1	27.4 m	35.6 m
z_1	0.65 m	0.58 m

Table 3.5: Empirical and analytic uncertainties (standard deviations) for the first transmission, corresponding to the figures shown in Section 3.2.

Parameter	**Bias, Straight**	σ_{SEM}**, Straight**	**Bias, Curving**	σ_{SEM}**, Curving**
x_1	1.83 m	0.55 m	2.31 m	0.52 m
y_1	-10.05 m	1.34 m	0.82 m	1.13 m
z_1	0.081 m	0.018 m	0.039 m	0.018 m

Table 3.6: Bias and standard error on the mean (σ_{SEM}) for the first transmission location. Inversion results for both straight-line and curving-ray inversion are shown.

The estimated bias and the uncertainty of this bias (the standard error on the mean, σ_{SEM}) are given in Table 3.6 for the x, y, and z location of the first transmission, computed from the 1000 noisy simulated data sets. These values are representative of those for all transmissions along the track. Figure 3.7 shows the x, y, and z biases for both the straight-line and curving-ray results. The results show that there are significant biases present in both the straight-line and curving-ray results except for the y results for the curving-ray case. The x and z biases are small and similar for the curving-ray and straight-line results. The straight-line y bias is much larger than, and of opposite sign to, the curving-ray value. Except for the x results, the straight-line bias is larger than the curving-ray bias with a large difference for y. Since both the straight-line and curving-ray biases are much less than the absolute posterior uncertainties (Table 3.5), they should not significantly diminish the confidence in the estimated transmission location for this case.

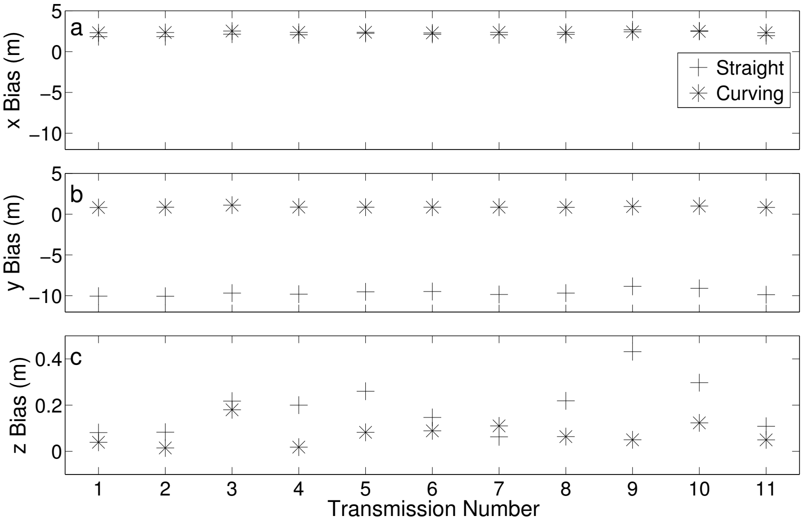

Figure 3.7: Differences between the average estimated transmission (a) x, (b) y, and (c) z values and the true values. Results for both straight-line and curving-ray inversion of Small Set are shown.

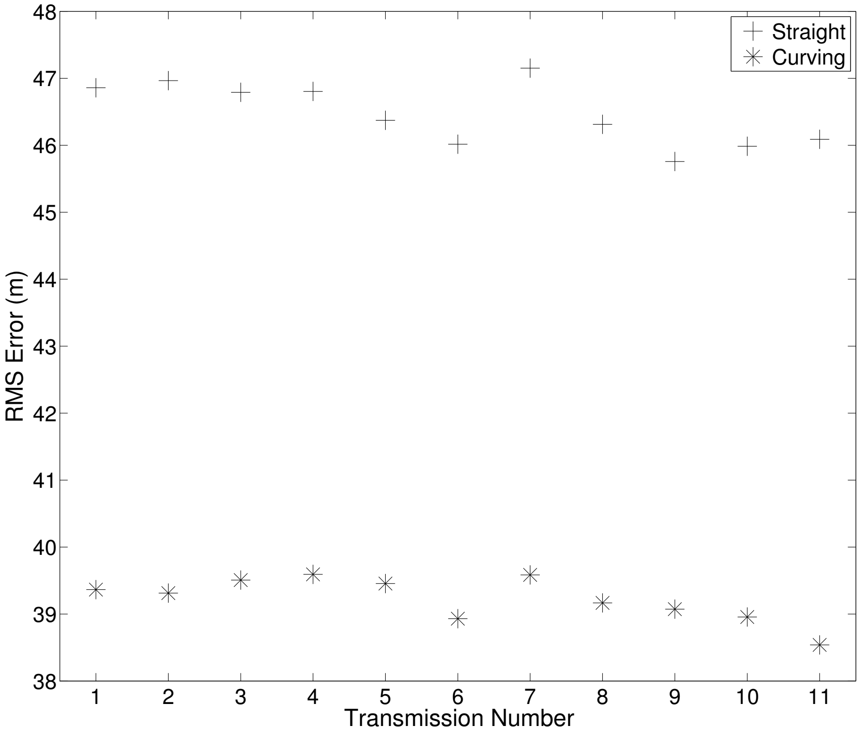

Figure 3.8: 3D RMS error for each transmission and propagation model calculated over the 1000 independent noisy data sets from Small Set.

To more closely examine the differences in curving-ray vs. straight-line inversion results, the 3D RMS error ($E_{RMS,3D}$)

$$E_{RMS,3D} = \Big[\sum_{i=1}^{R}\Big((x_i - x_t)^2 + (y_i - y_t)^2 + (z_i - z_t)^2\Big)/R\Big]^{1/2} \tag{3.1}$$

is calculated for each transmission location and propagation model. In Eq. (3.1), R is the number of noisy data sets, $\big(x_i, y_i, z_i\big)$ is the estimated transmission location for the i^{th} data set, and $\big(x_t, y_t, z_t\big)$ is the true source position. The 3D RMS error ($E_{RMS,3D}$) for each transmission and propagation model is shown in Fig. 3.8. Curving-ray inversion $E_{RMS,3D}$ is 8 m (19%) less than than straight-line $E_{RMS,3D}$.

The following equation is used to calculate RMS depth error:

$$E_{RMS,depth} = \Big[\sum_{i=1}^{R}\Big(z_i - z_t\Big)^2/R\Big]^{1/2}. \tag{3.2}$$

The RMS depth error for each transmission and propagation model is shown in Fig.

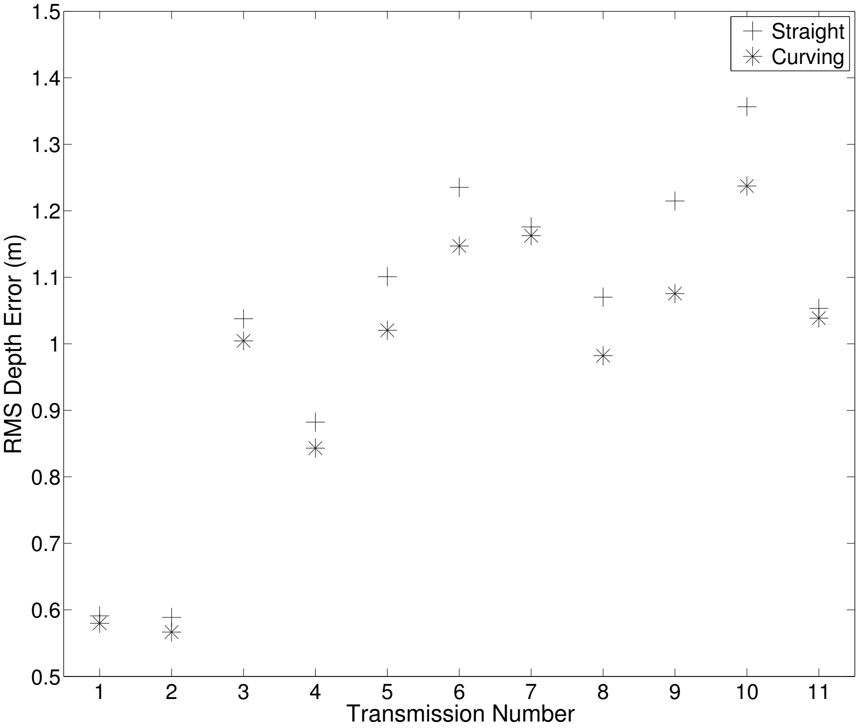

Figure 3.9: RMS depth error for each transmission and propagation model calculated over the 1000 independent noisy data sets from Small Set.

3.9. Curving-ray RMS depth error is 0.01–0.14 m (2–13%) less than straight-line RMS depth error. To calculate RMS range error, the following equation is used:

$$E_{RMS,range} = \Big[\sum_{i=1}^{R} \Big((x_i - x_t)^2 + (y_i - y_t)^2 \Big) / R \Big]^{1/2}. \tag{3.3}$$

The calculated RMS range errors (not shown) are not noticably different from the RMS errors depicted in Fig. 3.8, indicating that 3D RMS error is more strongly influenced by errors in the x and y transmission locations than in z errors.

Parameter	**Bias, Straight**	σ_{SEM}, **Straight**	**Bias, Curving**	σ_{SEM}, **Curving**
Water Depth	0.43 m	0.043 m	−0.042 m	0.035 m
Sound Speed	0.059 m/s	0.061 m/s	−0.0070 m/s	0.065 m/s
Source 1 Time	−7.4 ms	0.86 ms	0.46 ms	0.71 ms
X_A	−0.69 m	0.32 m	0.33 m	0.31 m
Y_A	0.29 m	0.32 m	0.0028 m	0.34 m
Z_A	0.066 m	0.062 m	−0.020 m	0.065 m
X_B	0.60 m	0.31 m	−0.12 m	0.31 m
Y_B	0.73 m	0.33 m	−0.18 m	0.32 m
Z_B	0.082 m	0.061 m	−0.0092 m	0.062 m
τ_B	3.4 ms	0.44 ms	−0.16 ms	0.36 ms
X_C	−1.45 m	0.31 m	−0.14 m	0.32 m
Y_C	−0.91 m	0.31 m	−0.12 m	0.30 m
Z_C	0.30 m	0.060 m	−0.0043 m	0.062 m
τ_C	3.6 ms	0.27 ms	0.88 ms	0.26 ms

Table 3.7: Bias and standard error on the mean (σ_{SEM}) for nuisance parameters. Inversion results for both straight-line and curving-ray inversion are shown. A, B, and C refer to hydrophones labeled in Fig. 3.1.

3.3 Nuisance Parameter Results

While the main objective of this inversion approach is to estimate sound source locations, several nuisance parameters are also estimated. These parameters include water depth, sound speed offset, source time, hydrophone locations, and inter-hydrophone time synchronization factors. This section considers simulation results examining the ability of the localization algorithm to estimate these nuisance parameters while simultaneously estimating transmission locations. Small Set (15 arrival paths per transmission) is used for inversions in this section. Table 3.7 summarizes the bias and standard error on the mean for the results in this section.

Histograms of estimated water depth values using both curving-ray and straight-line inversion are shown in Fig. 3.10. Based on the standard error on the mean for the straight-line (0.043 m) and curving-ray (0.035 m) cases, the 0.43 m bias in the straight-line results is significant whereas the curving-ray bias of −0.042 m is not necessarily significant. The bias toward larger water depth in the straight-line case could be caused by the inversion preferring larger ray path lengths for curving rays compared to straight-line propagation. To fit to the curving-ray data, the straight-line algorithm may increase the water depth, thereby increasing the path length and travel time. The decrease from the prior uncertainty (2 m) to the empirical posterior

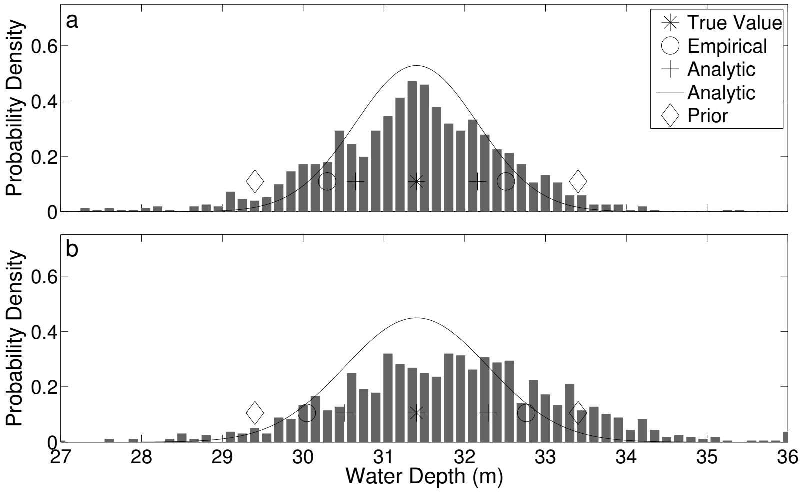

Figure 3.10: Histograms showing true and estimated water depth values for (a) curving-ray and (b) straight-line inversion. One standard deviation prior, empirical, and analytic uncertainties are shown centered on the true solution.

uncertainties (1.1 m and 1.4 m for the curving-ray and straight-line cases) suggests that the data contains some information regarding water depth. The empirical and analytic uncertainties for the straight-line case are slightly larger than those for the curving-ray case.

Histograms for the estimated sound speed offset are shown in Fig. 3.11 for curving-ray inversion and Fig. 3.12 for straight-line inversion. The lack of significant distinction between prior and posterior uncertainties in both these figures suggests that the data contain little information regarding sound speed compared to the prior information. For the curving-ray results, the standard error on the mean (0.065 m/s) indicates that the bias of −0.007 m/s is not significant. The standard error on the mean for the straight-line case (0.061 m/s) indicates that the bias of 0.059 m/s is not necessarily significant.

Estimated source times for the first transmission are shown in Fig. 3.13. Prior uncertainties (σ=70 s) are not shown on these plots. Based on the standard error on the mean for the straight-line (0.86 ms) and curving-ray (0.71 ms) cases, the bias in the curving-ray results of 0.46 m/s is not significant whereas the straight-line bias of −7.4 ms is significant. As is the case for the bias toward larger water depths, the bias toward earlier source times in the straight-line results serves to make travel times longer to compensate for the shorter travel times in straight-line propagation relative

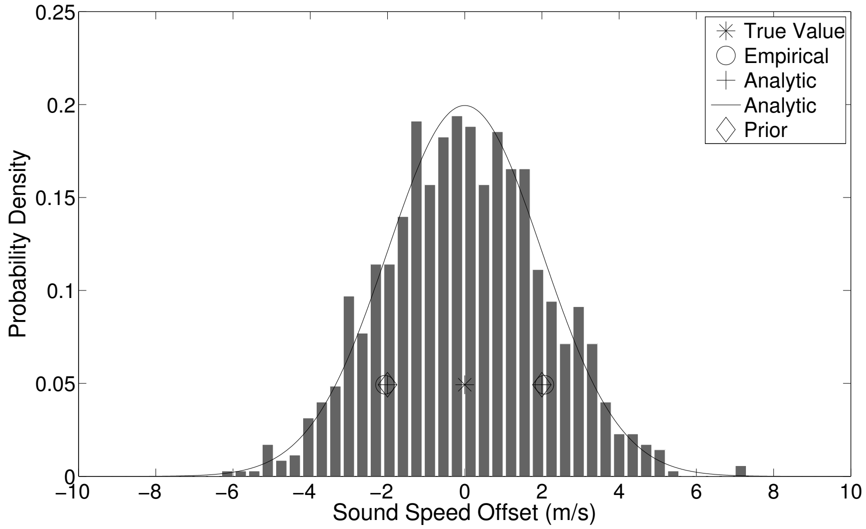

Figure 3.11: Histogram showing true and estimated sound speed offsets for curving-ray inversion. One standard deviation prior, empirical, and analytic uncertainties are shown centered on the true solution.

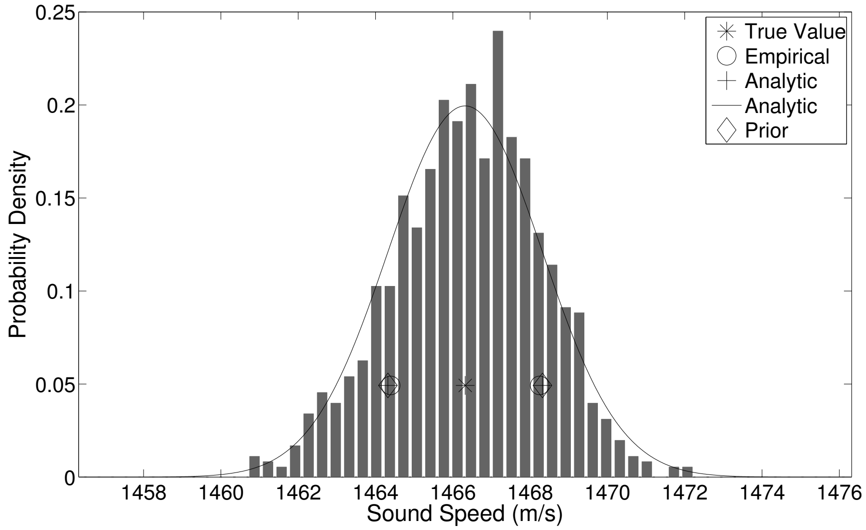

Figure 3.12: Histogram showing true and estimated sound speed for straight-line inversion. One standard deviation prior, empirical, and analytic uncertainties are shown centered on the true solution.

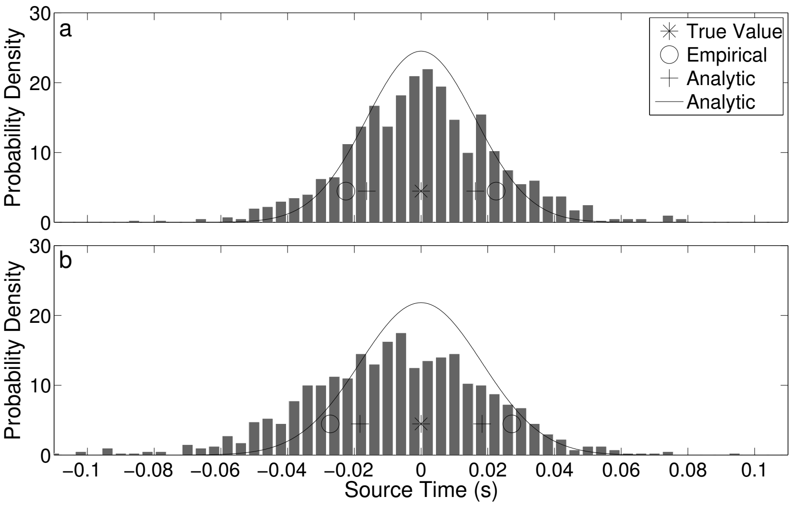

Figure 3.13: Histograms showing true and estimated source times for the first transmission and (a) curving-ray and (b) straight-line inversion. One standard deviation empirical, and analytic, uncertainties are shown centered on the true solution. Prior uncertainties of ±70 s relative to the true solution are omitted from these plots.

to curving-ray travel times.

Estimated hydrophone B time synchronization factors (τ_B) are shown in the histograms in Fig. 3.14. Curving-ray and straight-line analytic uncertainties are similar. The bias of 3.4 ms for the straight-line case is larger than that for the curving-ray results (−0.16 ms). Based on the standard error on the mean for the straight-line (0.44 ms) and curving-ray (0.36 ms) cases, the bias in the curving-ray results is not significant whereas the straight-line bias is significant. As shown in Table 3.7, there is a significant bias in the hydrophone C time synchronization factor, although the bias is less significant than the straight-line bias for this parameter.

Histograms for estimated hydrophone B X, Y, and Z coordinates are shown in Figs. 3.15–3.17. For all three of these cases, there is little difference between the prior, empirical, and analytic uncertainties, suggesting that the data contain little information on hydrophone position and that the prior information essentially determines the estimated values. Table 3.7 lists the bias and standard error on the mean for the X, Y, and Z cases. For the straight-line results, the bias in estimated X, Y, and Z values is likely significant in comparison to the standard error on the mean.

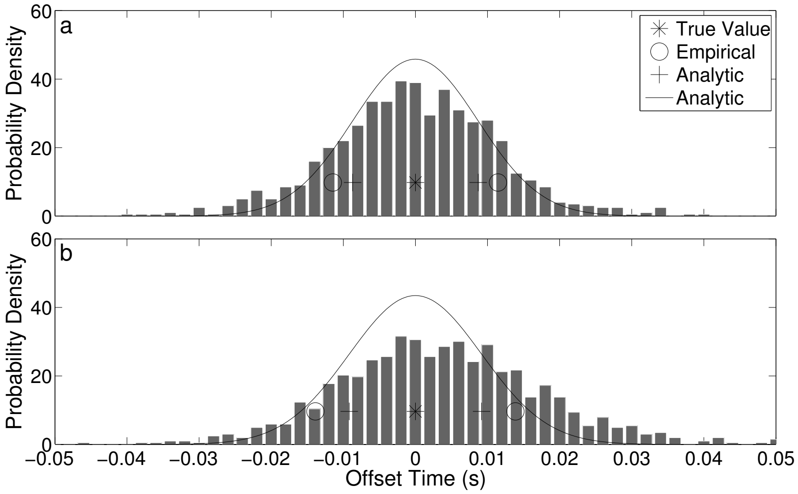

Figure 3.14: Histograms showing true and estimated hydrophone B time synchronization factors for (a) curving-ray and (b) straight-line inversion. One standard deviation empirical, and analytic, uncertainties are shown centered on the true solution. Prior uncertainties of ±1 s relative to the true solution are omitted from these plots.

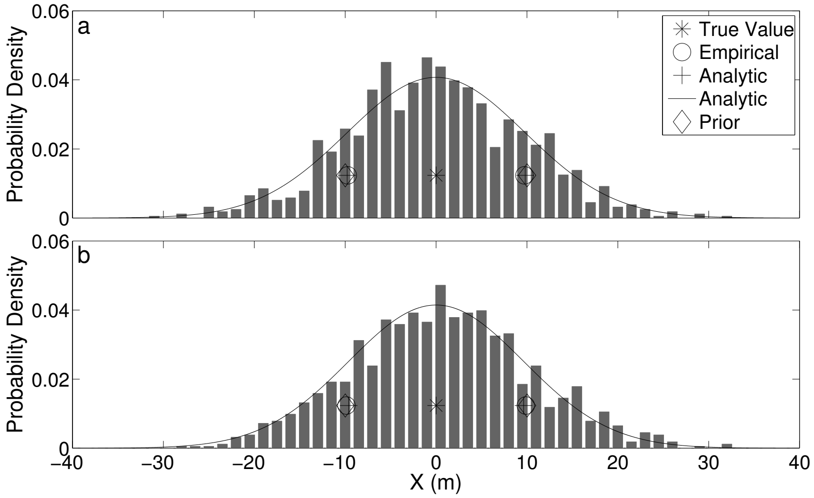

Figure 3.15: Histograms showing true and estimated hydrophone B X coordinate values for (a) curving-ray and (b) straight-line inversion. One standard deviation prior, empirical, and analytic uncertainties are shown centered on the true solution.

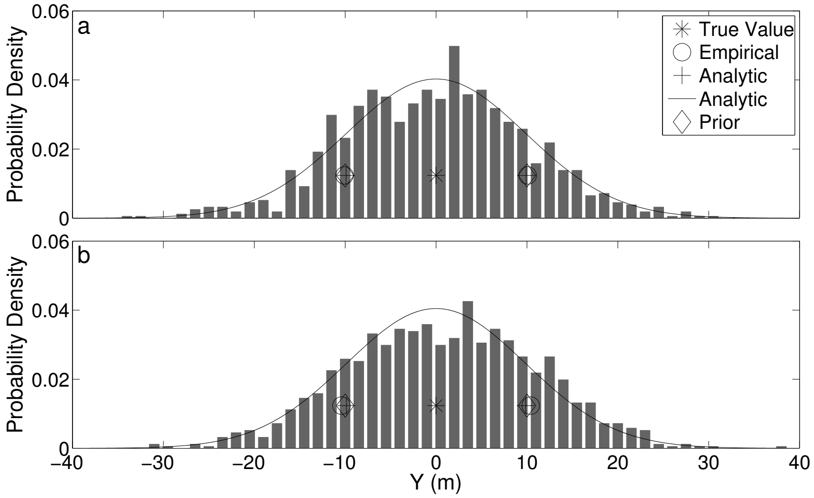

Figure 3.16: Histograms showing true and estimated hydrophone B Y coordinate values for (a) curving-ray and (b) straight-line inversion. One standard deviation prior, empirical, and analytic uncertainties are shown centered on the true solution.

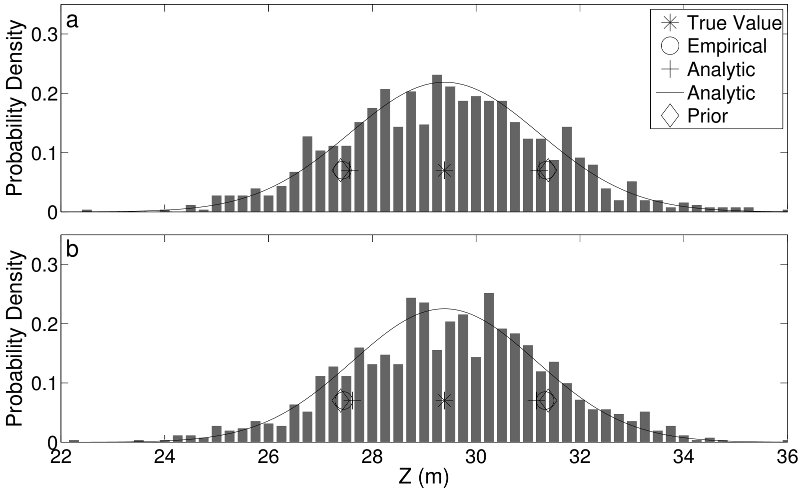

Figure 3.17: Histograms showing true and estimated hydrophone B Z coordinate values for (a) curving-ray and (b) straight-line inversion. One standard deviation prior, empirical, and analytic uncertainties are shown centered on the true solution.

Parameter	σ_e, **Straight**	σ_a, **Straight**	σ_e, **Curving**	σ_a, **Curve**
Water Depth	1.36 m	0.89 m	1.11 m	0.76 m
Sound Speed	1.93 m/s	2.00 m/s	2.06 m/s	2.00 m/s
Source 1 Time	27.2 ms	18.28 ms	22.52 ms	16.28 ms
X_A	10.04 m	9.92 m	9.92 m	9.91 m
Y_A	10.09 m	9.77 m	10.68 m	9.87 m
Z_A	1.97 m	1.78 m	2.05 m	1.89 m
X_B	9.86 m	9.62 m	9.72 m	9.79 m
Y_B	10.42 m	9.86 m	10.08 m	9.90 m
Z_B	1.94 m	1.77 m	1.96 m	1.82 m
τ_B	13.87 ms	9.18 ms	11.46 ms	8.71 ms
X_C	9.86 m	9.57 m	10.01 m	9.74 m
Y_C	9.75 m	9.52 m	9.39 m	9.74 m
Z_C	1.88 m	1.66 m	1.96 m	1.93 m
τ_C	8.41 ms	6.91 ms	8.30 ms	6.96 ms

Table 3.8: Empirical (σ_e) and analytic (σ_a) uncertainty estimates for straight-line and curving-ray inversion results. A, B, and C refer to hydrophones labeled in Fig. 3.1.

Table 3.8 summarizes the empirical and analytic uncertainty estimates for the nuisance parameters. Based on the similarity between empirical and analytic uncertainties for the curving-ray case, linearization error is small and analytic uncertainties provide a good approximation of the non-linear, empirical uncertainty. The differences between empirical and analytic uncertainties for the straight-line case tend to be larger than those for the curving-ray case. However, these differences are not so great as to render the analytic uncertainties useless.

3.4 Effect of Data Set Size

Increasing the number of arrival paths identified for a given source and included in the inversion is expected to reduce the posterior model uncertainty. To test whether this decrease is significant, inversion results using Small Set (15 arrivals per transmission, Table 3.1) and Large Set (24 arrivals per transmission, Table 3.2) are compared in this section.

Histograms for estimated x coordinates for the first transmission based on Large Set and Small Set are shown in Fig. 3.18. Both curving-ray and straight-line inversion results are shown. Histograms showing the same cases for y and z coordinates are shown in Figs. 3.19 and 3.20, respectively. Table 3.9 lists the posterior analytic and

Coordinate	**Propagation Model**	**Large Set**	**Small Set**
x_1	Curving-Ray	15.29 m, 13.75 m	16.6 m, 15.2 m
	Straight-Line	16.45 m, 13.97 m	17.48 m, 15.03 m
y_1	Curving-Ray	22.31 m, 17.44 m	35.63 m, 27.39 m
	Straight-Line	24.61 m, 17.66 m	42.28 m, 29.66 m
z_1	Curving-Ray	0.39 m, 0.36 m	0.58 m, 0.65 m
	Straight-Line	0.37 m, 0.40 m	0.59 m, 0.69 m

Table 3.9: Empirical (first number) and analytic (second number) posterior uncertainties in the first transmission x, y, and z values for both propagation models and data sets.

empirical uncertainties from Figs. 3.18–3.20. These results are typical of those for transmissions throughout the track. For all three transmission location coordinates (x, y, and z) and both propagation models, Large Set posterior uncertainties are smaller than those for Small Set. Also, the difference between Large Set and Small Set uncertainties, for a given propagation model, is greater than the difference in uncertainties between propagation models. Specifically, for curving-ray inversion, analytic uncertainty decreases by 10–40% between the Small Set and Large Set cases, whereas the difference between the curving-ray and straight-line analytic uncertainties for the Small Set case is −1–8%. The percent differences between Small and Large Set uncertainties were calculated using the equation

$$\%_{Diff} = \Big((\sigma_{Small} - \sigma_{Large})/\sigma_{Small}\Big) \times 100\%, \tag{3.4}$$

while the percent differences between propagation models were calculated using the equation

$$\%_{Diff} = \Big((\sigma_{Straight} - \sigma_{Curving})/\sigma_{Straight}\Big) \times 100\%. \tag{3.5}$$

These results show that the size of the data set being inverted can have a larger impact on the posterior uncertainties than the use of either a curving-ray or straight-line propagation model. However, it is unlikely that a data set with as many arrivals as Large Set can actually be picked for realistic data. Also, even though posterior uncertainties decreased by as much as 40% due to the additional arrivals in Large Set, Small Set uncertainties are likely small enough to give enough confidence in estimated transmission locations for many localization applications.

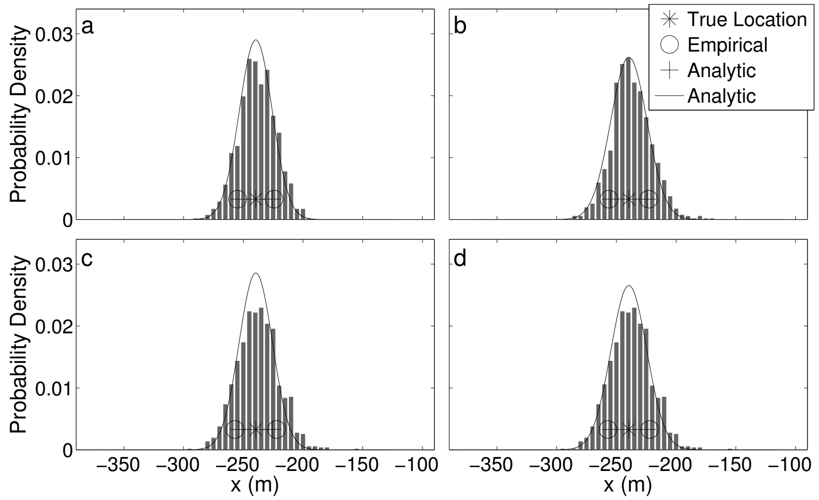

Figure 3.18: Histograms showing estimated x coordinate values for the first transmission. (a) Large Set using curving-ray inversion. (b) Small Set using curving-ray inversion. (c) Large Set using straight-line inversion. (d) Small Set using straight-line inversion.

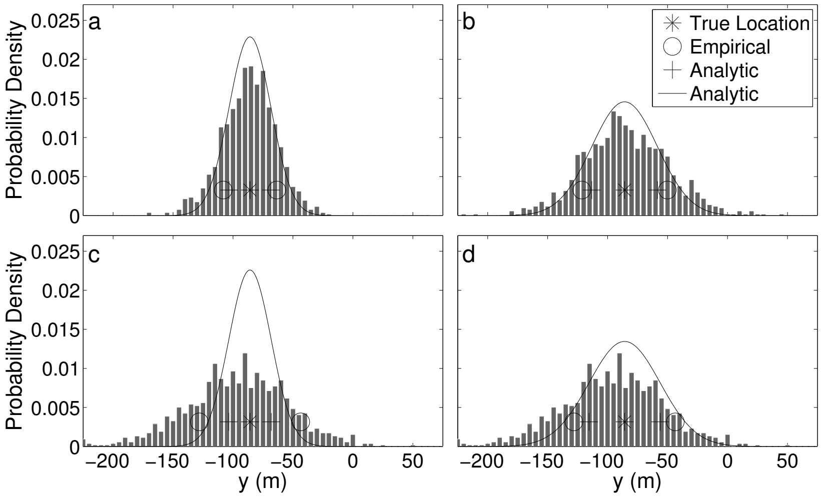

Figure 3.19: Histograms showing estimated y coordinate values for the first transmission. (a) Large Set using curving-ray inversion. (b) Small Set using curving-ray inversion. (c) Large Set using straight-line inversion. (d) Small Set using straight-line inversion.

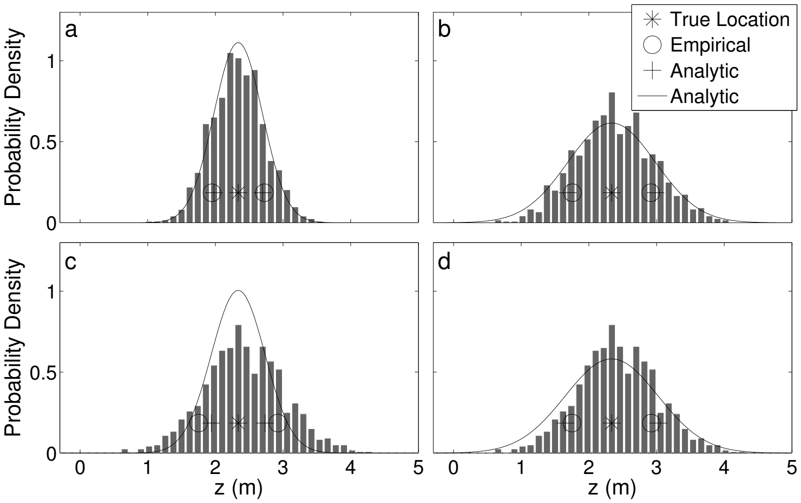

Figure 3.20: Histograms showing estimated z coordinate values for first transmission. (a) Large Set using curving-ray inversion. (b) Small Set using curving-ray inversion. (c) Large Set using straight-line inversion. (d) Small Set using straight-line inversion.

Parameter	**Bias, Small**	σ_{SEM}**, Small**	**Bias, Large**	σ_{SEM}**, Large**
x_1	2.31 m	0.52 m	1.13 m	0.48 m
y_1	0.82 m	1.13 m	-0.72 m	0.70 m
z_1	0.039 m	0.018 m	-0.0088 m	0.012 m

Table 3.10: Bias and standard error on the mean (σ_{SEM}) for the first transmission location. Inversion results for curving-line inversion of both Small Set and Large Set are shown.

Parameter	**Bias, Small**	σ_{SEM}**, Small**	**Bias, Large**	σ_{SEM}**, Large**
x_1	1.83 m	0.55 m	2.36 m	0.52 m
y_1	-10.05 m	1.34 m	3.32 m	0.78 m
z_1	0.081 m	0.019 m	0.026 m	0.012 m

Table 3.11: Bias and standard error on the mean (σ_{SEM}) for the first transmission location. Inversion results for straight-line inversion of both Small Set and Large Set are shown.

To investigate the effect of increasing the size of the inverted data set on estimated source location bias, the bias and standard error on the mean for the first transmission from both Small Set and Large Set are listed for curving-ray inversion in Table 3.10 and straight-line inversion in Table 3.11. Except for the straight-line x_1 bias, for both propagation models the size of the bias and σ_{SEM} for Large Set is smaller than the Small Set values. Additionally, with the exception of the y_1 curving-ray and x_1 straight-line bias, the size of the bias relative to σ_{SEM} decreases in going from Small Set to Large Set. While these results show that increasing the data set size can decrease both the size and significance of the bias, whether this modest decrease in bias warrents the added effort of picking a large data set even if this is possible depends on the specific localization application. For this work, a decrease in depth bias on the order of ~ 0.03 m (for curving-ray results) or ~ 0.05 m (for straight-line results) does not yield significantly more insight into walrus depth. Similarly, decreasing x and y bias by one or two meters will likely not give significantly more insight into walrus position.

On the whole, the results of this section show that while increasing the data set size reduces posterior uncertainties and tends to decrease the significance of estimated source location biases, the decreases in uncertainty and bias significance are not likely to yield significantly more insight into walrus position. Additionally, in most cases it will not be possible to pick so many arrivals.

3.5 Effect of Arrival Path Mislabeling

Localization, as implemented in this work, requires that arrivals be labeled according to their path (e.g., D, BS, SBS). If the arrivals are mislabeled, even though the inversion algorithm may converge to a solution, the estimated transmission locations may be substantially in error. As Chapter 5 shows, the process of assigning arrival path labels can be non-trivial. This section presents simulation results, using curving-ray inversion, which illustrate the effects of two types of path label mismatches on localization accuracy and uncertainty. As with the other results in this section, the ABIC linearized Bayesian inversion algorithm was used to perform localization. A potential method for identifying path mislabeling is also proposed. The same noisy data set was used for each of the cases considered here.

In this section, assumed arrival path labels are referred to as being offset by one or more arrival paths from the true labels. If arrival paths are listed by increasing path length, a single path offset shifts each of the true arrival path labels one entry longer on the path length ordered list (i.e., D → B, BS → BSB . . .). For the purposes of defining single and double-offsets in this chapter, the source is assumed to be deep enough that B arrivals reach the hydrophone before S arrivals. In other words, the source depth is assumed to be greater than the hydrophone elevation off the sea floor. Therefore, mistaking a D arrival for a B is defined as a single-offset, while mistaking D for S is a double-offset. For the measured data case (considered in Chapter 6) the fact that the hydrophones are within 2 m of the bottom suggests that, for the majority of potential source depths, this assumption should be appropriate.

The effects of a given arrival path offset are likely dependent on the arrival which is mislabeled as well as the degree of mislabeling. For example, if a D arrival is mistaken for an S, the resulting bias in estimated transmission location may be different than if an S is mistaken for a BS.

3.5.1 Single Arrival Path Offset

For a single arrival path offset, consider the two sets of arrival paths shown in Table 3.12. The 'True Arrivals' column lists accurate path labels for 7 arrival paths [D, BS, SBS, etc.]. Due to errors in the arrival path labeling process, these arrivals are given the labels in the 'Assumed Arrivals' column. A comparison of true transmission locations with those estimated using zero and single-offset arrival paths is shown in Fig. 3.21. Estimated x and y values (from the mislabeled data) have significantly

True Arrivals	Assumed Arrivals
D	B
BS	BSB
SBS	SBSB
BSBS	BSBSB
SBSBS	SBSBSB
BSBSBS	BSBSBSB
BSBSBSBS	BSBSBSBSB

Table 3.12: Comparison of true (i.e., zero arrival path offset) and assumed arrival path labels displaying a single arrival path offset.

larger errors than those estimated from correctly labeled arrivals. The errors in x and y for the single-offset data are larger than the analytic posterior uncertainties shown in Fig. 3.22. These errors could be due, in part, to arrival times tending to get closer together as the source moves away from the hydrophone. The source location whose B and BSB arrival times best fit the true D and BS arrival times will be further from the hydrophone than the true location, resulting in the single-offset estimated transmission locations being further from the hydrophone than the zero offset estimated locations. The single-offset z values are very similar to those estimated for the zero offset case. This similarity is likely due to the sign of the partial derivative of arrival time with respect to source depth being the same for the zero and single-offset cases considered here. For example, the first true arrival is D. Regardless of whether this arrival is assumed to be D or B, for source depths less than the hydrophone depth increasing the depth decreases the arrival time for both D and B arrivals.

Analytic posterior transmission location uncertainties for the zero and single-offset cases are shown in Fig. 3.22. Posterior x and y uncertainties for the single-offset case are slightly larger than those for the true arrival path labels, while z posterior uncertainties are similar for the two cases. This result is not unexpected. Variation in the Jacobian matrix ($\mathbf{J}$) and the relative error scale factor (σ_0^2) caused by path label mismatch can increase posterior uncertainties. However, the estimated posterior model covariance matrix in the presence of path label mismatch is likely not a reliable indication of posterior uncertainties. The derivation for the posterior model covariance matrix assumes that errors are zero-mean and Gaussian-distributed. Path label mismatch can cause errors which are strongly at odds with these assumptions, and hence the resulting model covariance matrix may be of little use.

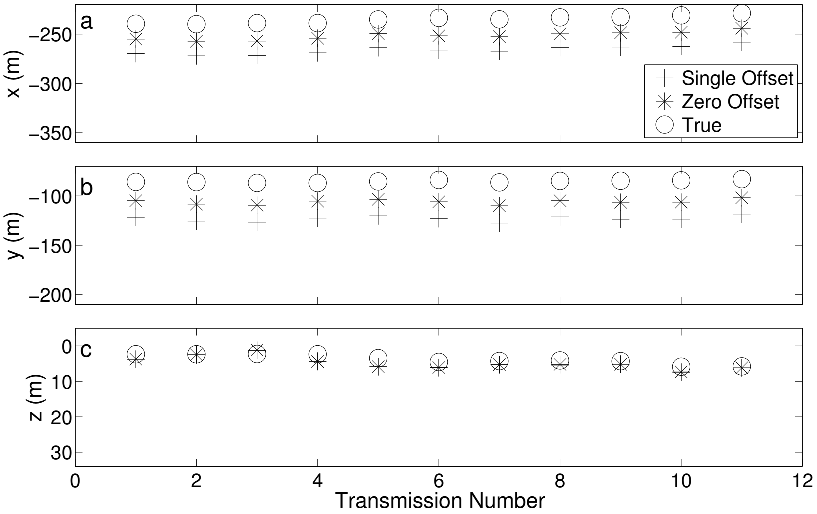

Figure 3.21: Comparison of true transmission positions with those estimated using the zero and single-offset arrival paths.

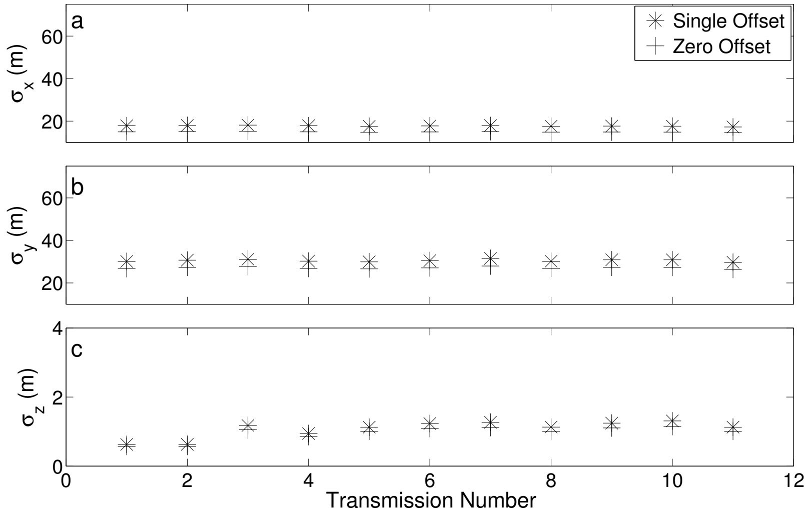

Figure 3.22: Comparison of posterior transmission location uncertainties for the zero and single-offset cases.

True Arrivals	Assumed Arrivals
D	S
BS	SBS
SBS	BSBS
BSBS	SBSBS
SBSBS	BSBSBS
BSBSBS	SBSBSBS
BSBSBSBS	SBSBSBSBS

Table 3.13: Comparison of true (i.e., zero arrival path offset) and assumed arrival path labels displaying a double arrival path offset.

3.5.2 Double Arrival Path Offset

Table 3.13 illustrates the case of assumed arrival path labels which are offset by two arrival paths compared to their true values. A comparison of true transmission locations with those estimated using zero and double-offset arrival paths is shown in Fig. 3.23. Source depth errors are larger for the double-offset case than for the single-offset case. Specifically, the z coordinate values seem to be mirrored about the middle of the water column ($\sim$ 15.5 m in this case). This mirroring is likely caused by the sign of the partial derivative of arrival time with respect to source depth being different between the zero and double-offset cases considered here. For example, consider a source shallower than the hydrophone depth; D arrival times will decrease with increasing depth while S arrival times will increase. The errors in x and y values are much larger for the double-offset than for the single-offset case, and are also much larger than the posterior uncertainties.

Posterior transmission location uncertainties for the zero and double-offset cases are shown in Fig. 3.24. Uncertainties for the double-offset case are larger than those for either the single or zero offset cases. As for the single-offset case, path label mismatch is expected to increase the posterior model covariance matrix, but these uncertainties will not fully express the posterior uncertainties because path mismatch likely causes errors which are neither zero-mean nor Gaussian-distributed.

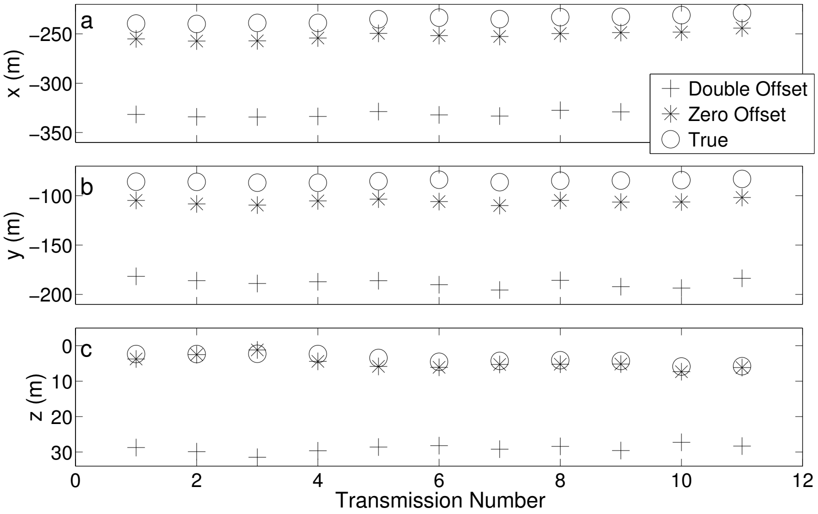

Figure 3.23: Comparison of true transmission positions with those estimated using the zero and double-offset arrival paths.

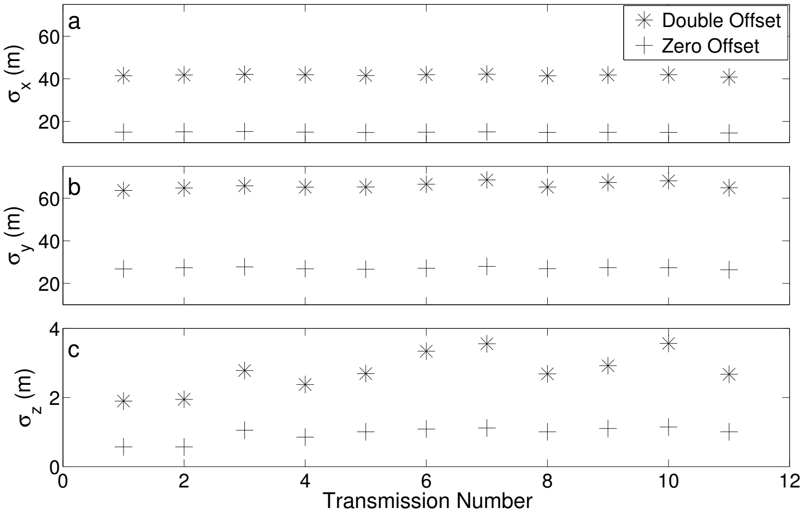

Figure 3.24: Comparison of posterior transmission location uncertainties for the zero and double-offset cases.

3.5.3 Arrival Path Mislabel Detection

Due to the large localization errors arrival path mislabeling can cause in estimated source locations, a method to check for mislabeling is sought. As mentioned earlier in this chapter, the posterior covariance matrix may not be reliable in the presence of mislabeling errors. Examining the difference between observed and model-predicted arrival times (i.e., the data residuals) is another way to potentially identify that arrival paths have been mislabeled. Data residuals (the difference between observed and model-predicted arrival times) for the arrivals of the first transmission at hydrophone A for the true, single, and double-offset cases are shown in Fig. 3.25. Similar trends are observed in the residuals for other transmissions and hydrophones. As expected, the zero-offset residuals are much smaller than either the single or double-offset residuals. For each of the seven arrivals in this figure, the magnitude of the single-offset residual is greater than the zero-offset residual. The sawtooth-like pattern in the double-offset residuals is likely a result of the apparent reflection of the estimated z values about the middle of the watern column, relative to the true values.

These observations suggest that data residuals can be used to identify the presence of arrival path mislabeling. However, it will not necessarily be straightforward to determine correct arrival path labels based on patterns in the data residuals. In practice, if arrival paths for measured data are mislabeled every arrival path may not be offset by the same number of arrival paths (e.g., early arrivals could have a double-offset while subsequent arrival labels could be accurate). Trying several arrival path labeling schemes, examining the data residuals for each scheme, and selecting the scheme based on physically-realizable arrivals which minimizes the data residuals should improve the accuracy of the arrival path labels, but can be time consuming if a large number of potential schemes are considered.

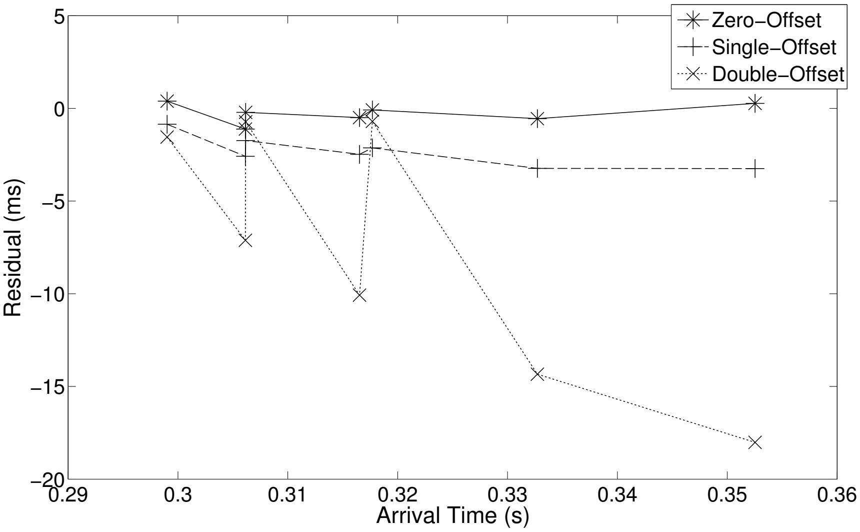

Figure 3.25: Comparison of data residuals for the arrivals of the first transmission at hydrophone A for the zero, single, and double-offset cases.

3.6 Relative Transmission Location Error

In Section 2.5, an analytic method for calculating the relative position error between transmissions based on the posterior model covariance matrix was presented. This section compares absolute and relative transmission uncertainties using Small Set. Additionally, to demonstrate the significance of linearization error, the analytic relative uncertainties are compared with those estimated through a non-linear Monte Carlo approach.

Relative and absolute uncertainties for each transmission in the track are shown in Fig. 3.26. Absolute x and y uncertainties are much larger than relative uncertainties, while relative z uncertainties are slightly larger than absolute uncertainties. The difference between horizontal (x and y) and z relative uncertainties compared to absolute uncertainties is caused by differences in the degree of correlation between consecutive transmission location estimates. The formula for calculating relative uncertainty given in Section 2.5 is repeated here:

$$\sigma_{pq}^2 = C_{m,p,p} + C_{m,q,q} - 2C_{m,p,q}, \tag{3.6}$$

where $C_{m,p,p}$ is the posterior variance of m_p, $C_{m,q,q}$ is the posterior variance of m_q, and $C_{m,p,q}$ is the covariance of m_p and m_q. The x and y transmission location estimates exhibit greater correlation than z estimates. In other words, the difference between z variances and covariances is greater than is the case for either x or y. Therefore, z relative uncertainties are larger, compared to absolute uncertainties, than is the case for x and y.

In Dosso and Ebbeson [2006] a method for calculating relative error estimates via Monte Carlo analysis is presented. Since both hydrophone and track positions will be different for each solution within the Monte Carlo set, this method removes the maximum likelihood translation (in x, y, and z) and rotation (x and y coordinates only) of each track (relative to the true transmission locations) prior to calculating relative errors. The optimal translation is removed first so that each track is rotated about the center of the track and not a point which changes for each track. The optimal rotation is removed because track rotation will change the relative sizes of the x and y coordinates between sources in the track.

To determine the significance of linearization error in the analytic expression for relative uncertainty, the Monte Carlo and analytic relative uncertainty estimates are

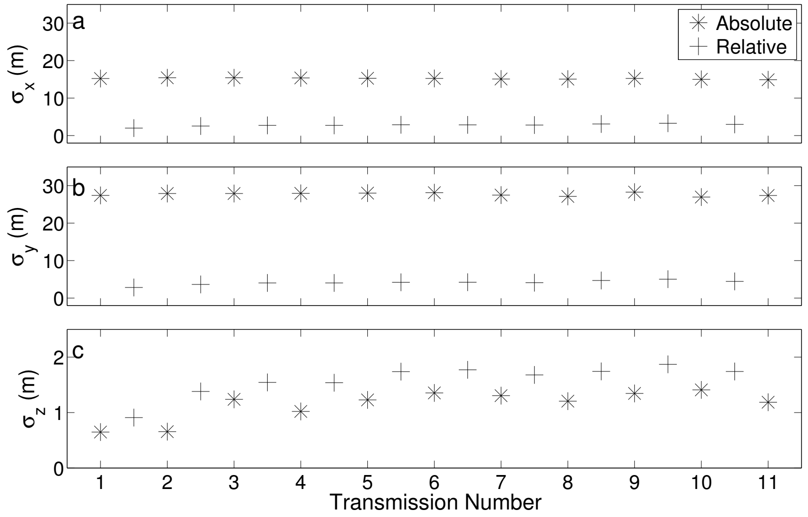

Figure 3.26: Comparison of relative and absolute (a) x, (b) y, and (c) z coordinate posterior standard deviations for curving-ray inversion. Each + symbol is the relative uncertainty between the two adjacent sources.

compared in Fig. 3.27. The small differences between empirical and analytic results suggest that the analytic approach to calculating relative uncertainties can yield a good approximation of the non-linear, empirical results and that linearization error does not cause significant errors in the estimated relative uncertainties.

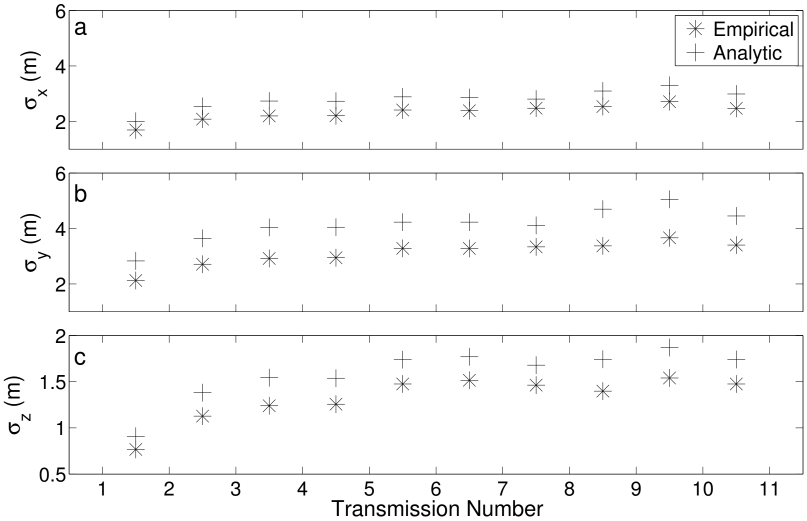

Figure 3.27: Comparison of Monte Carlo and analytic relative (a) x, (b) y and (c) z value uncertainties for curving-ray inversion.

Chapter 4

Field Work and Data Collection

This chapter describes the experiment which yielded the walrus vocalization data which are inverted for localization in Chapter 6. The author of this thesis assisted in designing the layout of the underwater acoustic recorders used for this experiment and acquired the sound speed profile used in this thesis while on assignment in the Chukchi Sea in August 2009.

4.1 Recorder Information

To perform 3D underwater localization in a range independent environment, at least three receivers must record each walrus knock. In light of this, three AMARs (Autonomous Multichannel Acoustical Recorder) were deployed in the northeastern Chukchi Sea (Fig. 4.1) from August–October 2009. A roughly equilateral triangular layout ($\sim$ 400 m between receivers) was selected to minimize the expected variation in localization uncertainty as a function of bearing about the array, and to provide a large ocean volume within the array while not having the recorders so far apart that knocks recorded on one AMAR were unlikely to be discernable on another. These three AMARs collected 24-bit data continuously with a 16 kHz sampling frequency over 2.5 months, producing approximately 300 GB of data per AMAR. Chapter 5 shows waveforms taken from this data.

Pictures of an AMAR before and during deployment are shown in Figs. 4.2 and 4.3. Each AMAR consists of an omni-directional hydrophone, acoustic recording electronics, a pressure housing rated for 400 m depth, a float collar which gives the AMAR a net-positive buoyancy, and two anchors. The equipment arrangement on the ocean bottom for the AMAR deployments from 2009 is illustrated in Fig. 4.4.

4.2 Deployment Plan

Localizing Pacific walruses using the localization algorithm developed in this thesis is important and appropriate for several reasons:

- Information on walrus location relative to anthropogenic noise sources (e.g., underwater oil exploration) would allow a more accurate assessment of the effects of these noise sources on the walrus population, including changes in walrus habitat usage over time.
- The enforcement of marine mammal exclusion zones around underwater anthropogenic noise sources would be enhanced by knowing the underwater positions of nearby animals, including walruses.
- Due in part to the important role sea ice plays in walrus migration and feeding habits, climate change is expected to have a particularly negative impact on the Pacific walrus population (Lowry et al. [2011]).
- Little work has been done in localizing underwater walruses; some work has been done in tracking tagged walruses in depth (Wiig et al. [1993]), tagged walruses latitude and longitude (Jay et al. [2009]), and in range and depth using passive acoustics (Mouy et al. [2011]) but these approaches did not include a rigorous uncertainty analysis.
- In air (Miller [1985]) as well as underwater (Schevill et al. [1966], Stirling et al. [1987], Schusterman and Reichmuth [2008]) walruses are very acoustically active.
- Given that Pacific walruses are found in a shallow and flat-bottomed environment, it was anticipated that localization using passive acoustics would work well.

Walruses are not expected to be evenly distributed throughout the Chukchi Sea. The Hanna Shoal (Fig. 4.5) is a shallow region of the Chukchi Sea located northwest of the community of Wainwright, Alaska, and was the deployment site for the three AMARs. Water depth varies from ~ 18 m to more than 30 m near the Hanna Shoal.

Figure 4.1: Satellite map of a portion of North America (courtesy of Google Inc.). The northeastern Chukchi sea is highlighted by the green circle.

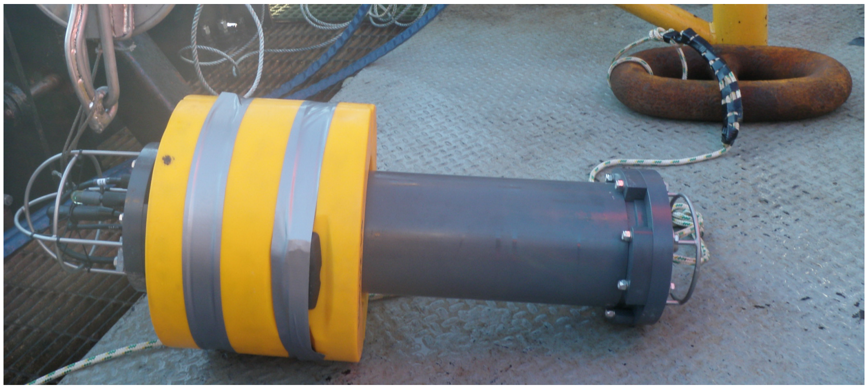

Figure 4.2: An AMAR on the deck of the ship prior to deployment (courtesy of JASCO Research, Ltd.).

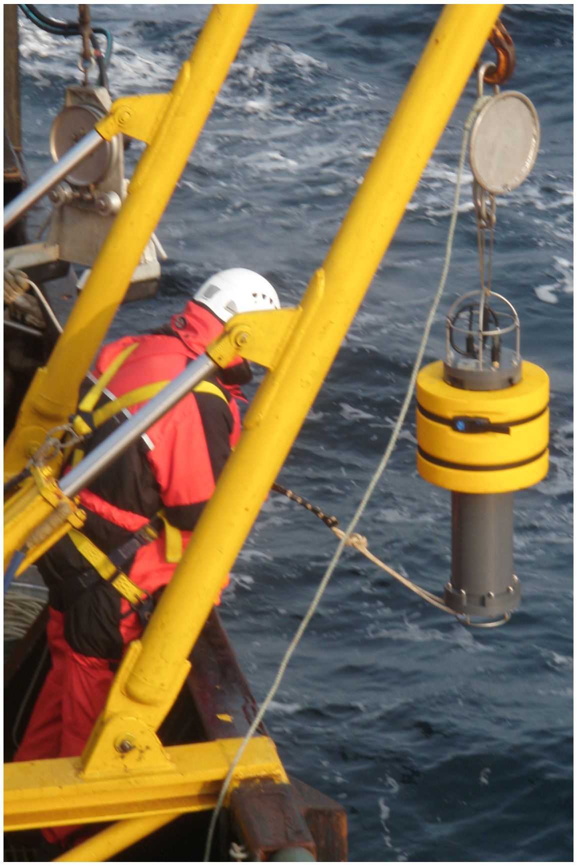

Figure 4.3: An AMAR after it is lifted off the deck by the crane and prior to release from the vessel (courtesy of JASCO Research, Ltd.).

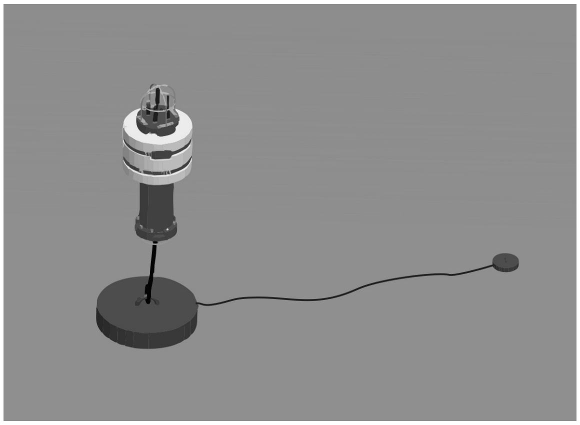

Figure 4.4: The underwater layout of an AMAR with two attached anchors (courtesy of JASCO Research, Ltd.).

For the area around the AMAR deployment site, water depth variation is expected to be very small. Based on historical walrus migration studies (Fay [1982]), a significant concentration of female and juvenile male walruses is thought to be present near the Hanna Shoal during the summer months. Historical walrus sightings in August for the Bering, Chukchi, and Beaufort Seas (collected over a 50 year period) are shown in Fig. 4.6. The figure shows a significant number of walrus sightings near the Hanna Shoal.

More recent evidence of walrus presence on the Hanna Shoal comes from a study by the United States Geological Survey (Jay et al. [2009]) in which satellite tracking tags were attached to walruses in the Chukchi Sea throughout the summer of 2009. Tagging locations (X symbols), recorded walrus tracks (yellow lines), and the final recorded walrus positions (red circles) for each of the tagged animals are shown in Fig. 4.7. The Hanna Shoal (highlighted by the green arrow) showed a high concentration of walruses.

Finally, benthic sampling carried out in 1986 showed a significant concentration of infaunal mollusks near the Hanna Shoal (Feder et al. [1994]), as shown in Fig. 4.8. Based on studies of the stomach contents of walruses killed by native hunters (Fay [1982]), walruses are known to consume these organisms.

4.3 Experiment Uncertainty Estimation

The measurements of hydrophone positions, water depth, and sound speed profile offset for this study have significant uncertainties. To ensure that the posterior uncertainty estimates for source (walrus) locations represent the state of knowledge of the experimental geometry and environment the uncertainty of these measurements must be quantified. The ABIC linearized Bayesian inversion algorithm used in this study considers these uncertain quantities to be Gaussian-distributed random variables. This section presents the reasoning behind the prior uncertainties chosen for these random variables.

Immediately after deployment, the latitude and longitude for each AMAR was measured using a handheld GPS receiver on the deployment vessel. The uncertainty in these measurements is estimated based on the following:

- The uncertainty in the GPS system used for this project is approximately 5 m.
- The handheld GPS was held approximately 5 m away from the receiver during

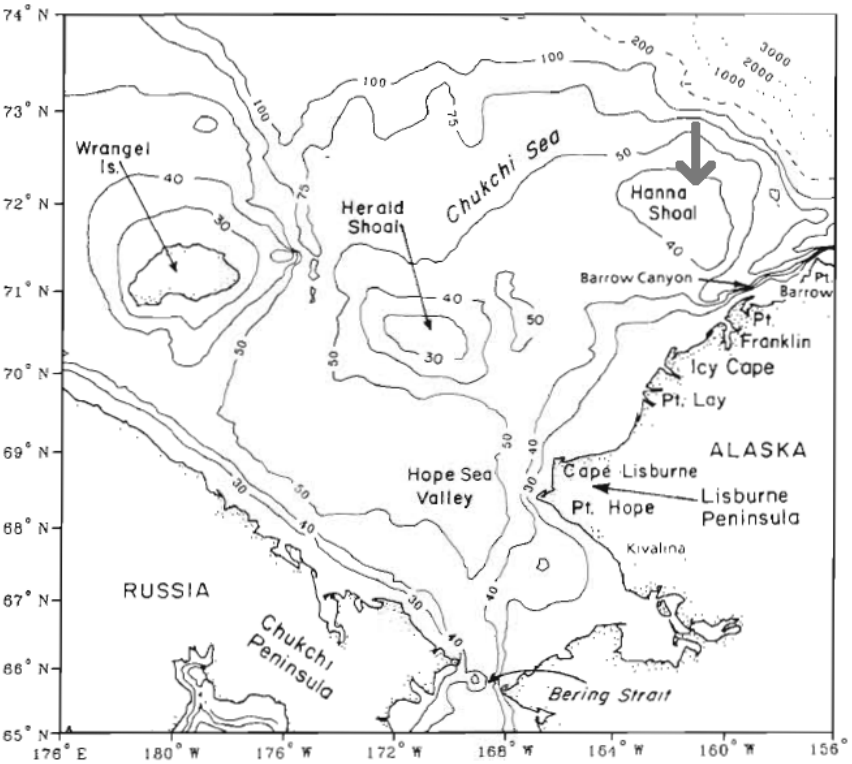

Figure 4.5: Bathymetric map of the Chukchi Sea (Feder et al. [1994]). The grey arrow highlights the Hanna Shoal.

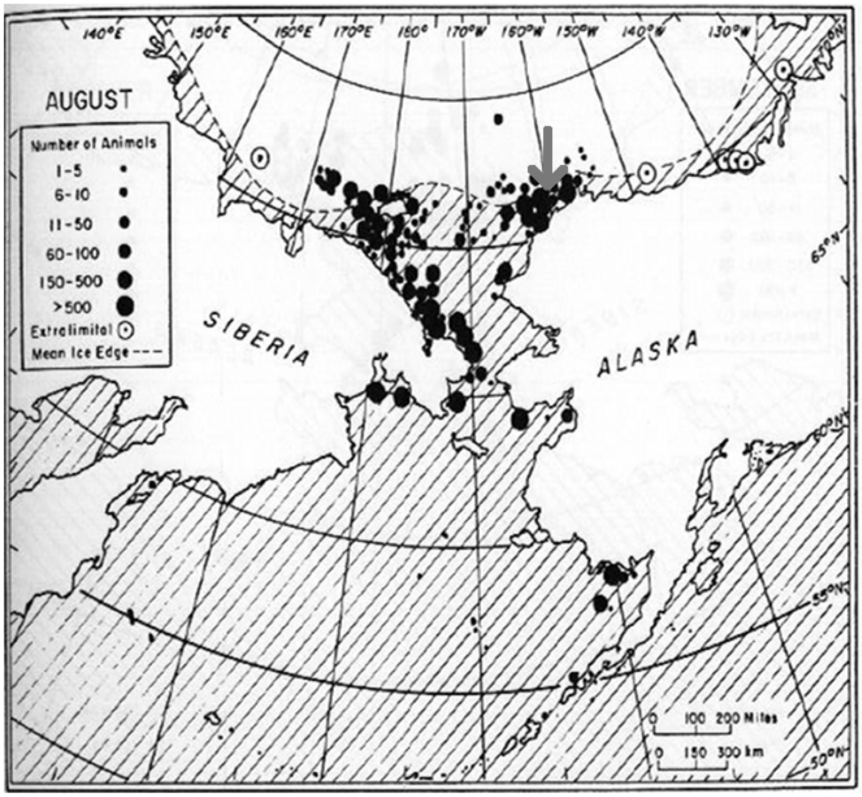

Figure 4.6: Historical walrus sightings for the month of August in the Chukchi, Bering, and Beaufort Seas from 1930 - 1979 (Fay [1982]). The grey arrow highlights the approximate location of the Hanna Shoal.

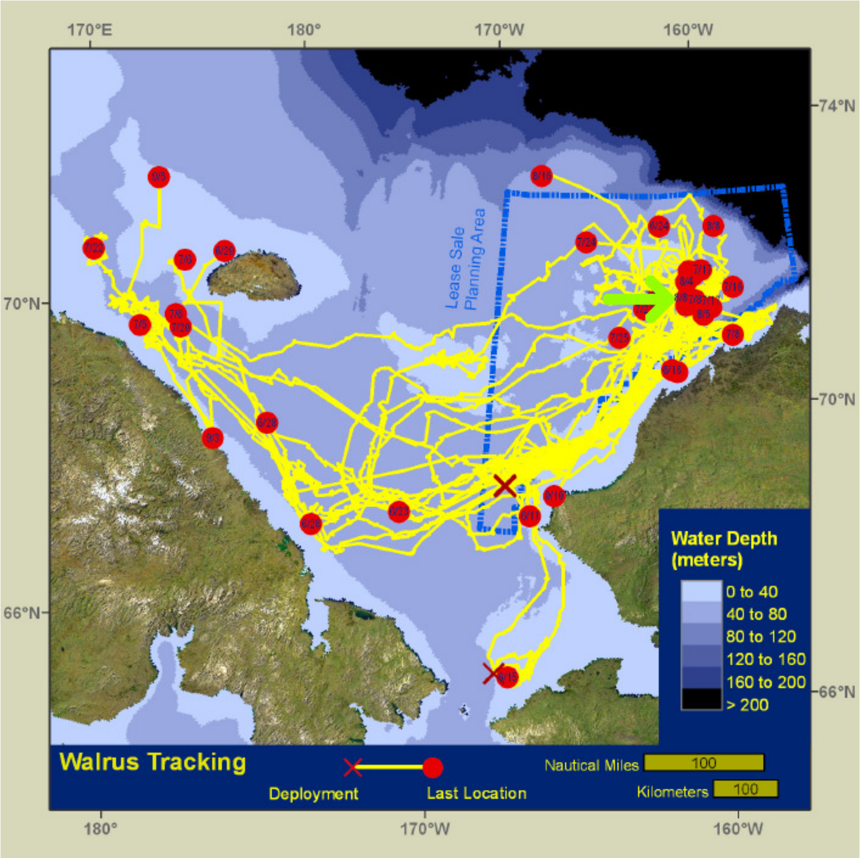

Figure 4.7: Summer migration of ∼ 30 walruses in the Chukchi Sea in the summer of 2009 as recorded by satellite tracking tags (Jay et al. [2009]). The green arrow highlights the Hanna Shoal.

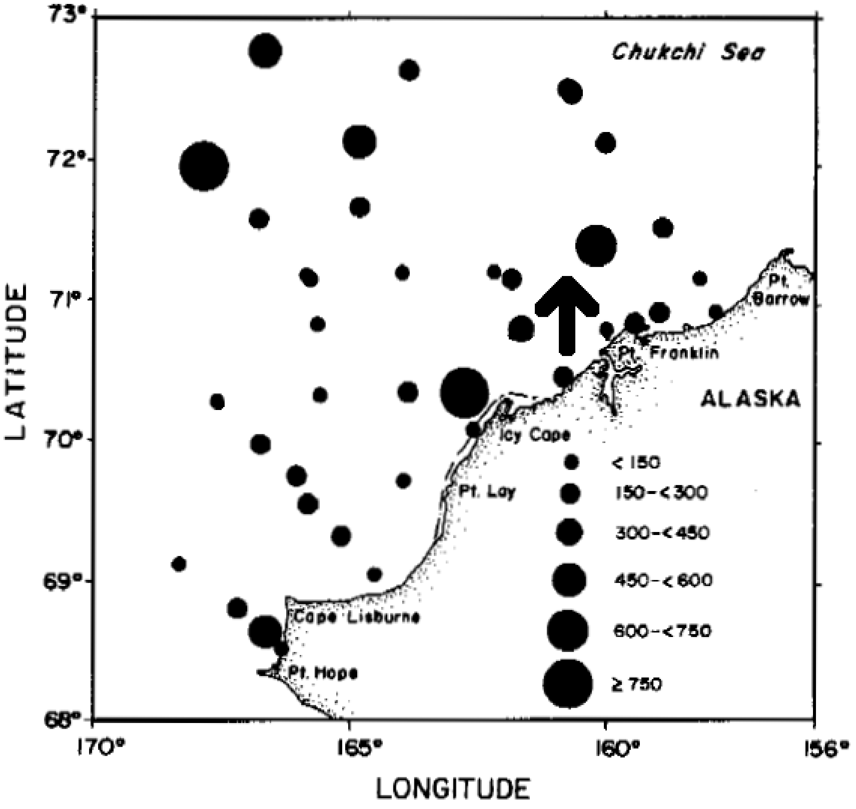

Figure 4.8: Abundance (individuals·m^{-2}) of infaunal mollusks in the northeastern Chukchi Sea. Abundances were estimated using grab samples collected from a surface vessel (Feder et al. [1994]). The arrow highlights the approximate location of the Hanna Shoal.

deployment. Since ship location relative to the deployment location is not fixed (i.e., the ship does not move in the same direction during each deployment) this introduces a further 5 m uncertainty.

- The deployment vessel can move approximately 5 m between the release of the AMAR from the ship and the GPS measurement, leading to an additional 5 m uncertainty.
- Current-induced drift causes the AMAR to move laterally as it decends to the ocean bottom. On the Hanna Shoal, this drift is estimated to be $\leq$ 5 m.
- Once the AMAR is on the bottom, time variable currents will cause the AMAR (which floats $\sim$ 2 m above the bottom) to sway, thereby making its horizontal location variable on the order of 1 m.

Under the assumption that all of these uncertainties are independent, the standard deviation of the measured X and Y hydrophone locations is taken to be the square root of the sum of squares of the individual uncertainties, which is $\sim$ 10 m. The standard deviation for the difference between AMAR depth and water depth is taken to be $\leq$ 1 m, and is due primarily to current-induced AMAR sway and uncertainty in the length of the rope connecting the anchor to the AMAR. Water depth uncertainty is taken to be $\leq$ 2 m due to uncertainty in the fathometer depth measurement and measurement locations. As a result, the uncertainty in hydrophone depth is taken to be 2 m.

There are at least two potential sources of error in the measured sound speed profile. First, calibration error can create a bias in the SSP of up to 2 m/s (Vincent and Hu [1997]). Also, the SSP (Fig. 4.9) used for this work was not measured at the time and location of the walrus knocks localized in Chapter 6. Specifically, this SSP was measured approximately 110 km away from the Hanna Shoal, and several days before the knocks used in this thesis. As a result, the true SSP may be significantly different than that shown in Fig. 4.9.

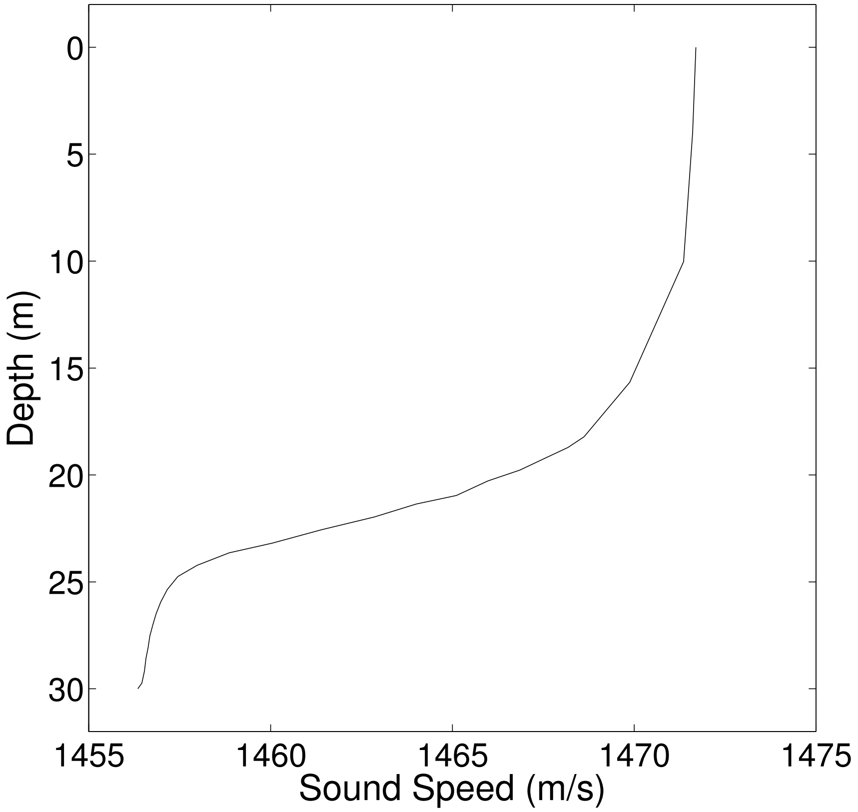

Figure 4.9: Sound speed profile used for all localizations using the curving-ray propagation model in this thesis.

Chapter 5

Data Processing

Walruses produce a large variety of vocalizations. To be useful for localization (as it is implemented in this work), the selected vocalization type must produce identifiable direct and interface-reflected path arrivals. Knocks were chosen for the following reasons:

- The short time duration of walrus knocks means that interface-reflected arrivals are less likely to be obscured by earlier arrivals than is the case for longer vocalizations. This simplifies interface-reflected arrival detection and labeling.
- The abrupt onset (i.e., short rise time) of walrus knocks makes arrival time uncertainties smaller than they would be for vocalizations with a more gradual onset.
- The relatively high amplitude of the recorded walrus knocks from the Hanna Shoal, compared to background noise levels, results in a significant area around the recorders within which walrus knocks are detectable.

Prior to performing localization on measured data, several data processing steps must be performed: walrus knocks must be distinguished from noise, arrival times identified and labeled, and arrival time uncertainties estimated. This chapter describes the data processing techniques found to be the most useful in performing these tasks for the Hanna Shoal data set.

5.1 Automated Knock Detection

The first processing step uses an automated marine mammal vocalization detector and classifier (developed by JASCO Research, Ltd.) to identify portions of the data set which contain a significant number of walrus vocalizations. Automated, rather than human-based, knock detection was used since it takes much less time and is expected to provide more consistent results over a large data set. The JASCO detector and classifier (JDAC) is able to correctly discriminate between a variety of different marine mammal vocalization types. As described in Mouy et al. [2011], the JDAC uses kurtosis (e.g., Balanda and MacGillivray [1988]) to detect walrus knocks. Effectively, kurtosis is sensitive to sudden extreme values in the data, making it well suited to detect walrus knocks; the recorded knocks have a short rise time and high amplitude compared to observed background noise levels at the Hanna Shoal. For a digital signal (s) consisting of N values, the kurtosis is

$$\beta_2 = \frac{\sum_{i=1}^{N}(s_i - \mu)^4}{(N-1)\sigma^4} \tag{5.1}$$

where μ and σ are the mean and standard deviation calculated over the N data. An illustration of the JDAC identifying twelve walrus knocks is presented in Fig. 5.1.

Each of the three recorders placed near the Hanna Shoal recorded acoustic data continuously for 2.5 months. The data from one of the recorders were processed using the JDAC by Xavier Mouy (a scientist working for JASCO Research, Ltd.). A kurtosis window size of 18 ms ($N = 288$) with 17% overlap was used. This analysis identified the number of knocks observed in each of the 3000 acoustic files recorded, and indicated a high concentration of walrus knocks just after midnight on August 12 but relatively low knock concentration at other times. Given the aim of intensively examining a small amount of data for this thesis project, it was decided to focus on identifying direct and interface-reflected arrival times for knocks near midnight on August 12 rather than spend time acquiring a large data set from files with relatively few walrus knocks.

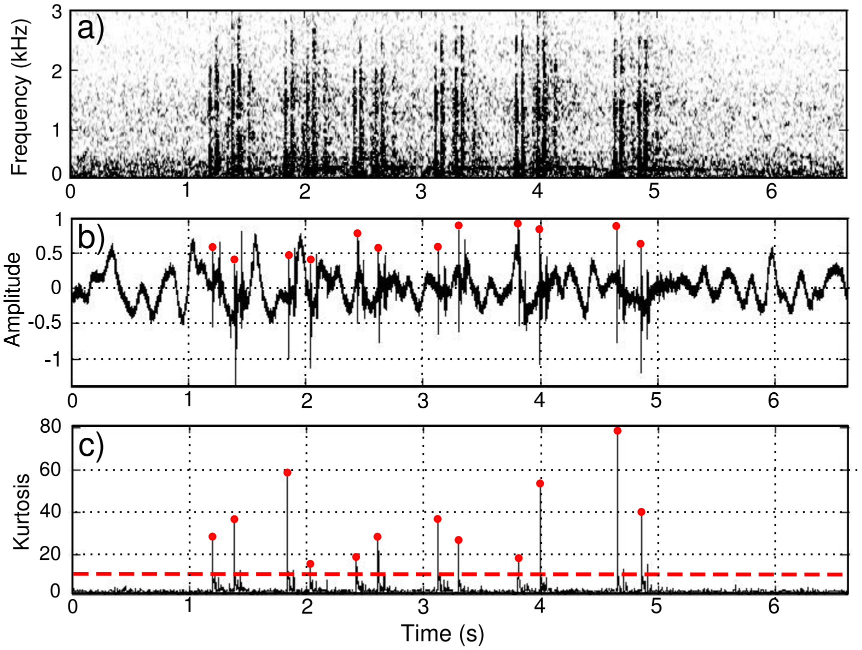

Figure 5.1: An example of the JASCO marine mammal vocalization detector and classifier identifying 12 walrus knocks (Mouy et al. [2011]). The (a) spectrogram for the knocks, (b) time-domain waveform, and (c) calculated kurtosis values with the kurtosis detection threshold indicated by the dashed red line are shown. Picked knocks are highlighted by red dots in (b) and (c).

5.2 Leading-Edge Arrival Time Identification and Labeling

The goal of arrival time identification and labeling is to produce the input data for the localization algorithm. Since this localization method is based on the time of arrival of direct and interface-reflected arrivals, any phase or amplitude changes due to reflections do not influence the localization, although they can make it more difficult to identify high-order interface-reflected arrivals. In general, it can not be assumed that the leading-edge arrival of a knock is the direct arrival since refraction can cause some arrivals to fail to reach the receiver. In this section, the first arrival is assumed to be the direct arrival. This assumption is borne out in the inversion results of Chapter 6. Some of the implications of erroneously labeling arrival paths are explored in Section 3.5.

Kurtosis was also used to assist in picking direct arrival times. Prior to beginning the picking process, the data was passed through a bandpass filter with cutoff

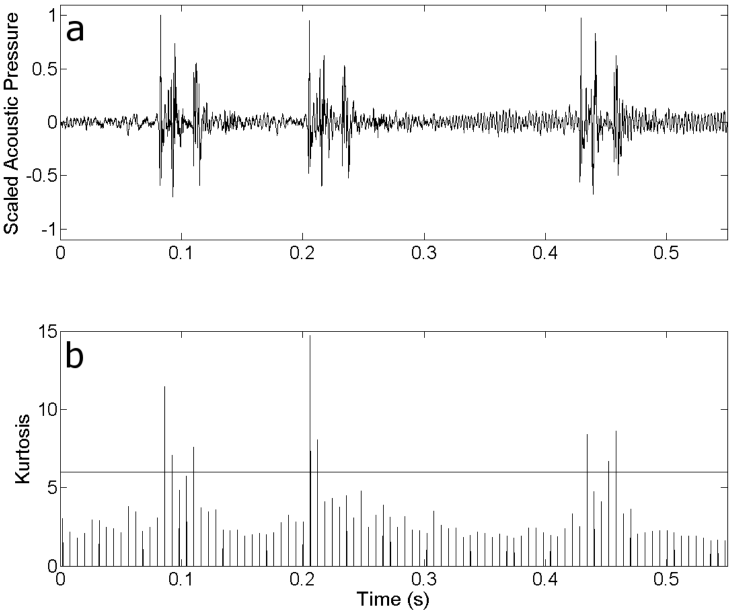

Figure 5.2: Three walrus knocks (a) with calculated kurtosis values (b). Window length is 0.01 s with 50% overlap. The horizontal line on the kurtosis plot is the threshold above which kurtosis values are deemed to indicate the leading edge of walrus knock.

frequencices of approximately 50 Hz and 4 kHz. Next, an appropriate kurtosis window size (the number of samples over which a single kurtosis value is calculated) is defined. If this window is too small, the calculated values of μ and σ will not be reliable. If too large, walrus knocks could fail to significantly change the calculated kurtosis value and may not be detected. Through trial and error experimentation, a window length of 0.01 s ($N = 160$) was found to reliably detect walrus knocks. Also through experimentation, a 50 % overlap between adjacent windows was chosen. The percent overlap directly impacts the time resolution (the minimum detectable time difference) of the algorithm; higher overlap makes arrival time estimates more precise but also increases the computational load.

A comparison of three time domain walrus knocks (a) with calculated kurtosis values (b) is shown in Fig. 5.2. The horizontal line on the kurtosis plot represents the threshold (selected through experimentation) to distinguish between knocks and background noise. Gaussian-distributed random noise has an expected kurtosis of 3, which explains the kurtosis values for the noise between the knocks.

To identify direct path arrivals, the kurtosis vector is scanned until a value is found that exceeds the threshold. The index of this high kurtosis value is saved and the corresponding waveform portion is displayed for the operator. The operator then decides if there is a direct arrival in the waveform. If there is, the operator refines the arrival time estimate given by the kurtosis index; due to the resolution of the kurtosis, the index of the high kurtosis value will likely not coincide with the direct arrival in the waveform. Once manual refinement is complete, the next high kurtosis value is considered, taking care to avoid false positives due to interface-reflected arrivals. In this way, the entire data set is processed for direct arrival times.

5.3 Interface-Reflected Arrival Time Identification and Labeling

To make use of as much of the available information in the data as possible, interface-reflected, in addition to direct, arrival times are sought. In general, it is expected that increasing the data set size will reduce the posterior uncertainties. Increasing the data set size also increases the number of unknowns which can be estimated. However, incorrectly labeling an arrival (e.g., labeling an arrival as BS when it is actually D) can cause large errors in the estimated track. This section describes a method for identifying and labeling interface-reflected arrivals while justifying the assigned labels.

The first task in labeling interface-reflected arrivals is to identify arrivals which are clearly distinct from ringing (due to earlier arrivals) and background noise. The waveform for a single walrus knock recorded by one of the Hanna Shoal AMARs is shown in Fig. 5.3. Clear arrivals were picked by hand and are highlighted. The primary feature used to pick these arrivals was the high amplitude leading edge of the arrivals relative to the noise.

To assign path type labels to these highlighted arrivals, it is assumed that:

- the propagation environment is range independent,
- knocks are made more than 2 m below the surface, and
- that the SSP is approximately known.

With these assumptions, the arrival paths can be ordered by increasing travel time (D, B, S, SB, BSB, . . .). The assumption on walrus depth comes from the fact that

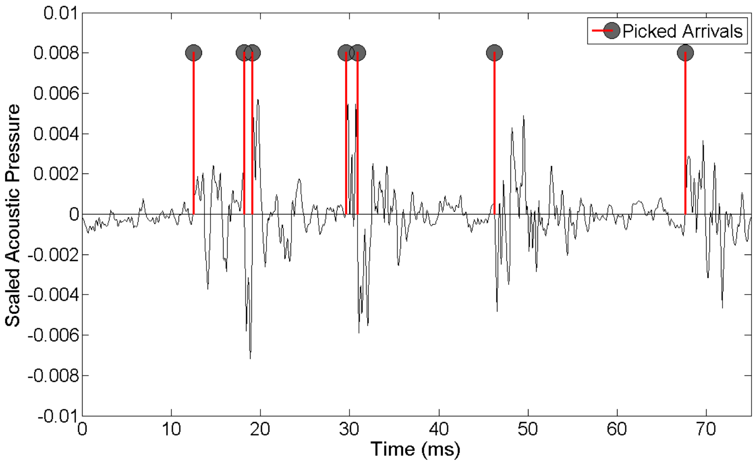

Figure 5.3: The recorded waveform for a walrus knock from the Hanna Shoal data set. Suspected direct and interface-reflected arrival times are highlighted.

if the walrus depth is less than the difference between the water and hydrophone depths (approximately 2 m), surface bounces will have smaller path lengths than bottom bounces. This is not likely to cause problems because if the walrus is close to the surface, the D arrival path length will be so similar to the path lengths for the B, S, and SB arrivals that it will probably be difficult to reliably pick the B, S, and SB arrival times.

Since the second highlighted arrival (SHA) in Fig. 5.3 arrives too late to be the B arrival, the SHA could potentially be the S arrival. However, the third highlighted arrival arrives too late to be the SB arrival. The next possibility is that the SHA is the BS arrival, making the third highlighted arrival the SBS arrival. To test this possibility, arrival path labels consistent with the SHA being the BS arrival are picked and the resulting data are processed using the ABIC linearized Bayesian inversion algorithm. The arrival times for the source location estimated via the ABIC algorithm are compared with the picked arrivals, along with the original waveform, in Fig. 5.4. The differences between picked and model-predicted arrival times are similar to the estimated data uncertainties (~ 0.5 ms).

For an arrival path labeling scheme to be reasonable, it must make sense given acoustic propagation in the environment. For example, consider a case where the leading edge arrival in Fig. 5.4 is labeled as BS rather than D. For this case, the estimated source location for the knock in this figure is close enough to the hydrophone that there should exist a D arrival which connects the source and receiver. Thus, in

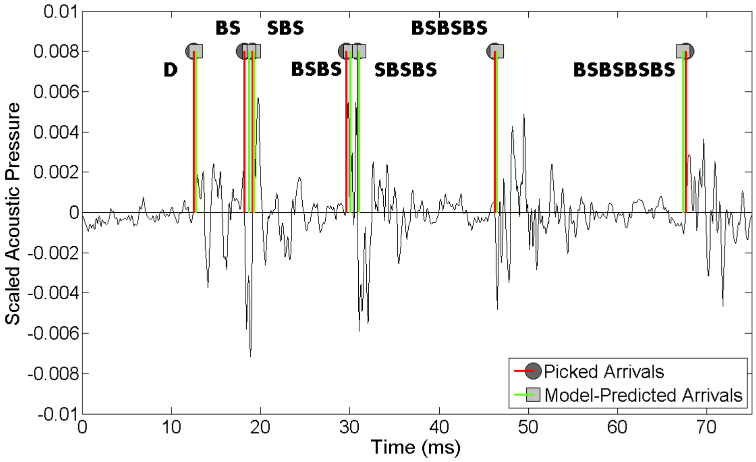

Figure 5.4: The recorded waveform for a walrus knock from the Hanna Shoal data set. Picked and model-predicted arrival times are highlighted and labeled. The picked arrival times are fit to approximately the data uncertainties (~ 0.5 ms).

this case, the leading edge arrival is likely not BS because the D arrival would have arrived before it. The fact that the labeling scheme depicted in Fig. 5.4 is both consistent with ray tracing given the SSP, and that the differences between picked and model-predicted arrival times are similar to the estimated data uncertainties, makes this labeling scheme plausible. The same approach to interface-reflected arrival labeling was used to label the arrivals for each hydrophone and knock in the track.

5.4 Arrival Time Uncertainty Estimation

Following the identification of direct and interface-reflected path arrival times, estimates of the arrival time uncertainty are made. An illustration of this process is presented in Fig. 5.5. The $*$ symbol highlights the estimated direct arrival time for this knock. Background noise and ringing within the knock make it impossible to precisely pick the arrival time. The $+$ symbols delineate the window (estimated by the operator) within which the arrival time is thought to lie, while α illustrates the maximum time duration from the estimated arrival time to the edge of the window for this specific arrival. Values for α for each arrival path type (D, BS, SBS, etc.) and hydrophone over a representative sample of the knocks within the track are estimated in the same way. Values for α were found to be consistent for a given arrival path type and hydrophone over all the calls in the track processed for this work.

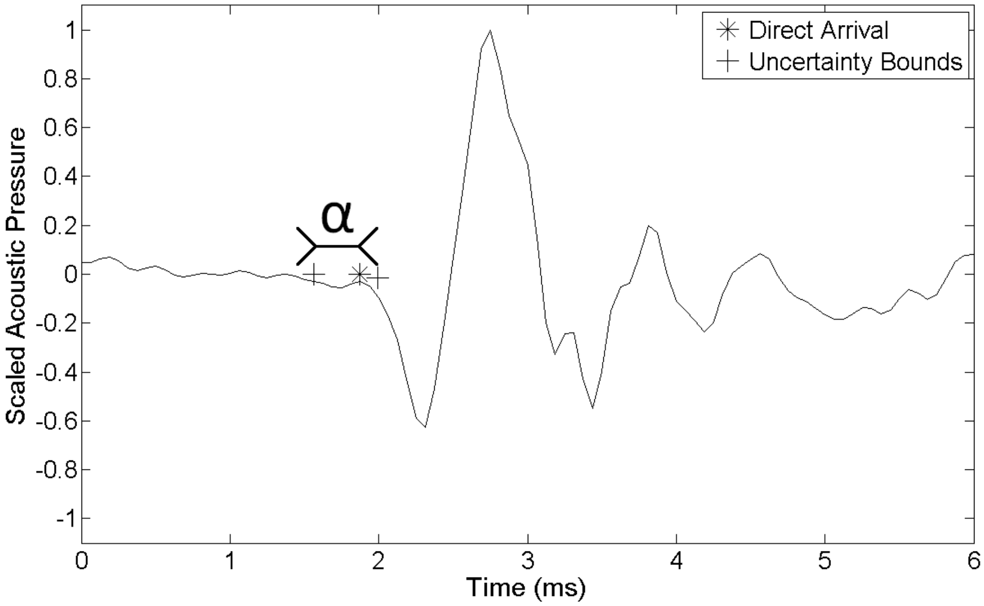

Figure 5.5: The waveform of the first portion of a walrus knock showing the picked direct arrival and uncertainty.

As discussed in Chapter 2, the inversion algorithm used for this work assumes that data errors are Gaussian-distributed. Consistent with this assumption, the average α (Fig. 5.5) over all direct path arrivals at a given hydrophone is used as the standard deviation of the Gaussian distribution which models the direct path arrival time uncertainty at this hydrophone (i.e., $\sigma_D = \bar{\alpha}_D$). This was done to ensure the data standard deviations represent conservative uncertainty estimates; $\sigma = \alpha$ is taken to be the expected standard deviation of the data errors whereas α is at least 2 times the expected standard deviation. Due to signal to noise ratio differences between arrival path types and hydrophones, arrival time uncertainties for each arrival path type and hydrophone were found to be different. Table 5.1 presents estimated arrival time uncertainties for each hydrophone and arrival path type used in this thesis.

For an inversion algorithm which treats data uncertainties as constants, to avoid overestimating the resolvable structure in the measured data it is better to slightly overestimate than underestimate data uncertainties. However, for an ABIC-based inversion algorithm, where the maximum likelihood uniform scaling factor (σ_0^2) for the data covariance matrix is estimated during the inversion, if data uncertainties are consistently overestimated the algorithm should compensate by returning a σ_0^2 value less than one. The relative sizes of data uncertainties, which are fixed for a single

Arrival Path Type	Hydrophone A	Hydrophone B	Hydrophone C
D	0.6	0.2	0.4
BS	0.8	0.4	0.4
SBS	0.5	0.6	-
BSBS	0.9	0.3	0.4
SBSBS	0.5	0.4	0.4
BSBSBS	0.9	-	0.4
BSBSBSBS	0.9	-	-

Table 5.1: Estimated arrival time uncertainties in milliseconds for the Hanna Shoal data set. The '-' symbols indicate that the arrival path was not picked in the measured data for the hydrophone in question.

ABIC inversion, determine which arrivals are fit more closely than others.

In picking the optimum σ_0^2 value, the ABIC algorithm does not distinguish between data errors and theory errors. In this work, theory errors exhibit themselves as differences between observed and modeled arrival times due to the propagation model not accurately representing the actual environment. For example, consider underwater acoustic localization where arrival times have very small uncertainty. If the model is a good representation of the actual propagation environment, it is expected that estimated sound source locations will be a good match with actual locations. However, if the propagation model neglects significant effects (e.g., errors in the SSP, horizontal refraction, or variable water depth), theory errors will result in sound source locations which significantly deviate from actual values. In this case, the ABIC algorithm may choose a value of σ_0^2 significantly higher than one and treat the prior estimates as relatively more important despite the fact that the failure of the algorithm to produce model-predicted data which matches the measured data is not due to measurement errors.

Chapter 6

Walrus Localization in the Chukchi Sea

As described in Chapter 5, the analysis of walrus knock occurence over the 2.5 month recording period on the Hanna Shoal indicated a particularly high number of knocks early in the morning of August 12, 2009. Rather than processing portions of the data set with few walrus knocks, the localization results presented in this chapter are based on a sequence of 11 knocks recorded shortly after midnight on August 12, 2009. The SSP depicted in Fig. 3.3 is used for inversions in this chapter. This profile was measured on August 9, 2009, approximately 110 km away from the Hanna Shoal recording site. This represents the only SSP measurement available and is believed to be representative of the SSP at the recording site, although some differences are possible.

6.1 Data Depiction

The recorded acoustic time series containing the walrus knocks used in this chapter are shown in Fig. 6.1. Each $*$ symbol highlights a knock used to localize the walrus which produced the knock. Not all knocks visible in this figure were used for localization; only those with clear arrivals in the data recorded by all three hydrophones were processed. This yielded a data set containing 11 knocks.

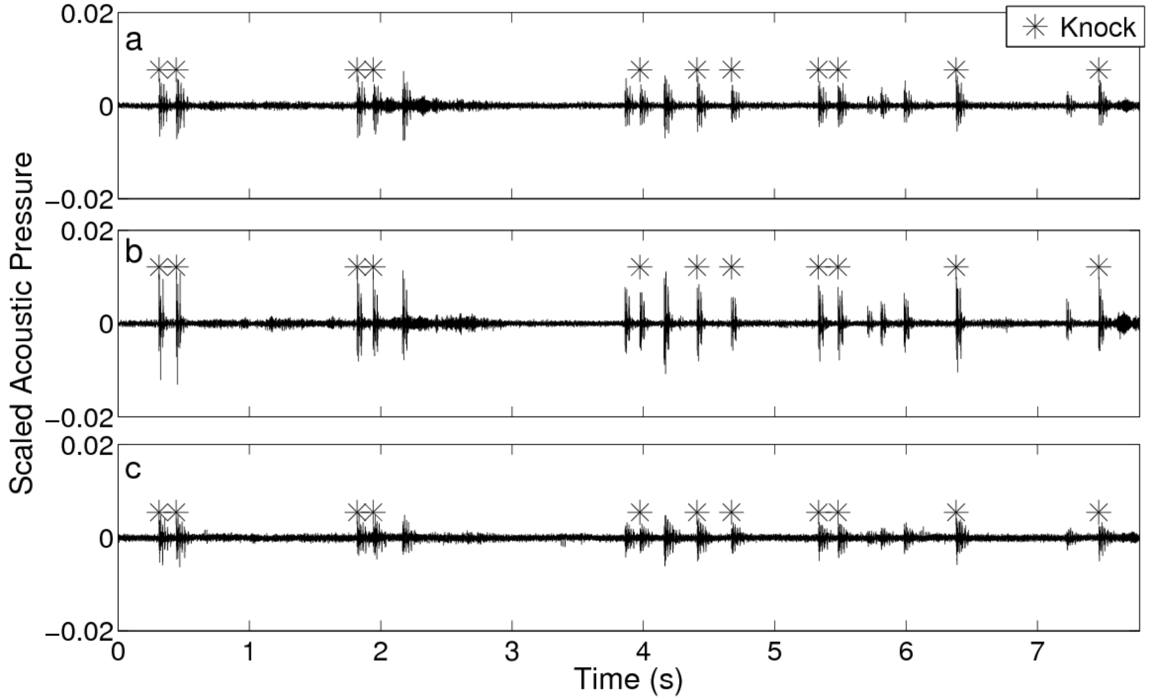

Figure 6.1: Acoustic time series for (a) hydrophone A, (b) hydrophone B, and (c) hydrophone C recorded just after midnight on August 12, 2009, on the Hanna Shoal. The $*$ symbols highlight the leading edges of walrus knocks used for localization in this chapter.

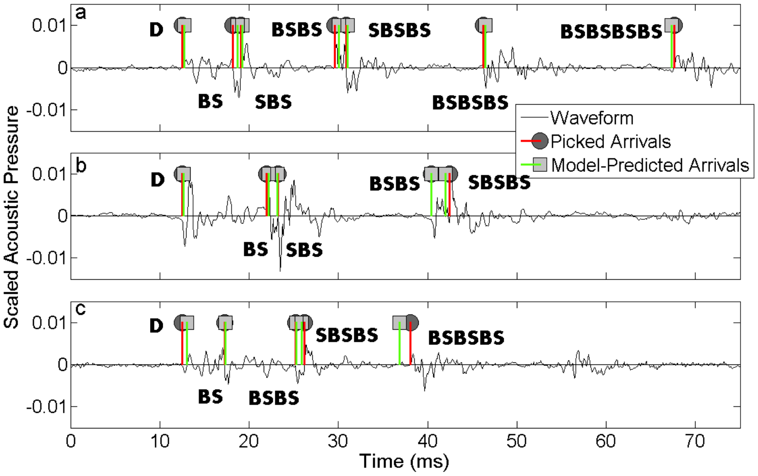

Figure 6.2: Picked and model-predicted arrival times along with the recorded acoustic time series for the second knock in the track recorded at (a) hydrophone A, (b) hydrophone B, and (c) hydrophone C.

6.2 Localization Results and Estimated Uncertainties

Following the identification of knock arrival times, and arrival time uncertainties, arrival paths were labeled. The labelled arrivals represent direct (D) and interface-reflected (e.g., BS, SBS, BSBS, SBSBS, and BSBSBS) paths for all knocks at the three hydrophones, with a few exceptions (SBS could not be identified at hydrophone C, BSBSBS could not be identified at hydrophone B, and BSBSBSBS was identified at hydrophone A). Other ways of labeling the arrival paths were explored but did not fit the data. Picked and model-predicted arrival times for the second knock in the track are presented in Fig. 6.2. The model-predicted arrival times are calculated via the curving-ray propagation model for the walrus position estimated from the localization inversion. The average RMS misfit between the picked and model-predicted arrival times (0.43 ms, averaged across all knocks and hydrophones) demonstrates that the picked data are fit to the estimated data uncertainties ($\sim$ 0.5 ms, see Table 5.1). Based on the path mislabeling study in Section 3.5, there is no obvious evidence of path label mismatch in the data residuals. The match between picked and model-predicted data is typical of the results throughout the track. The ray paths labeled in Fig. 6.2 are illustrated in Fig. 6.3 (hydrophone A), Fig. 6.4 (hydrophone B), and Fig. 6.5 (hydrophone C).

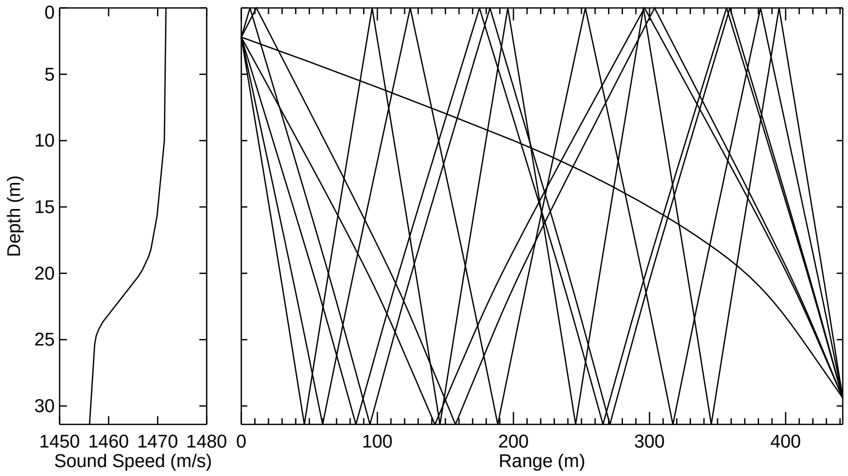

Figure 6.3: Ray paths for arrivals from the second knock at hydrophone A, along with the SSP.

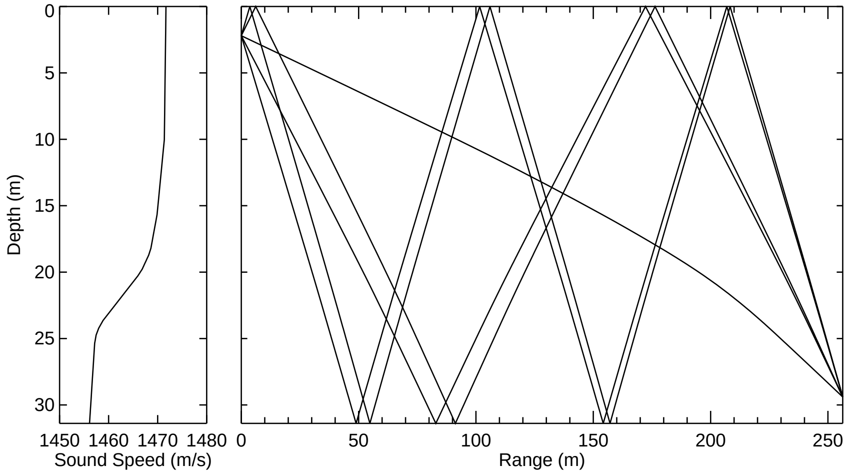

Figure 6.4: Ray paths for arrivals from the second knock at hydrophone B, along with the SSP.

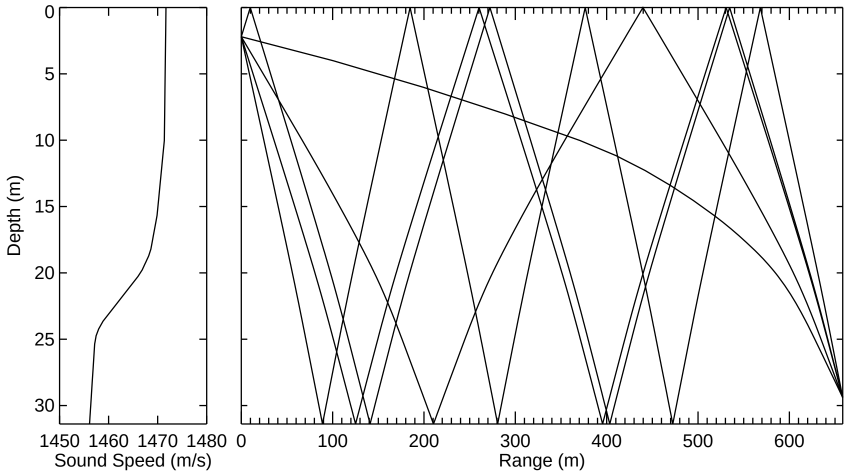

Figure 6.5: Ray paths for arrivals from the second knock at hydrophone C, along with the SSP.

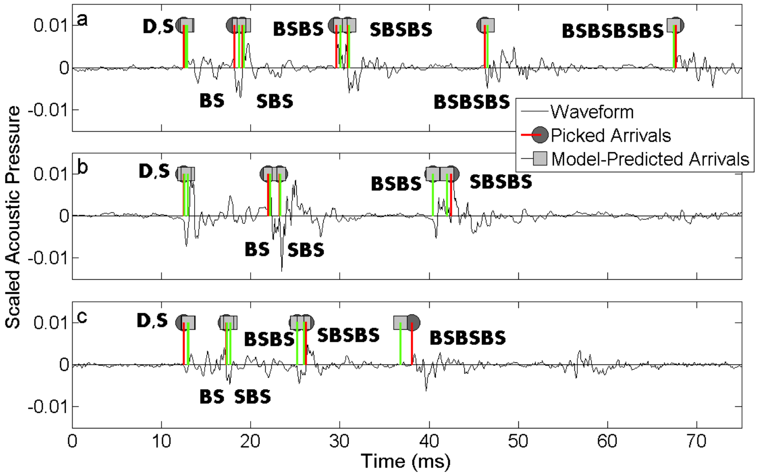

Figure 6.6: Picked and model-predicted arrival times along with the recorded acoustic time series for the second knock in the track recorded at (a) hydrophone A, (b) hydrophone B, and (c) hydrophone C. Certain additional model-predicted arrivals not picked during arrival path identification and labeling (S at hydrophones A-C and SBS at hydrophone C) are also shown.

During the arrival time identification and labeling process, not all potential arrival paths were picked. This was due to some arrivals being obscured by earlier ones (e.g., S at hydrophones A-C and SBS at hydrophone C). In addition to showing the same arrivals as Fig. 6.2, Fig. 6.6 also includes model-predicted arrival times for several arrivals not used for inversion. The proximity of the model-predicted arrival times for the unpicked S and SBS arrivals to picked arrivals supports the claim that the unpicked arrivals could not be identified due to interference with earlier arrivals.

A plan view of the estimated track and hydrophone locations is shown in Fig. 6.7. Given that the x and y axes are approximately parallel to the lines of latitude and longitude (respectively) at the Hanna Shoal, the track is located roughly southwest of the center of the hydrophone array. An enlarged view of the track, which also shows x and y relative uncertainties, in Fig. 6.8 shows an overall east-southeast direction of travel (as indicated by the arrow) for the walrus along the track. Straight lines connecting adjacent knocks are meant to illustrate the order in which the associated knocks were recorded and do not necessarily indicate the path of the animal. The thin lines which cross at each knock location are one standard deviation x and y relative uncertainties, the calculation of which is described later in this section. The zig-zag in the track between knocks 5 and 8 is within estimated relative uncertainties and, thus, is unlikely to be real.

Estimated knock x, y, and z values, along with estimated source times, are presented in Fig. 6.9. The error bars in this figure are absolute uncertainties and show that variation in x and y along the track is smaller than the absolute uncertainties for these quantities. Also, given the estimated z values and absolute uncertainties it is likely that the walrus is deeper at the end of the track than at the beginning. The fact that variation in x is more significant when compared with relative (Fig. 6.8) rather than absolute uncertainties (Fig. 6.9) illustrates the usefulness of examining relative uncertainties in this case. When only absolute uncertainties are considered, little can be said about the track other than general x and y locations of the knocks. However, when relative uncertainties are considered the x location of the walrus is shown to have varied significantly along the track. In other words, the absolute uncertainties show that the uncertainty in the estimated location of each knock relative to the array is greater than the x and y variation along the track, whereas the relative uncertainties show that it is very likely that the walrus was not stationary in the x-y plane throughout the track in question.

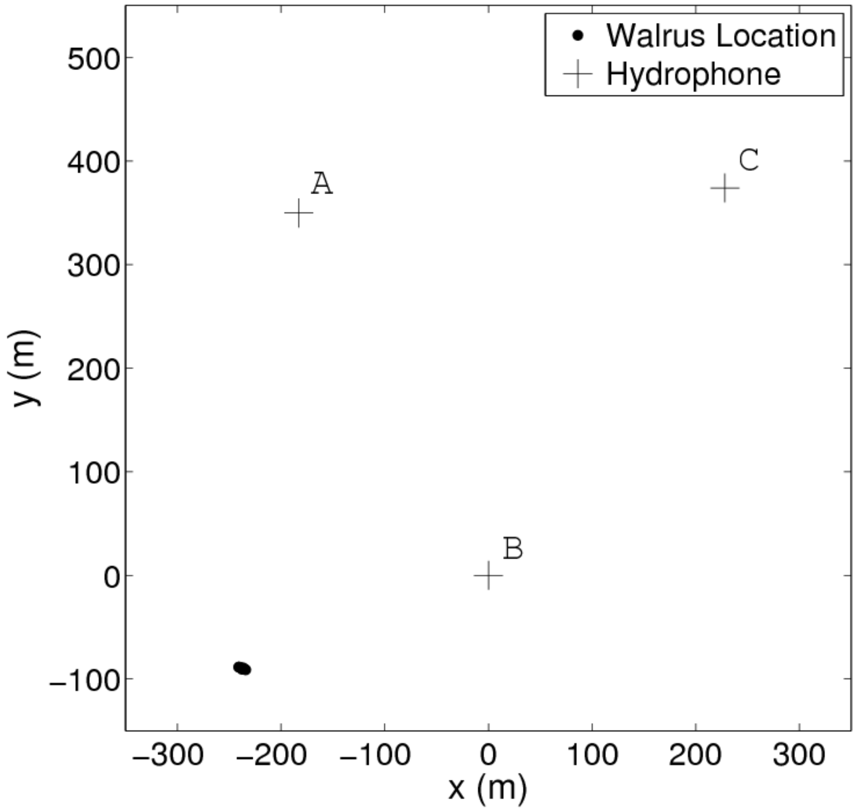

Figure 6.7: Estimated walrus locations relative to the estimated hydrophone positions. Hydrophones A, B, and C are labeled accordingly.

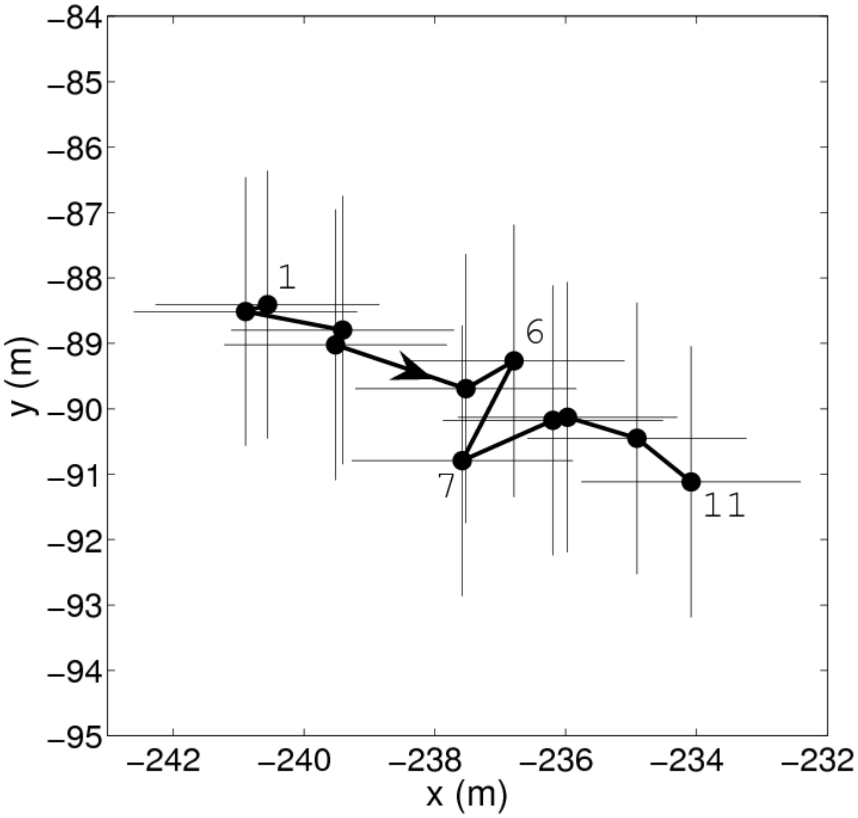

Figure 6.8: Estimated x and y walrus locations. The arrow indicates the direction of increasing estimated source time along the track. Fine lines intersecting each walrus location are one standard deviation relative uncertainty estimates. The first, sixth, seventh, and last (eleventh) knocks in the track are labeled.

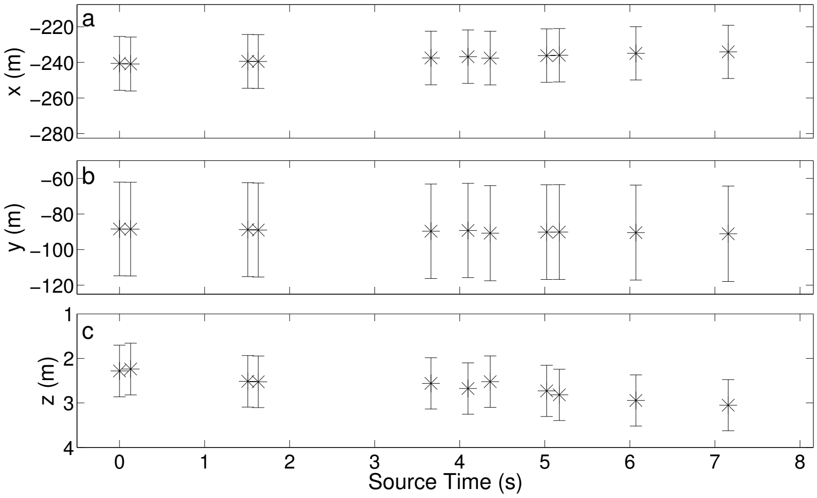

Figure 6.9: Estimated source (a) x, (b) y, and (c) z values relative to estimated source times. Error bars represent one standard deviation absolute posterior uncertainty estimates.

Parameter	**Estimated Value**	**Prior Estimate**
X [A,B,C] (m)	-182.86, 0.01, 228.24	-182.86, 0, 228.25
Y [A,B,C] (m)	349.79, 0.01, 373.93	349.78, 0, 373.94
Z [A,B,C] (m)	29.39, 29.39, 29.39	29.39, 29.39, 29.39
Time Synchronization [B,C] (s)	-379.29, -97.57	-379.26, -97.5
Source 2 Time (s)	0.884	0
Water Depth (m)	31.41	31.39
Sound Speed Offset (m/s)	-0.00017	0

Table 6.1: Estimated and prior values for selected nuisance parameters.

During the ABIC inversion process, values for σ_0^2 and μ are estimated. These values reflect the balance between data and prior information which minimizes the ABIC. The estimated value of $\sigma_0^2 = 1.17$ indicates estimated data uncertainties are similar to their initial assignment (i.e., the relative weighting data covariance matrix, $\mathbf{C_d}'$, as in Eq. (2.45)). The small value of $\sigma_0^2/\mu = 0.00013$ (used in Eq. (2.46)) estimated during the inversion indicates that, for at least some of the unknown parameters, the inversion is more strongly influenced by the prior estimates than by the data. In particular, Table 6.1 shows that hydrophone locations, time synchronization factors, water depth, and sound speed offset are similar to prior estimates. The similarity between the RMS data misfit and the data uncertainties, however, shows that the data are fit to an appropriate degree.

The prior estimates and uncertainty for the time synchronization parameters were estimated from the measured data. In this work, for example, the prior estimate of time synchronization between hydrophone B and A is the difference between D arrival times of a single knock at these two hydrophones. Due to the walrus not being located equidistant to the three hydrophones, there will be error in this measure of time synchronization. Assuming straight-line propagation, this error will be greatest if the walrus and the two hydrophones in question are collinear (i.e., the difference in travel times for the D arrival path is at a maximum). Given an approximate hydrophone spacing of 400 m, and using 1470 m/s as the approximate sound speed, the maximum difference in arrival times for the D arrival at two hydrophones is roughly 0.27 s. In other words, the time synchronization factors, estimated using the difference in D arrival times, could be in error by as much as 0.27 s. For inversions throughout this thesis, the prior uncertainty in the time synchronization factors is conservatively estimated to be 1 s.

Selected prior and absolute posterior uncertainties are presented in Table 6.2. To

Parameter	**Prior (σ)**	**Posterior (σ)**
Source 2 Location [x,y,z] (m)	10^5, 10^5, 10^5	15.16, 26.3, 0.58
Source 2 Time (s)	70	0.016
X [A,B,C] (m)	10, 10, 10	9.93, 9.67, 9.49
Y [A,B,C] (m)	10, 10, 10	9.73, 9.80, 9.62
Z [A,B,C] (m)	2, 2, 2	1.84, 1.76, 1.89
Time Offset [B,C] (s)	1, 1, 1	0.0082, 0.0069
Water Depth (m)	2	0.76
Sound Speed Offset (m/s)	2	2.00

Table 6.2: Prior and estimated absolute posterior uncertainty values.

calculate the posterior model covariance matrix ($\mathbf{C_m}$), Eq. (2.89) in Chapter 2 is used. During the inversion, μ is selected to minimize the ABIC. To calculate $\mathbf{C_m}$, the scaling on the prior model covariance matrix ($\mathbf{C_{\hat{m}}}$) is set to unity rather than using the ABIC-calculated hyperparameter values. This was done so that $\mathbf{C_m}$ is a function of the actual (physical) prior uncertainties estimated independently of the inversion, as was done for the regularized inversion in Dosso and Ebbeson [2006].

Absolute and relative call location uncertainties for the track are shown in Fig. 6.10. Absolute uncertainties are the square root of the main diagonal elements of $\mathbf{C_m}$. Relative uncertainties were calculated using Eq. (2.93) in Chapter 2. In this case, x and y relative uncertainties are lower than absolute uncertainties while z uncertainties are larger than absolute uncertainties. These trends are largely due to correlation between estimated knock locations. Due to hydrophone positions being uncertain (and there only being 3 hydrophones in the array), errors in hydrophone X or Y positions effect each of the knock x and y positions in the same way; all knock positions are shifted in a similar way in response to the hydrophone position errors. This does not hold for knock z positions because the sea surface and bottom provide an absolute frame of reference in depth. This means that knock z values are relatively uncorrelated compared to x and y (each of which have serial correlations). Thus relative z uncertainties are larger relative to absolute uncertainties than is the case for x and y. For instance, the (squared) relative uncertainty between the first (z_1) and second (z_2) walrus depths is given as

$$\sigma^2_{z_1 z_2} = C_{m,z_1} + C_{m,z_2} - 2C_{m,z_1,z_2}. \tag{6.1}$$

If walrus depths are uncorrelated (i.e., $C_{m,z_1,z_2} = 0$), and absolute uncertainties are similar for z_1 and z_2 (i.e., $C_{m,z_1} \approx C_{m,z_2}$), the relative z standard deviation is:

$$\sigma_{z_1 z_2} \approx \sqrt{2} C_{m,z_1} \approx \sqrt{2} C_{m,z_2}. \tag{6.2}$$

In Fig. 6.10, absolute z uncertainties are ~ 0.6 m while relative z uncertainties are ~ 0.8 m. The estimated z position relative uncertainty is very similar to that expected if z positions were uncorrelated ($\sqrt{2}(0.6) = 0.84$ m).

The y absolute uncertainties ($\sim$ 28 m) and relative uncertainties ($\sim$ 2 m) are larger than x absolute and relative uncertainties ($\sim$ 16 m and $\sim$ 1.7 m) due to the track position relative to the array.

On the whole, these uncertainties are likely small enough for the estimated walrus locations to be useful for observing walrus behaviour, including mean and maximum dive depths and time spent at the bottom. These uncertainties are also small enough to allow the estimated locations to guide the enforcement of marine mammal exclusion zones around underwater anthropogenic noise sources; since these zones are frequently hundreds of meters across, knowing walrus horizontal position to within approximately 10 m gives sufficient resolution to decide if a mammal has approached too closely to the sound source.

6.3 Swim Speed Analysis

In Fig. 6.11, estimated knock distance and time relative to the location and time of the first knock are shown. The slope of the least squares linear regression $\left(\sim 0.98 \text{ m/s}\right)$ for these data is interpreted as the estimated swim speed of the walrus, and is comparable to the normal walrus swim speed (2.8 m/s, Fay [1982]). This indicates that the track is plausible. Finally, the R^2 value of 0.992 for this regression and data set indicates that almost all the variability in the data is expressed by the regression.

To estimate swim speed uncertainty, a Monte Carlo-based approach is used. Random errors (zero mean, with standard deviations equal to knock position relative uncertainties and source time absolute uncertainties) were added to knock positions and source times to produce 10^4 noisy, independent knock position and time sets. For each of these sets, the slope of the least squares linear regression was calculated. The standard deviation for the set of calculated speeds is $\sigma = 0.19$ m/s.

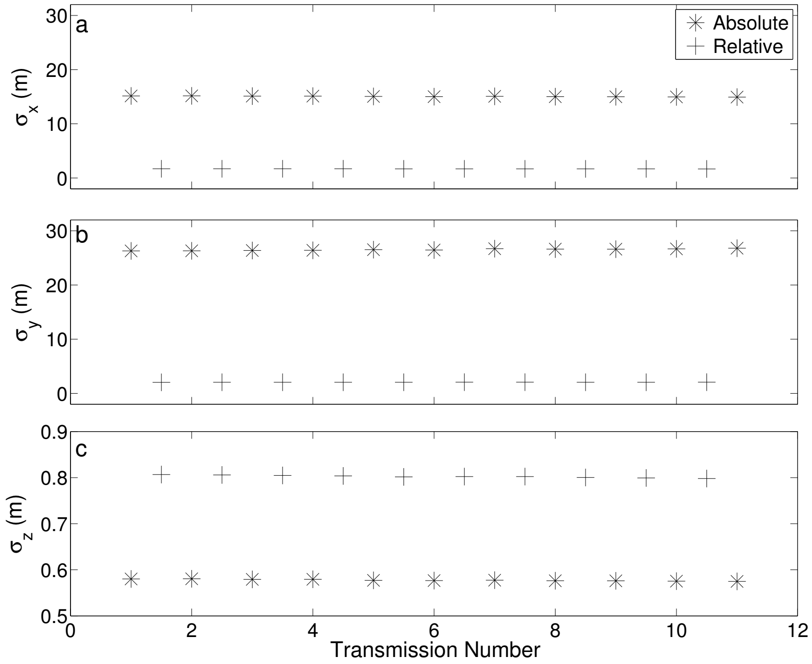

Figure 6.10: A comparison of absolute and relative call location uncertainties for (a) x, (b) y, and (c) z.

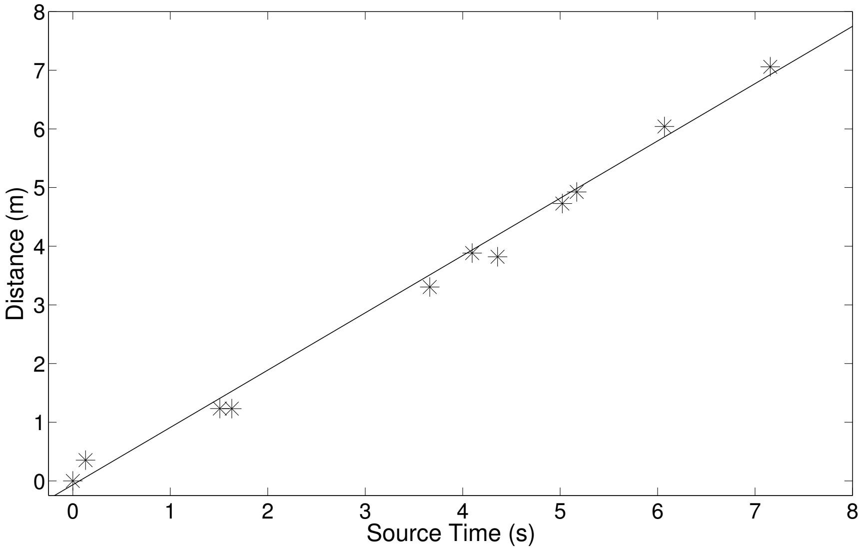

Figure 6.11: Estimated 3D distance and transmission time, relative to the first knock position and time. The line represents the least squares linear regression for this data, and has a slope of 0.98 (m/s) and R^2 value of 0.992.

Chapter 7

Summary and Discussion

The major focus of this thesis was the development and demonstration of an underwater marine mammal localization and tracking approach which provides rigorous location uncertainties. To properly account for uncertainty in the measurements of receiver parameters (e.g., 3D receiver locations and synchronization times) and environmental parameters (water depth and sound speed correction), these quantities are treated as unknowns constrained with prior estimates and prior uncertainties. Maximum *a posteriori* (MAP) estimates for sound source locations and times, receiver parameters, and environmental parameters are calculated simultaneously. Posterior uncertainties for all unknowns are calculated and incorporate both arrival time and prior uncertainties.

The work in this thesis builds upon a linearized inversion approach previously developed for array element localization (Dosso et al. [1998b], Dosso and Ebbeson [2006]). This approach is extended using the Akaike Bayesian information criterion (ABIC), as developed in Akaike [1974]. In array element localization, as presented in Dosso and Ebbeson [2006], an unknown scaling factor on the prior uncertainties is estimated as part of the inversion. However, data uncertainties are assumed to be known. In the work presented in this thesis, the ABIC is used to estimate unknown scaling factors on both the data and prior uncertainties.

Simulation results demonstrated that, at least for the case considered here, linearization errors are generally small and that the lack of an accurate sound speed profile does not necessarily cause large biases in the estimated positions. Also, increasing the size of the inverted data set (i.e., the number of direct and interface-reflected arrival paths identified in the measured data) was shown to decrease posterior location uncertainties and biases, although for many localization applications these effects may not be significant. While the arrival time data was shown to have information on estimated water depth, the prior and posterior uncertainties for estimated sound speed offset and hydrophone location coordinates are very similar.

The primary motivation for this work was to develop an algorithm for locating underwater Pacific walruses in the coastal waters around Alaska. Walruses are gregarious animals, and make a wide variety of vocalizations (including knocks, bells, and grunts). Walrus knocks were localized in this work due in part to their short time duration and fast rise time. Walruses are currently a species of interest to the scientific community for a number of reasons. First, according to the IUCN Red List of Threatened Species, climate change is expected to have a particularly negative impact on the Pacific walrus population (Lowry et al. [2011]). Second, increased anthropogenic noise (from ongoing oil exploration in traditional walrus habitats) may cause changes in Pacific walrus habitat usage over time. Third, little work has been done in observing walrus behavior in the wild.

In 2009, an array of approximately 40 underwater acoustic receivers was deployed in the northeastern Chukchi Sea (northwest of Alaska) from August to October to record the vocalizations of marine mammals including Pacific walruses and bowhead whales. Three of these receivers were placed in a triangular arrangement approximately 400 m apart near the Hanna Shoal (northwest of the community of Wainwright, Alaska). While the water depth on the Hanna Shoal varies from $\sim$ 18 m to more than 30 m, the region around the three receivers is expected to essentially be a range independent acoustic propagation environment. Historically, walruses have congregated near the Hanna Shoal in the summer months. A sequence of knocks from this data set was processed using the localization algorithm developed in this thesis, yielding a track whose estimated swim speed is consistent with current knowledge of normal walrus swim speed. An examination of absolute and relative walrus location uncertainties demonstrated the usefulness of considering relative uncertainties for applications where the precise location of the subject is not important (e.g., estimating swim speed).

The ability to estimate 3D walrus positions and positional uncertainties allows the collection of observations on walrus behavior in the wild which would otherwise be difficult or impossible to acquire. Potential areas for further research include the estimation of walrus knock source level and beam pattern, characterizing walrus swim speed in a variety of water depths, and the estimation of walrus dive depths and durations. Additionally, the uses of this localization approach are not constrained to the study of Pacific walruses, and could include the study of other marine mammals (e.g., beaked whales, sperm whales, or dolphins) and non-biological sound sources.

Bibliography

H. Akaike. A new look at the statistical model identification. *IEEE Transactions on Automatic Control*, 19(6):716–723, 1974.

R. Aubauer, M.O. Lammers, and W.W. Au. One-hydrophone method of estimating distance and depth of phonating dolphins in shallow water. *Journal of the Acoustical Society of America*, 107(5 Pt 1):2744–2749, 2000.

K.P. Balanda and H.L. MacGillivray. Kurtosis: A Critical Review. *The American Statistician*, 42(2):111–119, 1988.

L.M. Brekhovskikh and Y.P. Lysanov. *Fundamentals of Ocean Acoustics*. Springer-Verlag, New York, 3 edition, 2003.

W.C. Cummings and D.V. Holliday. Passive acoustic location of bowhead whales in a population census off Point Barrow, Alaska. *Journal of the Acoustical Society of America*, 78(4):1163–1169, 1985.

S.E. Dosso and G.R. Ebbeson. Array element localization accuracy and survey design. *Canadian Acoustics*, 34(4):3–13, 2006.

S.E. Dosso, G.H. Brooke, S.J. Kilistoff, B.J. Sotirin, V.K. McDonald, M.R. Fallat, and N.E. Collison. High-precision array element localization for vertical line arrays in the Arctic Ocean. *IEEE Journal of Oceanic Engineering*, 23(4):365–379, 1998a.

S.E. Dosso, M.R. Fallat, B.J. Sotirin, and J.L. Newton. Array element localization for horizontal arrays via Occams inversion. *Journal of the Acoustical Society of America*, 104(2):846, 1998b.

S.E. Dosso, N.E.B. Collison, G.J. Heard, and R.I. Verrall. Experimental validation of regularized array element localization. *Journal of the Acoustical Society of America*, 115(5):2129–2137, 2004.

F.H. Fay. *Ecology and biology of the Pacific walrus, Odobenus rosmarus divergens Illiger*. Number 74. United States Department of the Interior - Fish and Wildlife Service, Washington, DC, 1982.

H.M. Feder, N.R. Foster, S.C. Jewett, T.J. Weingartner, and R. Baxter. Mollusks in the Northeastern Chukchi Sea. *Arctic*, 47(2):145–163, 1994.

L.E. Freitag and P.L. Tyack. Passive acoustic localization of the Atlantic bottlenose dolphin using whistles and echolocation clicks. *Journal of the Acoustical Society of America*, 93(4 Pt 1):2197–2205, 1993.

R. Guo, S.E. Dosso, J. Liu, J. Dettmer, and X. Tong. Non-linearity in Bayesian 1-D magnetotelluric inversion. *Geophysical Journal International*, 185(2):663–675, 2011.

C.V. Jay, A.S. Fischbach, and D. Monson. Walrus tracking and telemetry data acquired from walruses instrumented on sea ice in the southern Chukchi Sea, June 2009. Technical Report June, USGS Alaska Science Center, Walrus Research Project, 2009.

M.H. Laurinolli, A.E. Hay, F. Desharnais, and C.T. Taggart. Localization of North Atlantic Right Whale Sounds in the Bay of Fundy Using a Sonobuoy Array. *Marine Mammal Science*, 19(4):708–723, 2003.

L.F. Lowry, K. Kovacs, and V. Burkanov. Odovenus rosmarus., 2011. URL `www.iucnredlist.org`.

E.H. Miller. Airborne acoustic communication in the walrus Odobenus rosmarus. *National Geographic Research*, 1(1):124–145, 1985.

Y. Mitsuhata and T. Uchida. 2-D inversion of frequency-domain EM data caused by a 3-D source. *Methods in Geochemistry and Geophysics*, 35:153–171, 2002.

Y. Mitsuhata, T. Uchida, Y. Murakami, and H. Amano. The Fourier transform of controlled-source time-domain electromagnetic data by smooth spectrum inversion. *Geophysical Journal International*, 144(1):123–135, 2001.

X. Mouy, D. Hannay, M. Zykov, and B. Martin. Tracking of Pacific Walruses in the Chukchi Sea using a single hydrophone. *Journal of the Acoustical Society of America*, Submitted, 2011.

E.M. Nosal and L.N. Frazer. Track of a sperm whale from delays between direct and surface-reflected clicks. *Applied Acoustics*, 67:1187–1201, 2006.

E.M. Nosal and L.N. Frazer. Sperm whale three-dimensional track, swim orientation, beam pattern, and click levels observed on bottom-mounted hydrophones. *Journal of the Acoustical Society of America*, 122(4):1969–1978, 2007.

M.B. Porter and Y.C. Liu. Finite-element ray tracing. *Theoretical and Computational Acoustics*, 2:947–956, 1994.

G. Ray, J. Mccormickray, P. Berg, and H. Epstein. Pacific walrus: Benthic bioturbator of Beringia. *Journal of Experimental Marine Biology and Ecology*, 330(1):403–419, 2006.

W.E. Schevill, W.A. Watkins, and C. Ray. Analysis of underwater Odobenus calls with remarks on the development and function of the pharyngeal pouches. *Zoologica*, 51:103–105, 1966.

R.J. Schusterman and C. Reichmuth. Novel sound production through contingency learning in the Pacific walrus (Odobenus rosmarus divergens). *Animal Cognition*, 11(2):319–327, 2008.

J.L. Spiesberger. Locating animals from their sounds and tomography of the atmosphere: experimental demonstration. *Journal of the Acoustical Society of America*, 106(2):837–846, 1999.

J.L. Spiesberger and K.M. Fristrup. Passive Localization of Calling Animals and Sensing of their Acoustic Environment Using Acoustic Tomography. *The American Naturalist*, 135(1):107–153, 1990.

K.M. Stafford, C.G. Fox, and D.S. Clark. Long-range acoustic detection and localization of blue whale calls in the northeast Pacific Ocean. *Journal of the Acoustical Society of America*, 104(6):3616–3625, 1998.

I. Stirling, W. Calvert, and C. Spencer. Evidence of stereotyped underwater vocalizations of male Atlantic walruses (Odobenus rosmarus rosmarus). *Canadian Journal of Zoology*, 65(9):2311–2321, 1987.

W.M. Telford, L.P. Geldart, R.E. Sheriff, and D.A. Keys. *Applied Geophysics*. Cambridge Univ. Press, New York, 1976.

A.M. Thode, G.L. D'Spain, and W.A. Kuperman. Matched-field processing, geoacoustic inversion, and source signature recovery of blue whale vocalizations. *Journal of the Acoustical Society of America*, 107(3):1286–1300, 2000.

C.O. Tiemann, A.M. Thode, J. Straley, V. OConnell, and K. Folkert. Three-dimensional localization of sperm whales using a single hydrophone. *Journal of the Acoustical Society of America*, 120(4):2355–2365, 2006.

H.T. Vincent and S.L.J. Hu. Geodetic position estimation for underwater acoustic sensors. *Journal of the Acoustical Society of America*, 102(5):3099–3100, 1997.

W.A. Watkins and W.E. Schevill. Sound source location by arrival-times on a non-rigid three-dimensional hydrophone array. *Deep-Sea Research*, 19:691–706, 1972.

W.A. Watkins and W.E. Schevill. Spatial distribution of Physeter catodon (sperm whales) underwater. *Deep-Sea Research*, 24:693–699, 1977.

O. Wiig, I. Gjertz, D. Griffiths, and C. Lydersen. Diving patterns of an Atlantic walrus Odobenus rosmarus rosmarus near Svalbard. *Polar Biology*, 13:71–72, 1993.